

# Optimal Control and Quantum Simulations in Superconducting Quantum Devices

Dissertation zur Erlangung des Grades  
des Doktors der Naturwissenschaften - Technischen Fakultät II  
- Physik und Mechatronik -  
der Universität des Saarlandes

von

Daniel J. Egger

Saarbrücken

2014

Tag des Kolloquiums: 31.10.2014

Dekan: Prof. Dr. Christian Wagner

Mitglieder des  
Prfungsausschusses: Prof. Dr. Frank K. Wilhelm-Mauch  
Prof. Dr. Giovanna Morigi  
Assoc. Prof. Dr. Michael Hartmann  
Dr. Reza Shaebani  
Prof. Dr.-Ing. Georg Frey

To my parents.



# Acknowledgements

First and foremost I would like to thank Professor Frank Wilhelm-Mauch who has given me the opportunity to work with him and his group. He has always been a source for motivation and intellectual stimulation. I would like to thank my parents, Melanie and Joe as well as my sister Sara for their love and support. I thank Emilia Green for her love, patience and support. Thanks also go to my comrades Luke, Per and Pierre-Luc for the stimulating scientific discussions and the good times spent in Saarbrücken and on various travels. I am also grateful to Emily Pritchett, Bruno Taketani and Markku Stenberg.

I thank the John Martinis group in Santa-Barbara for the collaboration in particular Daniel Sank, Julian Kelly, Rami Barends, Jim Wenner and John Martinis himself. Their ideas and experiments have largely shaped the context of this work. I would also like to thank Leo DiCarlo and his research team for the collaboration on frequency crowding issues in transmons.

Last but not least, I wish to thank all my friends in Saarbrücken and in Switzerland for the support and good times. Out of which particular thanks go to Dimitri, Mélissa, Céline, Laura, Laura and Chris, Chloé, John, Barbara and Amaël, El Presidente, Hannes, Michi and Stephan.



# Abstract

Quantum optimal control theory is the science of steering quantum systems. In this thesis we show how to overcome the obstacles in implementing optimal control for superconducting quantum bits, a promising candidate for the creation of a quantum computer. Building such a device will require the tools of optimal control. We develop pulse shapes to solve a frequency crowding problem and create controlled-Z gates. A methodology is developed for the optimisation towards a target non-unitary process. We show how to tune-up control pulses for a generic quantum system in an automated way using a combination of open- and closed-loop optimal control. This will help scaling of quantum technologies since algorithms can calibrate control pulses far more efficiently than humans. Additionally we show how circuit QED can be brought to the novel regime of multi-mode ultrastrong coupling using a left-handed transmission line coupled to a right-handed one. We then propose to use this system as an analogue quantum simulator for the Spin-Boson model to show how dissipation arises in quantum systems.



# Zusammenfassung

Quantenkontrolle ist die Wissenschaft von der Steuerung von Quantensystemen. In dieser Arbeit wird gezeigt wie die bisher bestehenden Hürden bei der Umsetzung von optimalen Steuerimpulsen für supraleitende Quantenbits überwinden können. Supraleitende Qubits sind aussichtsreiche Kandidaten für den Bau eines Quantencomputers. Wir entwickeln Steuerimpulse für Aufgabenstellungen mit dicht belegtem Frequenzspektrum am Beispiel des kontrolliertem Z-Gatters. Eine Methodik zur Optimierung der Zeitentwicklung des Quantensystems auf ein nicht-unitäres Ziel wird entwickelt und auf ein Modelle eines Detektors angewandt. Wir zeigen wie die Kalibrierung der Steuerimpulse durch eine Kombination von offenen und geschlossenen Methoden automatisiert werden kann. Das trägt zur Skalierung von Quantentechnologien bei, weil Algorithmen Steuereimpulse viel schneller und genauer als Menschen einstellen können. Zusätzlich, mit Hilfe einer linkshändigen Leitung gekoppelt an eine rechtshändige Leitung, zeigen wir wie Stromkreis-QED den neuen Bereich der vielmodigen, ultrastarken Kopplung erreicht. Wir schlagen vor, wie man dieses System als analogen Quantensimulator für das Spin-Boson Modell benutzen kann, um zu zeigen wie Dissipation in Quantensystemen zu einem Phasenübergang führt.



# Contents

<b>I</b>	<b>Introduction</b>	<b>1</b>
<b>1</b>	<b>Quantum Technologies</b>	<b>3</b>
1.1	Quantum Computing . . . . .	3
1.1.1	Qubits and Gates . . . . .	4
1.1.2	Physical Implementation . . . . .	7
1.1.3	Superconducting Qubits . . . . .	8
1.2	Simulation of Quantum Systems . . . . .	12
1.2.1	Digital Quantum Simulations . . . . .	13
1.2.2	Analogue Quantum Simulations . . . . .	14
<b>II</b>	<b>Optimal Control Theory</b>	<b>17</b>
<b>2</b>	<b>OCT Introduction</b>	<b>19</b>
2.1	Time Evolution of Quantum Systems . . . . .	20
2.2	Fidelity Measures . . . . .	21
2.2.1	Randomised Benchmarking . . . . .	22
2.3	Pulse Optimisation Algorithms . . . . .	26
2.3.1	BFGS . . . . .	28
2.4	Summary . . . . .	29
<b>3</b>	<b>Few Parameter Pulses</b>	<b>31</b>
3.1	Frequency Crowded Transmons . . . . .	32
3.2	Single Qubit Gates . . . . .	34
3.3	Applying DRAG . . . . .	35
3.4	Magnus Expansion . . . . .	36
3.4.1	Sideband Modulation . . . . .	39
3.4.2	Phase Correction . . . . .	41
3.4.3	Experimental Protocol . . . . .	42
3.5	Conclusions . . . . .	42

<b>4</b>	<b>Multiparameter Pulses</b>	<b>43</b>
4.1	Numerical Optimised Wah-Wah Pulses . . . . .	44
4.2	Qubit-Resonator-Qubit Architecture . . . . .	47
4.2.1	Analytic CZ Gate . . . . .	48
4.2.2	Limitations from Weak Anharmonicity . . . . .	49
4.3	Controlled-Z Gate Design by OCT . . . . .	50
4.3.1	Including Electronic Transfer Functions . . . . .	51
4.3.2	Frequency Dependent Anharmonicity . . . . .	52
4.3.3	Numerical Results . . . . .	53
4.3.4	Benchmarking . . . . .	56
4.4	CZ Error Sources and Mitigation Strategies . . . . .	58
4.4.1	Intrinsic Pulse Robustness . . . . .	59
4.4.2	Systematic Errors . . . . .	59
4.5	Conclusions . . . . .	64
<b>5</b>	<b>Non-Unitary Targets</b>	<b>67</b>
5.1	Optimal Control Algorithm . . . . .	67
5.2	Optimisation of a Phase Qubit Measurement Pulse . . . . .	70
5.2.1	Phase Qubit Model . . . . .	72
5.2.2	Optimisation Results . . . . .	74
5.3	Outlook and Conclusions . . . . .	78
<b>6</b>	<b>Ad-HOC</b>	<b>79</b>
6.1	OCT and Improperly Characterised Systems . . . . .	79
6.1.1	Problem Setting . . . . .	80
6.1.2	Modelling of the Control Transfer Chain . . . . .	82
6.1.3	Proposed Method . . . . .	82
6.2	Closed Loop Demonstration . . . . .	83
6.2.1	Random Gate Synthesis . . . . .	83
6.2.2	Closed-Loop Finding DRAG . . . . .	86
6.3	Realistic Setting Demonstration . . . . .	88
6.3.1	Gate-Taylor Quality Parameters Optimisation . . . . .	92
6.4	Robustness . . . . .	92
6.5	Conclusions . . . . .	95
<b>III</b>	<b>Quantum Simulations</b>	<b>97</b>
<b>7</b>	<b>Left-Handed Transmission Lines</b>	<b>99</b>
7.1	The System . . . . .	100
7.1.1	Equations of Motion . . . . .	100

7.1.2	Density of Modes of the CTL . . . . .	102
7.2	Applications . . . . .	111
7.2.1	Multi-Mode Entanglement . . . . .	111
7.2.2	Spin-Boson Simulator . . . . .	112
7.3	Conclusions . . . . .	116
	<b>Conclusion</b>	<b>117</b>
	<b>Publication List</b>	<b>120</b>
	<b>A Phase Qubit Potential</b>	<b>123</b>



# List of Figures

1.1	Bloch Sphere . . . . .	5
1.2	Quantum Circuit Example . . . . .	6
1.3	Charge Qubit . . . . .	9
1.4	Charge Qubit Energy Levels . . . . .	11
2.1	Randomised Benchmarking . . . . .	25
2.2	Interleaved Randomised Benchmarking . . . . .	26
2.3	Pixelised Control Field . . . . .	28
3.1	Frequency Crowded Transmons . . . . .	33
3.2	DRAG and Frequency Crowding . . . . .	36
3.3	Wah-Wah Pulse . . . . .	39
3.4	Wah-Wah and Frequency Crowding . . . . .	40
3.5	Wah-Wah Populations . . . . .	40
3.6	Wah-Wah Local Phase Shift . . . . .	41
4.1	Fast Numerical Wah-Wah Pulse . . . . .	45
4.2	Slow Numerical Wah-Wah Pulse . . . . .	45
4.3	Qubit-Bus-Qubit Architecture . . . . .	47
4.4	Sequential CZ Gate . . . . .	48
4.5	Two Excitation Level Crossings . . . . .	49
4.6	Strauch Gate with Weakly Non-Linear Qubits . . . . .	50
4.7	Strauch Gate: Acquired Phase . . . . .	51
4.8	Numerical CZ Gate: Pulse and Spectrum . . . . .	53
4.9	Comparison of the choice of Ginger and Fred . . . . .	54
4.10	Numerical CZ Gate: Populations . . . . .	55
4.11	Symmetrical CZ Pulse . . . . .	55
4.12	Numerical CZ Gate: Filter Function Effect . . . . .	56
4.13	Numerical CZ Gate Benchmarking: Quantum Speed Limit . . . . .	58
4.14	Numerical CZ Gate Benchmarking: Pulses . . . . .	58
4.15	Numerical CZ Gate Benchmarking: Populations . . . . .	59

4.16	Amplitude Errors . . . . .	60
4.17	AWG-Qubit Frequency Calibration Errors . . . . .	61
4.18	Effect of Calibration Errors . . . . .	62
4.19	Effect of Timing Errors . . . . .	63
4.20	Effect of Errors in the Hamiltonian Parameters . . . . .	64
5.1	Phase Qubit Potential . . . . .	72
5.2	Phase Qubit Model . . . . .	74
5.3	Optimal Measurement Pulses . . . . .	75
5.4	Populations during a Measurement Pulse . . . . .	76
5.5	Fast Measurement Pulses . . . . .	77
6.1	Layout of a Quantum Control Experiment . . . . .	81
6.2	Ad-HOC Protocol . . . . .	84
6.3	Convergence of Random Gate Synthesis . . . . .	85
6.4	Fidelity Function Evaluations . . . . .	85
6.5	DRAG with Model Free Methods: Pulses and Populations . . . . .	87
6.6	DRAG with Model Free Methods: Convergence Speed . . . . .	88
6.7	CZ Gate Tune-up . . . . .	89
6.8	CZ Gate Calibration Error Removal . . . . .	90
6.9	Gate Taylored Optimisation . . . . .	92
6.10	Closed-Loop Model Free Optimisation and Noise . . . . .	94
7.1	Coupled Transmission Lines . . . . .	100
7.2	Power Flow . . . . .	106
7.3	CTL Density of Modes . . . . .	108
7.4	Disordered Density of Modes . . . . .	110
7.5	Voltage Profile in a Disordered CTL . . . . .	110
7.6	Multi-Mode Entangled States . . . . .	112
7.7	Spin-Boson Model: Tunnelling Renormalisation . . . . .	114
7.8	Phase Diagram . . . . .	114

**Part I**  
**Introduction**



# Chapter 1

## Quantum Technologies

*Tes pensées s'évadent au coeur d'un royaume,  
comment est-il?*

Philippe Schneider

Most of the technologies that the modern human has adopted are either based on classical physics or make use of naturally occurring quantum phenomena. The laser is a perfect example, the quantum process by which the light is generated is well understood. However the quantum systems partaking in this process are not human made and one has to make due with the quantum properties of the atoms found in nature. Furthermore, the coherent laser light is a large collection of individual light quanta, i.e. photons in a coherent state. This is in contrast with the newly emerging *Quantum Technologies*. In these new technologies, information is processed quantumly instead of classically. The systems are engineered to have specific quantum properties and are manipulated on the level of individual quanta. Such technologies have a wide range of applications in computing, cryptography, simulations, measurements and potentially more.

This thesis explores two aspects of quantum technologies, the first focuses on the coherent control of quantum devices within the frame work of building a quantum computer. The second explores how a man engineered system can be put to use to simulate quantum phenomena otherwise intractable on a classical computer.

### 1.1 Quantum Computing

Up to date, all computers process information classically. Can anything else be imagined? Can a computer that processes information using the laws of

quantum mechanics — a *quantum computer* — be built? If so, what purpose would it serve and what makes building such a computer a difficult task? Currently this is under intense research. The physical system implementing the computer would have to be inherently quantum; many different systems could serve this purpose. Regardless of the underlying physical implementation, a quantum computer would be composed of quantum bits — *qubits* — as opposed to classical bits. Ideally these qubits are made of quantum systems with only two levels  $|0\rangle$  and  $|1\rangle$  representing the logical states of the bit. These qubits can be put into superposition states and be entangled. That is, two systems are said entangled if their state cannot be written as the product of states of each individual system [1]. A set of  $n$  classical bits exists in only one of the  $2^n$  states at any given time. On the other hand, due to the linearity of the Schrödinger equation, qubits can simultaneously be in a superposition of any of the  $2^n$  states. Therefore, the logical operations between qubits — *gates* — can be simultaneously applied on each state. However, upon measuring the final state of the qubits, the wave function will collapse onto one of the output states yielding one of the  $2^n$  qubit states with a specific probability. This shows that the massive parallelism resulting from superposition can in general not be used directly. This does not stop quantum algorithms, such as Grover’s search algorithm and the Shor algorithm, respectively used for searching through databases and factoring numbers, from outperforming any classical known equivalent. The prospect of being able to factor large numbers as well as simulate quantum systems has drawn much interest to the field of quantum computing. Indeed modern cryptography relies on the technical impossibility of factoring large numbers into two primes on classical computers. Quantum computers could overcome this.

### 1.1.1 Qubits and Gates

A quantum algorithm is a sequence of quantum gates — generally called a *quantum circuit* — acting on a set of qubits. The state of an individual qubit can be represented by

$$|\psi\rangle = \cos\left(\frac{\theta}{2}\right) |0\rangle + \sin\left(\frac{\theta}{2}\right) e^{i\varphi} |1\rangle,$$

with  $0 \leq \theta \leq \pi$  and  $0 \leq \varphi < 2\pi$ . Incidentally, the continuity of these two angles also shows that perfectly encoding a qubit state would require an infinite number of bits. Using the angles  $\theta$  and  $\varphi$ , the state  $|\psi\rangle$  can be represented on a sphere called the Bloch sphere, sketched in Fig. 1.1. Any quantum algorithm acting on  $n$  qubits can be implemented using only single

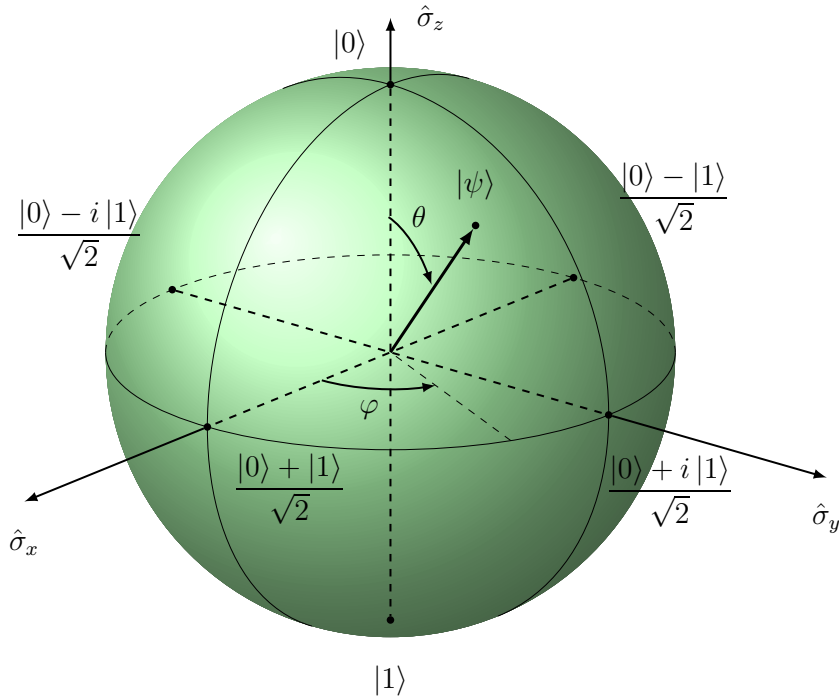


Figure 1.1: Bloch sphere. The state  $|\psi\rangle$  of a two level system can be represented in terms of two angle  $\theta$  and  $\varphi$ . The state of the sphere crossing a given axis are the eigenstates of the corresponding Pauli operator.

qubit operations and a two qubit operation. Such a set of gates is called universal. The single qubit gates, move the state  $|\psi\rangle$  from one point of the Bloch sphere to another. Of notable interest in quantum computing are the  $X$ ,  $Y$  and  $Z$  gates respectively given by the Pauli matrices

$$\hat{\sigma}_x = \begin{pmatrix} 0 & 1 \\ 1 & 0 \end{pmatrix}, \quad \hat{\sigma}_y = \begin{pmatrix} 0 & -i \\ i & 0 \end{pmatrix} \quad \text{and} \quad \hat{\sigma}_z = \begin{pmatrix} 1 & 0 \\ 0 & -1 \end{pmatrix}.$$

These gates serve as generators for a rotation of angle  $\alpha$ ,  $\hat{R}_k(\alpha) = e^{-i\alpha\hat{\sigma}_k/2}$  around axis  $k \in \{x, y, z\}$  of the Bloch sphere. One gate often recurring in quantum algorithms is the Hadamard defined by

$$H = \frac{1}{\sqrt{2}} \begin{pmatrix} 1 & 1 \\ 1 & -1 \end{pmatrix}.$$

Classical computing would be ineffective without the ability to condition an operation on a bit depending on the state of another one. This also applies to quantum computing. The quantum extension of the classical XOR gate

is the two qubit controlled not (*CNOT*) gate

$$CNOT = \begin{pmatrix} 1 & 0 & 0 & 0 \\ 0 & 1 & 0 & 0 \\ 0 & 0 & 0 & 1 \\ 0 & 0 & 1 & 0 \end{pmatrix}.$$

This gate conditionally flips the state of the second qubit depending on the state of the first, much like the classical XOR. However, the reversibility of the CNOT, imposed by quantum mechanics, distinguishes it from its classical counterpart. It is used to form a universal set of gates [2]. The CNOT is often used to entangle two qubits since it is capable of generating, from a separable state, the non-local Bell states defined by  $|\Phi^\pm\rangle = (|00\rangle \pm |11\rangle)/\sqrt{2}$  and  $|\Psi^\pm\rangle = (|01\rangle \pm |10\rangle)/\sqrt{2}$ . The *CNOT* is thus an entangling gate. As example, Fig. 1.2 shows the quantum circuit used to generate  $|\Phi^+\rangle$  from the separable  $|00\rangle$  state. In some systems the interaction between qubits is not capable of directly implementing a CNOT gate in which case a controlled phase gate can be made

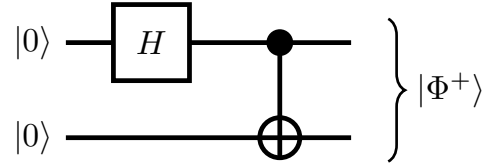


Figure 1.2: Quantum circuit capable of generating the Bell state  $|\Phi^+\rangle$  using a Hadamard gate and a CNOT. The horizontal lines indicate the qubits.

$$CZ = \begin{pmatrix} 1 & 0 & 0 & 0 \\ 0 & 1 & 0 & 0 \\ 0 & 0 & 1 & 0 \\ 0 & 0 & 0 & -1 \end{pmatrix}.$$

In this gate the  $|11\rangle$  state picks up a  $\pi$  phase. It should be noted that this gate is symmetric; no qubit distinctively plays the role of target or control. A CNOT gate can be recovered by applying a Hadamard gate before and after the CZ gate. Other perfect entangling gates are the  $\sqrt{\text{SWAP}}$  and  $i\text{SWAP}$  defined by

$$\sqrt{\text{SWAP}} = \begin{pmatrix} 1 & 0 & 0 & 0 \\ 0 & \frac{1}{\sqrt{2}} & -\frac{1}{\sqrt{2}} & 0 \\ 0 & \frac{1}{\sqrt{2}} & \frac{1}{\sqrt{2}} & 0 \\ 0 & 0 & 0 & 1 \end{pmatrix} \quad \text{and} \quad i\text{SWAP} = \begin{pmatrix} 1 & 0 & 0 & 0 \\ 0 & 0 & i & 0 \\ 0 & i & 0 & 0 \\ 0 & 0 & 0 & 1 \end{pmatrix}.$$

These are not the only perfect entangling gates. In fact, easily computable criteria exist to tell if an arbitrary gate is a perfect entangler or not [3, 4].

## Pauli and Clifford Groups

Together with the identity matrix, labelled  $\hat{\sigma}_0$ , the Pauli matrices can be used to construct the  $n$ -qubit Pauli group  $\mathcal{P}_n$ . This is done by taking the  $n$ -fold tensor product of all gates  $\hat{\sigma}_k$  multiplied by the factors  $\pm 1$  and  $\pm i$  where  $k \in \{0, x, y, z\}$  [1]. The Clifford group  $\mathcal{C}_n$  is then defined as the set of gates that leave the Pauli group invariant [5]

$$\mathcal{C}_n = \{C \in U(2^n) | CPC^\dagger \in \mathcal{P}_n \forall P \in \mathcal{P}_n\} .$$

This group includes the CNOT, Hadamard and phase gate (defined by  $|j\rangle \mapsto (-1)^j |j\rangle$   $j = 0, 1$ ). A Clifford gate circuit, i.e. a sequence of Clifford gates can efficiently be simulated by classical means [6]. Therein lies the interest of the Clifford group, this is used in randomised benchmarking, discussed in section 2.2.1.

### 1.1.2 Physical Implementation

A qubit is implemented by a two state system. In this two level space the logical states are labelled  $|0\rangle$  and  $|1\rangle$ . These do not necessarily correspond to ground and excited state and can be encoded by a linear combination of both. A generic form for a qubit Hamiltonian is given by

$$\hat{H} = \Omega_x(t)\hat{\sigma}_x + \Omega_y(t)\hat{\sigma}_y + \Omega_z(t)\hat{\sigma}_z .$$

Practically, some terms may miss and some may be time independent. Usually the two states are separated by an energy difference  $\hbar\omega_q$  (from now on  $\hbar = 1$ ) and in the basis  $\mathcal{B} = \{|0\rangle, |1\rangle\}$  the term  $\Omega_z$  is  $\omega_q/2$ . The time evolution of this part of the Hamiltonian alone will only produce phase gates, i.e. a rotation around the  $z$ -axis of the Bloch sphere. The contributions  $\Omega_x$  and  $\Omega_y$  allow to oscillate between the  $|0\rangle$  and  $|1\rangle$  states. If the functions  $\Omega_k$  are controllable, i.e. we can shape their temporal profile, then any of the single qubit rotations  $\hat{R}_k(\alpha)$  can be made.

Many different physical systems such as electrons and photons can be used to support a qubit. Some degrees of freedom such as spin make a natural choice. However qubits can also be built from two distinct levels in a larger Hilbert space. Here is a non-exhaustive description of various physical qubit implementations: Photonic qubits are made out of the two possible polarisations of a single mode [7]. Combining two photonic modes with different wave numbers allows us to build a dual rail qubit where the logical  $|0\rangle$  state corresponds to one quanta in the first mode and none in the second. The logical  $|1\rangle$  is the opposite [8]. An alternative to photonic qubits

are trapped ions. In such setups ions are trapped by electromagnetic fields and a qubit is formed in each ion using a transition between two energy levels [9]. This is a nice example where a qubit is formed out of two levels in a larger Hilbert space. The qubits are coupled through motional degrees of freedom resulting from Coulomb forces [10]. These qubits also hold the record<sup>1</sup> of the largest entangled quantum register [11]. Qubits can also be implemented by neutral atoms. These are trapped by inducing a dipole moment with an external electric field [12]. Qubits can then be formed using the internal atomic levels of the atoms [13, 14]. In these systems it is possible to isolate the quantum systems from the environment thus blessing the qubits with a long life-time. However atoms and photons are not the only quantum systems at our disposal. In solid state systems it is possible to single out an electron forming a quantum dot. The qubit is then built out of the spin states of the electron [15]. Another way to realise qubits is with impurities in solid state systems. As example, <sup>14</sup>N or <sup>13</sup>C impurities couple to Nitrogen-Vacancy centres in diamond. The NV centres are then used to address the nuclear spin of the impurities and use them as qubits [16]. Colour centres in diamond can also be used as single photon sources for use in quantum information processing. This can be done with NV centres as well as with Silicon-Vacancy centres [17, 18].

### 1.1.3 Superconducting Qubits

All of the qubits mentioned previously have a point in common. Their physical properties are set by nature and cannot be changed. For instance when dealing with trapped ions the choice lies in which ion of the periodic table to use. However the ions themselves cannot be engineered to have particular properties. *Superconducting qubits* are different in that their quantum properties are designed and engineered by humans [19–23]. Furthermore, their quantum degree of freedom is collective similar to a Bose Einstein Condensate [24]. These superconducting qubits consist of electrical circuits put into quantum states. They are fabricated by conventional electron beam lithography and sometimes even optical [25]. The resulting qubits are two dimensional leaving the third dimension available for accessing the qubits with the control and read-out electronics. This feature makes superconducting qubits very scalable in numbers. Scalability is the process of moving from proof of principal experiments, involving a few qubits, to a quantum computer coherently controlling millions of qubits.

It is well known that an inductor in parallel with a capacitor produces,

---

<sup>1</sup>at the time of writing

in terms of charge and current, the equations of motion of a harmonic oscillator [26]. The mathematical procedure to quantise this oscillator is well known. Practically to reach the ground state, the system must be made out of superconductors to avoid dissipation and has to be cooled to temperatures where thermal excitations become negligible. However such a qubit would be impractical due to the linearity of the harmonic oscillator which makes it uncontrollable. Therefore, non-linearity is introduced into the system by replacing the inductor with a Josephson Junction (JJ). Historically Martinis *et al.* [27, 28] first showed macroscopic quantum behaviour in a JJ in the 1980s. This led to the creation of different types of superconducting qubits, namely phase [25], flux [29] and charge [30, 31]. Theoretical developments on how to engineer quantum states with Josephson Junctions were carried out very early by Makhlin *et al.* [21, 32]. In all of these non-linear circuits it is easy to isolate two levels to make a qubit. In the flux qubit two circulating macroscopic currents of opposite sign form the quantum states. Whereas in the charge qubit it is the number of Cooper pairs on a superconducting island which is quantised. Later developments led to the Transmon qubit [33, 34] and the Xmon [35].

Here we briefly review a couple of superconducting qubits. We start with the charge qubit [30, 31, 36]. A superconducting island is made with JJ (with capacitance  $C$ ) and an external gate capacitor  $C_g$ . The system is controlled with the gate voltage  $V_g$ , see Fig. 1.3. The voltage and current across a JJ are related to the phase difference  $\varphi$  between the two superconducting wave functions on each side of the junction. They are respectively given by

$$V = \Phi_0 \dot{\varphi} \quad \text{and} \quad I = I_0 \sin \varphi.$$

The flux quantum for Cooper pairs is  $\Phi_0 = \hbar/2e$ . The Lagrangian for this system is

$$L = \frac{1}{2} (C + C_g) \Phi_0^2 \dot{\varphi}^2 - C_g V_g \Phi_0 \dot{\varphi} + E_J \cos \varphi$$

The Josephson coupling energy is  $E_J = I_0 \Phi_0$ . Applying the Euler-Lagrange equations to the phase yields the equations of motion one would obtain from Kirchoff's laws. The conjugate momentum to the phase is the number of Cooper pairs  $N = \dot{\varphi}/2E_c + N_g$ . Here we defined the gate charge as  $N_g = -\Phi_0 C_g V_g$  and the charging energy  $E_c = (2e)^2/2(C + C_g)$ . This leads to the

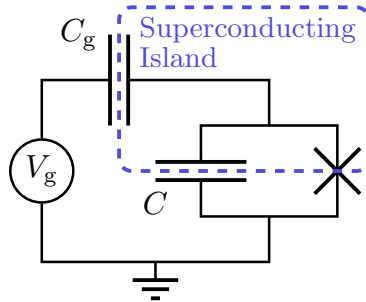


Figure 1.3: Charge Qubit

Hamiltonian

$$\hat{H} = E_c(\hat{N} - N_g)^2 - E_J \cos \hat{\varphi} \quad (1.1)$$

The charge qubit operates in the limit  $E_c \gg E_J$  [21, 37]. The charge term  $E_c(\hat{N} - N_g)^2$  is diagonalised by the states  $|N\rangle$  representing the number of Cooper pairs on the island. When  $N_g$  is half-integer two charge states are degenerate, these points are known as the charge degeneracy points and are indicated in Fig. 1.4 by the vertical dashed lines. The degeneracy is lifted by the Josephson term  $E_J \cos \hat{\varphi}$ . Analogously to quantum mechanics in one spatial dimension, we can write the wave-function as a plan wave  $\langle \varphi | N \rangle = e^{iN\varphi}$ . This shows that the action of the Josephson term on a charge state is  $E_J \cos \hat{\varphi} |N\rangle = \frac{E_J}{2}(|N+1\rangle + |N-1\rangle)$ . Thus the Hamiltonian takes the form

$$\hat{H} = \sum_N E_c(N - N_g)^2 |N\rangle\langle N| - \frac{E_J}{2}(|N\rangle\langle N+1| + |N+1\rangle\langle N|)$$

The charging energy  $E_c$  is thus the energy associated to having one extra Cooper pair, relative to the gate charge, on the island. The Josephson energy,  $E_J$  is the amount of energy required for a Cooper pair to tunnel across the junction. At the charge degeneracy point, the quantum state is a coherent superposition of two charge states. It is thus the number of Cooper pairs, i.e. the charge on the island, which is in a quantum state. This charge can be controlled by the gate voltage  $V_g(t)$ . The energy levels as function of gate charge, shown in Fig. 1.4, can be found using Mathieu functions [22, 33]; the spectrum is made from many avoided level crossings. When the charge qubit is biased far from these anti-crossings it stays in a charge eigenstate. Changing the bias  $N_g$  to an anti-crossing results in coherent oscillations between two charge states of the superconducting island. This implements single qubit rotations. However noise in  $N_g$  induces decoherence in the charge qubit since  $\partial E_k / \partial N_g \neq 0$  [31].

The charge qubit illustrates well how an electrical circuit can be put into a quantum state. The transmon qubit [33, 34], similar in design to the charge qubit, overcomes the limitation due to charge noise. It is operated in the limit  $E_J \gg E_c$  by shunting the JJ with a large capacitance. The dependence of the energy levels on gate charge  $N_g$  then becomes flat. This improves coherence times but comes at the cost of reducing the qubit's non-linearity. However weakly non-linear qubits can be controlled with adequate pulse shapes [38]. Additional controllability of the qubit is introduced by putting two JJs in parallel. This creates a superconducting ring interrupted by two JJs. Due to flux quantization [39], threading an external flux  $\Phi_{\text{ext}}$  through this loop

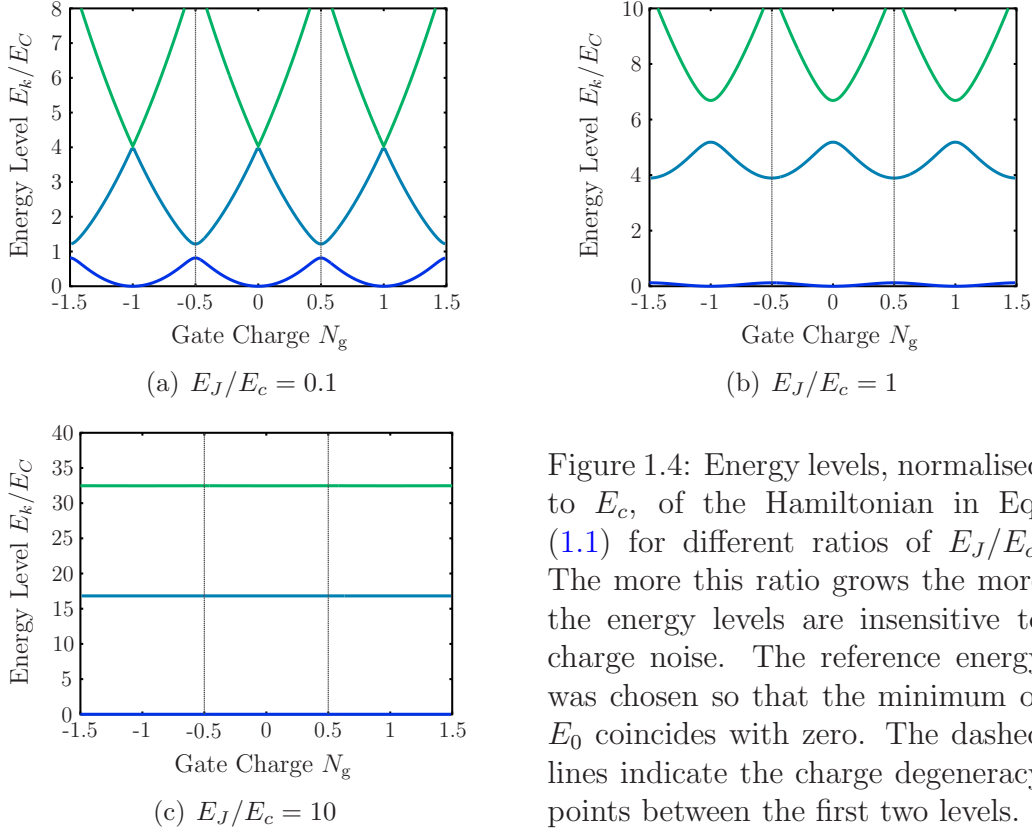


Figure 1.4: Energy levels, normalised to  $E_c$ , of the Hamiltonian in Eq. (1.1) for different ratios of  $E_J/E_c$ . The more this ratio grows the more the energy levels are insensitive to charge noise. The reference energy was chosen so that the minimum of  $E_0$  coincides with zero. The dashed lines indicate the charge degeneracy points between the first two levels.

makes the Josephson coupling energy tunable

$$E_J(\Phi_{\text{ext}}) = \frac{I_0 \hbar}{2e} \left| \cos \left( \frac{\pi \Phi_{\text{ext}}}{\Phi_0} \right) \right|. \quad (1.2)$$

In summary the charge qubit illustrates well how an engineered circuit can be put into a quantum state. The transmon shows how improvements on an existing design yields better qubits. This is well reflected in the coherence times of superconducting qubits which went from a few ns [40] to around 100  $\mu\text{s}$  in little over a decade [23, 31, 41–46]. The coherent control demonstrated by Nakamura *et al.* [31] of the charge qubit leads to the issue of making reliable gates for superconducting qubits. For a quantum computer to be viable, the quantum operations performed on the qubits need to have a very high fidelity, that is the measure of how close the realised gate is to the intended gate.

Different error detection or correction codes encode a single logical state into the physical states of many qubits [1, 47]. This redundancy introduces robustness against infidelities in the quantum operations. For example, the

error correcting Steane code requires gate fidelities above 99.999% [48]. In general most error correcting codes have threshold fidelities between  $1 - 10^{-6}$  and  $1 - 10^{-3}$  [47]. However, the surface code [49, 50], based on error detection requires a minimum gate fidelity of 99% [51]. This is much less than bit error rates in classical computers but nevertheless very hard to achieve. Below their respective threshold fidelity these codes degrade the fidelity of the quantum gates on the logical qubits but above it they allow more robustness against errors. In general, the higher the fidelity of single and two qubit operations are, the less overhead is needed to reduce errors on logical operations. Therefore attaining the threshold value in fidelity is not good enough, the implemented gates should have a higher fidelity.

In the first part of this thesis, Optimal Control Theory (OCT) methods [52–54] are applied to tackle the problem of making high fidelity gates in superconducting qubits. Since superconducting qubits are human engineered they can be designed to have more or less control. This reflects the trade-off between controllability and coherence. Often bringing more control lines to a qubit means creating additional noise sources. An example of this is shown in the transmon. Tuning the energy levels with external flux bias lines, Eq. (1.2), makes the qubit prone to flux noise. Some research groups have therefore opted for qubits with fixed energy levels [45, 55] whilst others work with tunable qubits [35]. In chapter 3 we show how spectral crowding issues due to fixed energy levels can be addressed with optimal control methods. Next, in chapter 4, is shown how optimal control can help improve a two qubit gate in a design with flux tunable energy levels. The gate can be made faster at the cost of a more complex pulse shape. Chapter 5 shows how to optimise pulse shapes when the target time evolution cannot be described by a unitary time evolution operator. The last chapter on optimal control, chapter 6, shows how to deal with the main shortcoming of Optimal Control Theory, that is the reliance of the theory on a model to design the control pulses. It is shown how a closed loop optimisation performed on the experiment can calibrate a pulse designed with OCT. The results in these last two chapters generalise outside of the field of superconducting qubits.

## 1.2 Simulation of Quantum Systems

Classical physics lends itself well to computer simulations. Indeed, if a classical system is in a given state at a given time, then the next state, an infinitesimal increment of time later, is given by a differential equation provided by the laws of nature. Upon discretisation of time and space, this process can be well described by a Turing machine and thus simulated on

a regular computer. Quantum physics, a more fundamental description of the world we live in, is probabilistic. The laws of quantum mechanics yield the probability amplitudes with which a system evolves from a given state to the next. Thus for a given configuration of the system we need to store the probabilities to every possible configuration a small time step later. This leads to exponential growth of the computation power as the system size is increased. Simulating quantum systems rapidly becomes intractable on a classical computer [56]. A way out was suggested by R. Feynman

*“Let the computer itself be built of quantum mechanical elements which obey quantum mechanical laws.”*

R. P. Feynman, Int. J. Theor. Phys. **21**, 467-488 (1982)

This led to the development of quantum computing introduced in the previous section, but also to *quantum simulations* [57]. The problem is simple: we wish to know some properties, e.g. a state or an observable, of a quantum system evolving under the action of a Hamiltonian  $\hat{H}_{\text{sys}}$ . Due to the exponential growth of system size, using a classical computer is impossible. The solution is to simulate the dynamics of  $\hat{H}_{\text{sys}}$  using another, usually more controllable, quantum system. There is a huge wealth of physics that can be simulated on different systems ranging from condensed matter physics to cosmology. A detailed yet non exhaustive list can be found in [57]. Quantum simulations are classified in two types *digital* and *analogue*. They are described below.

### 1.2.1 Digital Quantum Simulations

The insight of digital quantum simulations is to use the formalism of quantum circuits originating from quantum computing. Let the Hamiltonian  $\hat{H}_{\text{sys}}$  of the system we wish to simulate be written as

$$\hat{H}_{\text{sys}} = \sum_{k=1}^M \hat{H}_k.$$

In general computing the resulting time evolution  $\hat{U}_{\text{sys}}$  is a complicated task since the different  $\hat{H}_k$ 's might not commute. However, for a small time step  $\Delta t$  there exists various approximations for computing  $\hat{U}_{\text{sys}}(\Delta t)$  [1]. An example is the Trotter formula

$$\hat{U}_{\text{sys}}(\Delta t) = \prod_{k=1}^M e^{-i\hat{H}_k\Delta t} + \mathcal{O}(\Delta t^2).$$

It suggests a circuit approach where each time step  $\hat{U}_{\text{sys}}(\Delta t)$  is simulated by  $M$  quantum gates given by  $\hat{U}_k = \exp\{-i\hat{H}_k\Delta t\}$ . This allows for a complex many-body Hamiltonian to be simulated using two body physics. This comes as no surprise given that single qubit rotations and a well chosen two qubit gate form a universal set of gates. The drawback of digital simulations is that a high number of accurate gates are required to faithfully simulate  $\hat{U}_{\text{sys}}$ . Furthermore, it requires good preparation of the input state and a procedure to find out the quantity of interest from the output state. This makes digital quantum simulation almost as hard to perform as building a universal quantum computer.

### 1.2.2 Analogue Quantum Simulations

Analogue quantum simulations rest upon the idea that a simulating system  $\hat{H}_{\text{sim}}$  mimics the dynamics of  $\hat{H}_{\text{sys}}$ . The simulating system should be more controllable than the simulated system and one should be able to create it in a laboratory. An analogue quantum simulation would proceed as follows. First one finds a controllable system with a Hamiltonian  $\hat{H}_{\text{sim}}$  that maps to  $\hat{H}_{\text{sys}}$ . An initial state is prepared and evolved with  $\hat{H}_{\text{sim}}$ . Measurements of the evolved state give information on  $\hat{H}_{\text{sys}}$ . Consider the following example: It is suspected that  $\hat{H}_{\text{sys}}$  possesses a quantum phase transition. However we are unable to simulate it classically. Thus building a system that evolves under  $\hat{H}_{\text{sim}}$ , that maps to  $\hat{H}_{\text{sys}}$ , creates a test lab where one can try and observe the suspected quantum phase transition. One advantage of analogue simulations over digital ones is its advantage to be more resilient against errors. In a digital quantum simulation the gates need to be highly accurate. However in an analogue simulation a quantum phase transition could still be observed even in the presence of noise. For instance neutral atoms trapped in an optical lattice can simulate the transition between a superfluid state and a Mott insulator [12]. The former corresponds to the situation where the atoms are delocalised over the entire optical lattice whilst in the latter each atom is confined to a specific lattice site. Two dimensional Josephson Junctions arrays also provide a versatile framework for analogue quantum simulations [58].

Given their flexibility, circuit QED lattices of superconducting qubits and strip-line resonators provide a flexible architecture for analogue quantum simulations [59]. An electrical network is designed and then quantised producing a specific Hamiltonian whose time evolution we wish to study. In part III of this thesis we show how to reach the regime of ultrastrong multi-mode coupling within circuit QED. This is done with a hybrid transmission line.

We then show how this system can be used as an analogue simulator for the Spin-Boson model.



## Part II

# Optimal Control Theory



# Chapter 2

## Introduction to Optimal Control for Quantum Systems

*The woods are lovely, dark, and deep, ...*

Robert Frost

The last decades have seen the transformation of quantum theory from a mere description of nature to a tool in research and applications, prominently in quantum information processing [1], spectroscopy, sensing, and metrology [60]. Quantum control describes the science of shaping the time evolution of quantum systems in a potentially useful way [53, 54]. The goal of *optimal control* is twofold. Firstly to guide the time evolution of the system under consideration into a desired state or along a specific trajectory. This supposes that the system can be influenced through some external control field, labelled  $\mathbf{u}(t)$ , and that the performance of the time evolution with respect to the objective can be measured using a *fidelity function*. Secondly, optimality is measured with respect to some other quantity. E.g. a time optimal pulse is a pulse performing the desired evolution in the minimum amount of time possible. Control parameters typically are parameters of an external field parametrised in a technologically appropriate way, e.g., into a quantum logic gate [61], into a higher coherence in NMR [52, 62, 63], or into states important for sensing [64]. While analytically accessible only in highly specialised cases, these pulse shapes can in many cases be found using the powerful mathematical technique of Optimal Control Theory (OCT); by solving a Schrödinger or master equation iteratively, a pulse shape producing the desired time evolution can be found [52]. This results in complex pulses that are used in a wide variety of cases.

The following sections introduce how to perform optimal control for quantum systems with an emphasis towards superconducting quantum bits. It

discusses the time evolution of quantum systems and how to measure fidelity functions. Finally the GRAPE algorithm performing the control optimisation based on a gradient search is presented.

## 2.1 Time Evolution of Quantum Systems

At a microscopic level the laws of nature obey the Schrödinger equation

$$i\hbar\partial_t |\psi(t)\rangle = \hat{H}(t) |\psi(t)\rangle. \quad (2.1)$$

The system's state is encoded in the wave function  $|\psi(t)\rangle$  living in the Hilbert space  $\mathcal{H}$ . The Hamiltonian encodes the dynamics; it is a Hermitian matrix whose eigenvalues are the allowed energies of the system. The time evolution from time  $t = 0$  to  $t = T$  is given by the time evolution operator

$$\hat{U}(T, 0) = \mathbb{T} \exp \left\{ -\frac{i}{\hbar} \int_0^T \hat{H}(\tau) d\tau \right\}. \quad (2.2)$$

$\mathbb{T}$  denotes time ordering. The quantum state at  $T$ , starting from  $|\psi(0)\rangle$ , is then  $|\psi(T)\rangle = \hat{U}(T, 0) |\psi(0)\rangle$ . Due to the Hermitian nature of the Hamiltonian the time evolution is unitary and thus reversible since  $\hat{U}^{-1} = \hat{U}^\dagger$ . Many quantum systems cannot be separated from their environment. To include the effect of the latter on the former, a master equation is used. Indeed, the Hilbert space size of the system plus environment is too large for a direct exponentiation of the Hamiltonian to be possible. In many cases a Markov assumption is made so that the time evolution of the density matrix follows  $\rho(t + dt) = \rho(t) + \dot{\rho}dt$ . This means that the correlations between the system and its environment lasting of the order of  $dt$  or longer are neglected. The result is a Master Equation in Lindblad form

$$\dot{\rho}(t) = -\frac{i}{\hbar} [\hat{H}(t), \rho(t)] + \sum_k \hat{L}_k \hat{\rho}(t) \hat{L}_k^\dagger - \frac{1}{2} \left\{ \hat{\rho}(t), \hat{L}_k^\dagger \hat{L}_k \right\}. \quad (2.3)$$

The first part is the Quantum Liouville equation leading to the usual unitary dynamics. The second part describes how the environment acts on the system through the Lindblad operators  $\hat{L}_k$ . The time evolution of the density matrix can be found either by using solvers for differential equations or by vectorisation of the Master equation to obtain a form  $\dot{\vec{\rho}} = \mathcal{S}\vec{\rho}$  which can then be solved by matrix exponentiation as the Schrödinger equation would be. In this case, the time evolved density matrix is given by the Liouville superoperator  $\mathcal{T}(t)$  and reads  $\vec{\rho}(t) = \mathcal{T}(t)\vec{\rho}(0)$  where

$$\mathcal{T}(t) = \mathbb{T} \exp \left\{ \int_0^t \mathcal{S}(\tau) d\tau \right\}. \quad (2.4)$$

The remainder of this work will be restricted to systems evolving either under Schrödinger dynamics or following a Lindblad type Master equation.

### Quantum Channels

A quantum channel  $\mathcal{E}$  is any time evolution that maps a density operator onto another density operator [1]

$$\mathcal{E} : \hat{\rho}_{\text{in}} \mapsto \hat{\rho}_{\text{out}} = \mathcal{E}(\hat{\rho}_{\text{in}})$$

$\mathcal{E}$  is a completely positive trace preserving map. The input state and output states need not necessarily belong to the same Hilbert space, although in most practical cases they do. A channel of particular interest is the completely depolarising channel

$$\Lambda_{\text{dep}}(\hat{\rho}) = p\hat{\rho} + \frac{1-p}{d}\mathbb{1}.$$

It depolarises the state  $\hat{\rho}$  with probability  $1-p$ . A useful representation of quantum channels can be constructed using Choi matrices [65, 66]

$$C_{\mathcal{E}} = \sum_{ij} |i\rangle\langle j| \otimes \mathcal{E}(|i\rangle\langle j|). \quad (2.5)$$

The Jamiolkowski isomorphism is the map  $\mathcal{E} \mapsto C_{\mathcal{E}}$ . This shows that a quantum channel between a  $d_{\text{in}}$  dimensional Hilbert space and a  $d_{\text{out}}$  one can be seen as a density operator in  $d_{\text{in}}d_{\text{out}}$  dimensions. The Choi matrix, however, does not have unit trace like the density operator. In chapter 5, Choi matrices will be used to construct fidelity measures of quantum channels.

## 2.2 Fidelity Measures

There are many different ways to measure the fidelity of a quantum process. Under unitary time evolution, the fidelity can be measured by the gate overlap between the target  $\hat{U}_t$  and the gate implemented by the controls  $\hat{U}$

$$\Phi_{\text{QPT}} = \frac{1}{d^2} \left| \text{Tr} \left\{ \mathbb{P}_{\text{Q}} \hat{U}_t^\dagger \mathbb{P}_{\text{Q}} \hat{U} \right\} \right|^2. \quad (2.6)$$

The projector  $\mathbb{P}_{\text{Q}}$  allows us to consider only the relevant parts of the Hilbert space. For instance, when the individual qubits are built out of a Hilbert space with more than two levels it is often desired to project the time evolution onto the computational subspace, i.e. the space formed by the qubit's

logical  $|0\rangle$  and  $|1\rangle$  states. All gates have to be unitary on this subspace otherwise the quantum system being controlled no longer behaves as a qubit; any population leakage out of the  $|0\rangle$  or  $|1\rangle$  states at the end of the gate will degrade the fidelity [67].  $\Phi_{\text{QPT}}$  is easily computed numerically given that the time evolution operator has to be computed when doing OCT. Experimentally retrieving  $\Phi_{\text{QPT}}$  is done through Quantum Process Tomography (QPT). For  $n$  qubits it requires  $2^{2n}$  input states each measured with  $2^{2n}$  settings [68, 69]. This makes QPT time consuming and unscalable as qubits are added. Additionally the QPT fidelity will be sensitive to state preparation and measurement (SPAM) errors. Both of these issues are overcome by randomised benchmarking (RB), discussed in section 2.2.1. RB provides an alternative fidelity measure based on the average gate fidelity

$$\overline{\mathcal{F}}_{\Lambda, \mathcal{I}} = \int d\hat{V} \langle \psi_0 | \hat{V}^\dagger \Lambda(\hat{V} |\psi_0\rangle\langle\psi_0| \hat{V}^\dagger) \hat{V} | \psi_0 \rangle. \quad (2.7)$$

It measures how close the error channel  $\Lambda$  on a realised Clifford gate is to the identity.  $\Lambda$ 's dynamics can include non-unitary processes. The input state  $|\psi_0\rangle$  can, without loss of generality, be chosen as the ground state. The average gate fidelity measure relates to the concept of twirling. A twirl with respect to a measure  $\boldsymbol{\mu}$  on a set of unitary operators  $\mathcal{U}$  is a mapping between linear superoperators  $\Lambda \mapsto \mathbb{E}_\mu(\Lambda)$  [70] where the operator  $\mathbb{E}_\mu(\Lambda)$  is defined by

$$\mathbb{E}_\mu(\Lambda) : \hat{\rho} \mapsto \int_{\mathcal{U}} d\boldsymbol{\mu}(\hat{V}) \hat{V}^\dagger \Lambda(\hat{V} \hat{\rho} \hat{V}^\dagger) \hat{V}.$$

When evaluating the average gate fidelity  $\overline{\mathcal{F}}_{\Lambda, \mathcal{I}}$  the measure  $\boldsymbol{\mu}$  is chosen to be the uniform probability measure. Thus when sampling the integral, different matrices  $\hat{V} \in \mathcal{U}$  are equally probable. Numerically this integral is computed by building  $\hat{V}$  from a set of uniformly distributed real parameters [71, 72].

There are many more fidelity functions that can be built for quantum gates. These will not be detailed in the work but some additional examples can be found in [52, 73, 74]. The ones shown here will be used throughout the remainder of this work and in some cases new fidelity measures will be defined that are more suited to a given situation.

### 2.2.1 Randomised Benchmarking

In superconducting qubits, quantum process tomography is falling out of favour since evaluating it experimentally is time consuming. However randomised benchmarking is gaining in popularity [75, 76]. It is used to measure

the fidelity of a realised Clifford gate [77, 78]. The essence is to use a random sequence of Clifford gates that compose to unity. Measuring the survival of some input state through many different sequences yields a measure of the average gate fidelity. The fidelity of a specific Clifford gate can be found with Interleaved Randomised Benchmarking [79]. A significant advantage of randomised benchmarking over quantum process tomography is speed and scalability. This section describes how RB works.

### Sequence of Clifford Gates

In experiments a Clifford gate  $\hat{C}_i$  comes with some error  $\Lambda_i$ . The realised channel is  $\Lambda_i \circ \mathcal{C}_i : \hat{\rho} \mapsto \Lambda_i(\hat{C}_i \hat{\rho} \hat{C}_i^\dagger)$  where  $\circ$  denotes composition. Calligraphic script indicates the channel  $\mathcal{C}_i$  associated to the unitary  $\hat{C}_i$ . Consider a sequence  $\mathbf{i}_m = (i_1, \dots, i_m)$  of  $m + 1$  Clifford gates where the last gate inverts the full sequence  $\hat{C}_{i_{m+1}} = (\hat{C}_{i_m} \dots \hat{C}_{i_1})^\dagger$ . Restricting the sequence to Clifford gates, defined in section 1.1.1, makes the protocol scalable since the last gate can be chosen efficiently by the Gottesman-Knill theorem [6]. If each gate were ideal, this sequence would be the identity, but in practice each gate has some associated error. For now, to simplify the argumentation, the error channel  $\Lambda$  is assumed to be time and gate independent. Thus the channel of sequence  $\mathbf{i}_m$  is

$$\mathcal{S}_{\mathbf{i}_m} = \bigcirc_{j=1}^{m+1} \Lambda \circ \mathcal{C}_{\mathbf{i}_j} = \Lambda \circ \left( \bigcirc_{j=1}^m \tilde{\mathcal{C}}_{\mathbf{i}_j}^\dagger \circ \Lambda \circ \tilde{\mathcal{C}}_{\mathbf{i}_j} \right).$$

By  $\tilde{\mathcal{C}}_{\mathbf{i}_j}^\dagger$  it is understood that the corresponding gate is  $\hat{C}_{\mathbf{i}_j}^\dagger$ . The last step is possible because  $\{\mathcal{C}_{\mathbf{i}_j}\}$  forms a group. The procedure to find  $\tilde{\mathcal{C}}_{\mathbf{i}_j}$  from  $\mathcal{C}_{\mathbf{i}_j}$  is shown in [77]. The survival probability of an initial state  $\hat{\rho}_\psi$  through  $\mathcal{S}_{\mathbf{i}_m}$  is

$$F_{\mathbf{i}}(m, \psi) = \text{Tr} \{ E_\psi \mathcal{S}_{\mathbf{i}_m} (\hat{\rho}_\psi) \}. \quad (2.8)$$

$\hat{E}_\psi$  is a positive operator valued measurement. Both  $\hat{E}_\psi$  and  $\hat{\rho}_\psi$  are subject to SPAM errors. In the ideal case  $\hat{E}_\psi = \hat{\rho}_\psi = |\psi\rangle\langle\psi|$ .

### Measuring the Average Error per Gate

To measure how much error  $\Lambda$  introduces,  $K$  sequences  $\mathbf{i}_m$  of  $m$  randomly chosen Clifford gates are applied to a state  $\psi$ . Averaging over the survival probability of  $\psi$ , defined in Eq. (2.8), yields the average sequence fidelity  $F_{\text{seq}}(m, \psi) = \text{Tr} \{ E_\psi \mathcal{S}_m (\hat{\rho}_\psi) \}$ . From linearity of the trace, the average chan-

nel  $\mathcal{S}_m$  is

$$\mathcal{S}_m = \frac{1}{K} \sum_{i=1}^K \mathcal{S}_{i_m} = \Lambda \circ [\mathcal{W}(\Lambda)]^{om}.$$

In the last step, the number of sequences  $K$  should be large enough so that the average superoperator  $\mathcal{S}_m$  is a composition of  $m$  twirls of  $\Lambda$  [80]. The Twirl of  $\Lambda$  over the Clifford group  $\mathcal{C}_n$  is defined as [70]

$$\mathcal{W}_{\text{Clif}}(\Lambda) = \frac{1}{|\mathcal{C}_n|} \sum_{i=1}^{|\mathcal{C}_n|} \hat{C}_i^\dagger \circ \Lambda \circ \hat{C}_i.$$

This operation results in the depolarising channel  $\Lambda_{\text{dep}}$ . Thus  $\mathcal{S}_m$  takes the form  $\Lambda \circ (\Lambda_{\text{dep}})^{om}$ . For the one qubit case, some intuition on  $\mathcal{W}_{\text{Clif}}(\Lambda)$  can be gained by realising that twirling over the Clifford group corresponds to averaging the error channel inserted between a rotation and its inverse. If the error channel is the identity the initial state is recovered. If not, one expects the coherences in the density matrix to vanish and that there should be no probabilistic preference over ground or excited state. This suggests that the output state should be the completely mixed state  $\hat{\rho} = \mathbb{1}_2/2$ . Generally, the twirled channel is the depolarising channel  $\Lambda_{\text{dep}}$  with depolarising probability  $1 - p$  such that its average gate fidelity is the same as that of  $\Lambda$  [81]

$$p + \frac{1-p}{d} = \int d\hat{V} \langle \psi_0 | \hat{V}^\dagger \Lambda(\hat{V} |\psi_0\rangle\langle\psi_0| \hat{V}^\dagger) \hat{V} | \psi_0 \rangle = \overline{\mathcal{F}}_{\Lambda, \mathcal{I}}.$$

Knowing  $p$  gives the average fidelity of  $\Lambda$  and thus the average error per gate. The average sequence acting on an input state is

$$\mathcal{S}_m(\hat{\rho}_\psi) = (\Lambda \circ (\Lambda_{\text{dep}})^{om})(\hat{\rho}_\psi) = \Lambda \left( p^m \hat{\rho} + \frac{1-p^m}{d} \mathbb{I} \right).$$

This gives an expression for the average sequence fidelity

$$F_{\text{seq}}(m, \psi) = p^m \text{Tr} \left\{ E_\psi \left( \Lambda(\hat{\rho}_\psi) - \frac{\mathbb{I}}{d} \right) \right\} + \text{Tr} \left\{ E_\psi \frac{\mathbb{I}}{d} \right\} = Ap^m + B \quad (2.9)$$

This is the zeroth order model of randomised benchmarking. The average sequence fidelity depends on  $p^m$  and the constants  $A$  and  $B$  absorb SPAM errors. The data obtained by measuring  $F_{\text{seq}}(m, \psi)$  for different sequence lengths can be fitted to Eq. (2.9). This yields an experimental measure for  $p$ . Finally the average error per Clifford gate is

$$r = 1 - \overline{\mathcal{F}}_{\Lambda, \mathcal{I}} = 1 - p - \frac{1-p}{d}.$$

This procedure made the assumption that the errors are gate and time independent. This can be overcome and is done in [77]. The crucial insight is that twirling the channel  $\Lambda$  yields a depolarising channel with the same average fidelity as  $\Lambda$ . The overall procedure is sketched in Fig. 2.1.

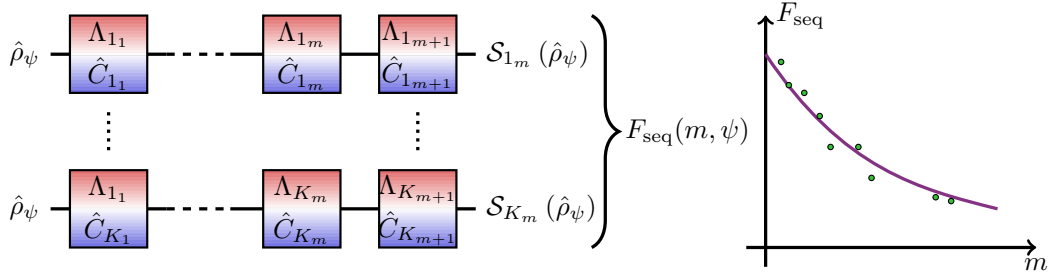


Figure 2.1: Sketch of randomised benchmarking. Each block is a Clifford gate with its associated error channel  $\Lambda_{i_j}$ . The survival of  $\hat{\rho}_\psi$  through  $m$  random Clifford gates is measured for  $K$  gate sequences. Averaging over these  $K$  sequences gives the average survival probability  $F_{\text{seq}}(m, \psi)$ . Plotting the latter as function of  $m$  and fitting the data to a model yields the average error per Clifford gate.

### Interleaved Randomised Benchmarking

The previous section shows how to extract the average gate fidelity of a series of Clifford gates. Interleaved randomised benchmarking [79] can extract the fidelity of a specific Clifford gate of interest. The protocol is the following

1. Perform randomised benchmarking with Clifford gates to get their average error per gate.
2. Repeat the previous step but interleave between each Clifford the gate of interest  $\mathcal{U}$ . This is sketched in Fig. 2.2. The complete sequence should still compose to the identity.

The first step gives the average error per Clifford gate estimated by a depolarising channel with probability  $p$ . The second sequence is equivalent to a depolarising channel with probability  $p_u$ . The error channel  $\Lambda_u$  on the interleaved gate  $\hat{U}$  has an average gate fidelity estimated by

$$\overline{\mathcal{F}}_{\Lambda_u, \mathcal{I}}^{(\text{est})} = 1 - \frac{(d-1)(1-p_u/p)}{d}$$

with  $d$  the dimension of the Hilbert space.

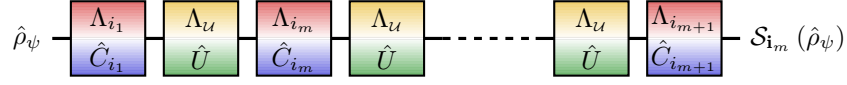


Figure 2.2: Modified gate sequence for interleaved randomised benchmarking.

## 2.3 Pulse Optimisation Algorithms

The strength of OCT is to be able to optimise the fidelity  $\Phi[\mathbf{u}(t)]$  by computing the functional derivative of  $\Phi$  with respect to the controls. Among the different algorithms there is the sequential Krotov algorithm [74] and the concurrent update methods namely GRAPE and a variant based on a quasi Newtonian method BFGS. In this work the GRAPE algorithm [52] with BFGS [82–84] is used.

### GRAPE

Here is described how the gradient ascent pulse shape engineering (GRAPE) algorithm works. The systems considered evolve under unitary dynamics. For superconducting qubits this is a good approximation given that gate times are typically three orders of magnitude faster than the decoherence mechanisms [75]. Such mechanisms could be included [83] in the optimisation but lead to more involved numerics. Instead the effects of decoherence are naturally accounted for when using model free methods, as suggested in chapter 6. To optimise the control field, GRAPE pixelises it into  $N$  piecewise constant controls of length  $\Delta T$ , see Fig. 2.3. The control field  $u_k(t)$  is approximated by

$$u_k(t) \approx c_k(t) = \sum_{j=0}^{N-1} u_{kj} [\Theta(t - j\Delta T) - \Theta(t - (j+1)\Delta T)]$$

where  $\Theta$  is the Heaviside step function and  $u_{kj}$  are the pixels whose values we seek. The Hamiltonian of the system is then separated into a drift and control part

$$\hat{H}(t) = \hat{H}_d + \sum_k c_k(t) \hat{H}_k. \quad (2.10)$$

Each time step  $j$  results in the time evolution operator  $\hat{U}_j = e^{-i\Delta T \hat{H}(j\Delta T)}$  and the total time evolution from 0 to  $T$  is

$$\hat{U} = \prod_{j=N-1}^0 \hat{U}_j.$$

GRAPE proceeds iteratively by updating the controls according to

$$\mathbf{u}_k^{(n)} \rightarrow \mathbf{u}_k^{(n+1)} = \mathbf{u}_k^{(n)} + \varepsilon^{(n)} (\nabla_k \Phi)^{(n)} \quad (2.11)$$

$\mathbf{u}_k^{(n)T} = (u_{k0}^{(n)}, \dots, u_{kN-1}^{(n)})$  is the vector of the pixels of control field  $u_k$  at iteration  $n$ . The gradient of the fidelity at iteration  $n$  is  $(\nabla_k \Phi)^{(n)}$ . The step size  $\varepsilon^{(n)}$  is made variable to speed up convergence and allow the algorithm to make smaller steps when the maximum is almost reached. There are many different fidelity functions that can be used to optimise  $\hat{U}$  [52]. In the subsequent chapters the most often used fidelity function is  $\Phi_{\text{QPT}}$  defined in Eq. (2.6). For this fidelity the gradient with respect to pixel  $j$  of control field  $k$  is

$$\nabla_{kj} \Phi_{\text{QPT}} = \frac{2}{d^2} \text{Re} \left[ \text{Re} \left\{ \mathbb{P}_{\text{Q}} \hat{U}_t \mathbb{P}_{\text{Q}} \frac{\partial \hat{U}}{\partial u_{kj}} \right\} \text{Tr} \left\{ \mathbb{P}_{\text{Q}} \hat{U}_t^\dagger \mathbb{P}_{\text{Q}} \hat{U} \right\} \right].$$

This requires the derivative of the time evolution operator

$$\frac{\partial \hat{U}}{\partial u_{kj}} = \left( \prod_{l=N-1}^{j+1} \hat{U}_l \right) \frac{\partial \hat{U}_j}{\partial u_{kj}} \left( \prod_{l=j-1}^0 \hat{U}_l \right).$$

The derivative of  $\hat{U}_j$  can be expressed in the eigenbasis  $\{|n_j\rangle\}$  of the full Hamiltonian at time step  $j$ . The corresponding eigenvalues are  $\{\lambda_n\}$ . Here we give a few intermediary steps on how to do this. The full detail of the derivation is found in [85]. The starting point is to recognise that

$$\frac{\partial \hat{U}_j}{\partial u_{kj}} = \frac{\partial}{\partial u} \exp \left\{ -i\Delta T \left( \hat{H}(j\Delta T) + u\hat{H}_k \right) \right\} \Big|_{u=0}.$$

The latter is then expressed in the eigenbasis of  $\hat{H}(j\Delta T)$ . Using the definition of the matrix exponential as a power series and setting  $u = 0$  after computing the derivative yields

$$\langle n_j | \frac{\partial \hat{U}_j}{\partial u_{kj}} | m_j \rangle = \sum_{l=0}^{\infty} \frac{(-i\Delta T)^l}{l!} \sum_{q=1}^l \lambda_n^{q-1} \langle n_j | \hat{H}_k | m_j \rangle \lambda_m^{l-q}.$$

This steps makes explicit use of the orthogonality of the eigenvectors of a Hermitian matrix. Rearranging the terms yields the final analytic expression for the gradient

$$\langle n_j | \frac{\partial \hat{U}_j}{\partial u_{kj}} | m_j \rangle = -i\Delta T \langle n_j | \hat{H}_k | m_j \rangle \begin{cases} e^{-i\Delta T \lambda_n} & n_j = m_j \\ \frac{e^{-i\Delta T \lambda_n} - e^{-i\Delta T \lambda_m}}{-i\Delta T (\lambda_n - \lambda_m)} & \text{otherwise} \end{cases}.$$

This last equation gives us the means of analytically performing the update rule (2.11) without having to resort to time consuming numerical estimations of the gradient.

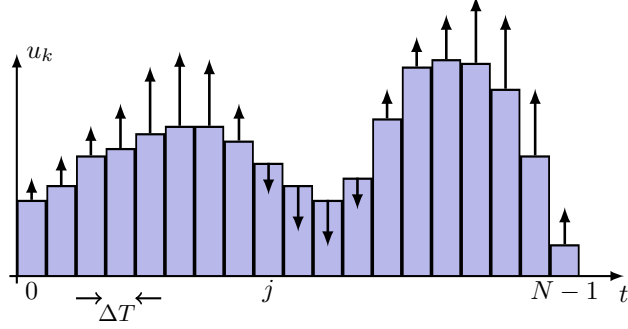


Figure 2.3: Illustration of the GRAPE algorithm update for a control field. Each pixel  $u_{kj}$  is updated at each iteration by an amount proportional to the derivative of the fidelity with respect to that pixel.  $\nabla_{kj}\Phi$  is indicated by the arrows whilst the bars correspond to the values of the pixels  $u_{kj}$  at iteration  $n$ .

### 2.3.1 BFGS

Newton's method searches for the extrema of a function through a series of quadratic approximations. The insight is that if a function  $f$  is quadratic then from any point  $x_n$  one can reach the extrema  $f'(x) = 0$  by performing a step of size  $\Delta x = x_n - f'(x_n)/f''(x_n)$ . When extending to multi-variable functions the second derivative is replaced with the inverse Hessian matrix. Quasi-Newton methods, such as the Broyden-Fletcher-Goldfarb-Shanno (BFGS) method, rely on the same principle but use an approximation of the Hessian matrix. When searching for optimal controls, the convergence speed can be increased by modifying the update rule of Eq. (2.11) so that the step size is determined by the curvature of the control landscape. This results in the quasi-Newtonian BFGS update rule

$$\mathbf{u}_k^{(n)} \rightarrow \mathbf{u}_k^{(n+1)} = \mathbf{u}_k^{(n)} + H_n^{-1}(\nabla_k\Phi)^{(n)}. \quad (2.12)$$

The inverse Hessian  $H_n$  is given by the update rule

$$H_{n+1}^{-1} = H_n^{-1} - \frac{H_n^{-1}yx^T - xy^TH_n^{-1}}{y^Tx} + \frac{xy^TH_n^{-1}yx^T}{(y^Tx)^2} + \frac{xx^T}{y^Tx} \quad (2.13)$$

where  $x = \text{vec } \mathbf{u}_k^{(n)} - \text{vec } \mathbf{u}_k^{(n-1)}$  is the vectorised difference in all control fields between iteration  $n - 1$  and  $n$ . Similarly  $y = \text{vec } (\nabla_k\Phi)^{(n)} - \text{vec } (\nabla_k\Phi)^{(n-1)}$ .

## 2.4 Summary

Closed quantum systems follow unitary dynamics according to the Schrödinger equation (2.1). Open quantum systems are described by a density operator whose dynamics, in the Markovian case, follows a Lindblad master equation (2.3). The dynamics resulting from a control pulse can be compared to a target time evolution using various fidelity functions. This fidelity function can be improved by means of the GRAPE algorithm. Its main steps are

1. Initial pulse guess  $u_k(t)$
2. Compute the time evolution  $\hat{U}$  and corresponding fidelity  $\Phi$
3. Compute the derivatives  $\nabla_k \Phi$
4. Perform the update rule corresponding either to GRAPE (2.11) or BFGS (2.12) and (2.13).
5. Iterate starting from point 2.



# Chapter 3

## Few Parameter Pulses

The work presented in this chapter shows how, in a selected important situation, average Hamiltonian theory can be used to help find analytic pulse shapes. Such pulse shapes are functions with a small number of parameters and as a consequence are easier to implement since they can be calibrated by manually tuning a or a few parameters. This will be illustrated within the framework of 3D transmons where the gain in coherence time comes at a cost in controllability. This is strongly felt when more than one qubit is in the cavity. Spectral crowding refers to transitions coming too close to address them individually. Now with the limited control, even if the logical transitions are well-spaced, crowding can occur between logical and leakage transitions, e.g., if the logical transition of the first qubit is close in frequency to the leakage transition, the transition between a computational and a non-computational state, of the second qubit. For example when performing an  $\hat{X}$  gate on the first qubit, leakage to second qubit's  $|2\rangle$  state will occur. Although high fidelity gates have been demonstrated with single junction transmons in the 2D architecture [55] spectral crowding will limit the gate fidelity in 3D architectures. In order to mitigate spectral overlap, the Derivative Removal by Adiabatic Gate (DRAG) technique has been developed [38, 86]. We will apply this technique to the problem at hand and show that on its own it is of limited success. We will then combine DRAG with a sideband drive to show how to do these single-qubit gates fast.

In this work we thus address the issue of spectral crowding with optimal control theory methods. To better illustrate the problem and show the effec-

---

Chapter published in “R. Schutjens, F. Abu Dagga, D. J. Egger & F. K. Wilhelm, Phys. Rev. A **88**, 052330 (2013)”. The main discovery of the Wah-wah pulse was made by F. Abu Dagga, R. Schutjens finalised the work. D. J. Egger provided research insight, pulse robustness analysis and supervision.

tiveness of the analytical pulses we introduce specific gate fidelity functions in section 3.2. In section 3.3 we demonstrate the limitations of the DRAG technique alone for this problem. We then present an analytical pulse, found through the Magnus expansion [87], capable of minimising leakage out of the computational subspace of both qubits in section 3.4.

### 3.1 Frequency Crowded Transmons

Optimised superconducting qubits such as 3D transmons are well described by weakly anharmonic oscillators [38, 88]. A realistic model of the qubit has to take at least one extra non-computational level (a *leakage level*) into account [76, 89, 90]. This is reflected in the following Hamiltonian for two superconducting transmon qubits in a common 3D cavity

$$\hat{H}(t) = \sum_{k=1}^2 \left[ \omega_k \hat{n}_k + \Delta_k \hat{\Pi}_2^{(k)} \right] + \Omega(t) \sum_{j=1}^2 \left[ \lambda_j^{(1)} \hat{\sigma}_{j,j-1}^{x(1)} + \lambda_j^{(2)} \hat{\sigma}_{j,j-1}^{x(2)} \right]. \quad (3.1)$$

The  $0 \leftrightarrow 1$  transition frequency and number operator of qubit  $k$  are, respectively,  $\omega_k$  and  $\hat{n}_k = \sum_j j |j\rangle\langle j|^{(k)}$ . We call the transition from the excited state  $|1\rangle$  to the extra state  $|2\rangle$  the leakage transition. It is detuned from  $\omega_k$  by the anharmonicity  $\Delta_k$ . In the remainder of this work we assume  $\Delta_1 = \Delta_2 = \Delta$ . The projectors on the energy levels of transmon  $k$  are  $\hat{\Pi}_j^{(k)} = |j\rangle\langle j|^{(k)}$ . The terms coupling adjacent energy levels of qubit  $k$  are

$$\hat{\sigma}_{j,j-1}^{x(k)} = |j\rangle\langle j-1|^{(k)} + |j-1\rangle\langle j|^{(k)}$$

and

$$\hat{\sigma}_{j,j-1}^{y(k)} = i |j\rangle\langle j-1|^{(k)} - i |j-1\rangle\langle j|^{(k)}.$$

$\Omega(t)$  is the drive field and is applied simultaneously to both qubits. The strength at which  $\Omega(t)$  drives the  $1 \leftrightarrow 2$  transition relative to the  $0 \leftrightarrow 1$  is given by  $\lambda_j^{(k)}$ . Table 3.1 show the variables and numerical values used in simulations [91].

Qubits are usually addressed by frequency selection through pulses tuned to the respective qubit level splitting. This is necessary whenever the control field cannot be selectively focused on individual qubits as is the case for multiple 3D transmons in the same cavity. An eventual implementation of a quantum computer will consist of many such qubits, probably a whole register in one cavity. The problem to distinguish different qubits can thus be seen as a problem of spectral crowding. In transmon systems this can lead to the  $0 \leftrightarrow 1$  transition of the first qubit being very close to the  $1 \leftrightarrow 2$  transition of

Table 3.1: System parameters as shown in Eq. (3.1).

	Qubit 1	Qubit 2	
$\omega_k/2\pi$	5.508	5.903	GHz
$\Delta/2\pi$	-350	-350	MHz
$\lambda_1^{(k)}$	1	1	
$\lambda_2^{(k)}$	$\sqrt{2}$	$\sqrt{2}$	

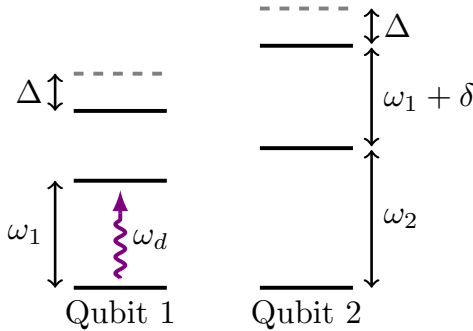


Figure 3.1: Level diagram of the two qubits. The driving field is set to have the same frequency as the  $0 \leftrightarrow 1$  transition of first qubit which we wish to drive. Requiring that the same transition of the second qubit be far detuned results in its leakage transition being only slightly detuned by  $\delta$  with  $0 \leftrightarrow 1$  of first qubit.

the second qubit. The frequency difference of these two transitions is named  $\delta$ . With  $\delta/2\pi = 45$  MHz, the leakage transition of qubit two is closer to the driving fields frequency than the leakage transition of qubit one detuned by  $\Delta/2\pi = -350$  MHz. The situation is depicted in Fig. 3.1.

The second term in Eq. (3.1) is the control Hamiltonian, described as a semiclassical dipolar interaction between the qubits and the classical cavity field

$$\Omega(t) = \Omega_X(t) \cos(\omega_d t) + \Omega_Y(t) \sin(\omega_d t).$$

Both quadrature envelopes can be modulated separately. In the remainder of this work, we assume resonance between the drive and qubit 1, i.e.  $\omega_d = \omega_1$ . Single quadrature pulses employ Gaussian shapes  $\Omega_g$  due to their limited bandwidth [86]. To remove fast oscillating terms we move to another reference frame and invoke the rotating wave approximation (RWA). The transformation into an appropriate frame is accomplished by the time-dependent unitary  $\hat{R}$  that acts on the Hamiltonian as

$$\hat{H}^R = \hat{R}\hat{H}\hat{R}^\dagger + i\dot{\hat{R}}\hat{R}^\dagger. \quad (3.2)$$

Here,  $\hat{R}(t) = \left(\sum_j e^{-i\omega_j^{(1)}t}\hat{\Pi}_j^{(1)}\right) \otimes \left(\sum_j e^{-i\omega_j^{(2)}t}\hat{\Pi}_j^{(2)}\right)$ . Transformations into this type of frame can lead to either the rotating frame with respect to the drive  $\omega_d$  or the interaction frame by choosing  $\omega_j^{(l)} = j\omega_d$ ,  $\omega_j^{(l)} = j\omega^{(l)} + \Delta_j^{(l)}$  respectively. Here, we choose the former. In the rotating frame, we use

the RWA to neglect the fast oscillating terms such as  $\pm 2\omega_d$ . The system's original Hamiltonian, given by Eq. (3.1), is now

$$\begin{aligned} \hat{H}^R = & \Delta \hat{\Pi}_2^{(1)} + (\delta - \Delta) \hat{\Pi}_1^{(2)} + \delta \hat{\Pi}_2^{(2)} + \frac{\Omega_X(t)}{2} \sum_{j=1}^2 \left[ \lambda_j^{(1)} \hat{\sigma}_{j,j-1}^{x(1)} + \lambda_j^{(2)} \hat{\sigma}_{j,j-1}^{x(2)} \right] \\ & + \frac{\Omega_Y(t)}{2} \sum_{j=1}^2 \left[ \lambda_j^{(1)} \hat{\sigma}_{j,j-1}^{y(1)} + \lambda_j^{(2)} \hat{\sigma}_{j,j-1}^{y(2)} \right]. \end{aligned} \quad (3.3)$$

## 3.2 Single Qubit Gates

We aim at applying, up to a global phase  $\phi$ , a gate on the first qubit without affecting the second one  $\hat{U}_t = e^{i\phi} \hat{U}^{(1)} \otimes \mathbb{1}$ . Unless otherwise specified  $\hat{U}^{(1)}$  is an  $\hat{X}$ -gate. A specific control pulse of duration  $T$  results in a final gate given by  $\hat{U}$ . The fidelity with which a control pulse meets the target gate is measured by Eq. (2.6). We will also investigate single-qubit gates that shift the phase of the second qubit. Such gates can be made more efficiently and we later show how to correct the phase. They can be studied using the reduced fidelity functions

$$\Phi_{|*,i\rangle} = \frac{1}{2^2} \left| \text{Tr}_{\{|0,i\rangle,|1,i\rangle\}} \left\{ \hat{U}_t^\dagger \hat{U}(T) \right\} \right|^2. \quad (3.4)$$

The trace is taken over states where the second qubit is exclusively in  $|0\rangle$  or  $|1\rangle$ . A gate producing a good  $\Phi_{|*,i\rangle}$  has qubit 2 starting and ending in state  $|i\rangle$ . The average of the  $\Phi_{|*,i\rangle}$ 's gives a fidelity function insensitive to the phase of the second qubit

$$\Phi_{\text{avg}} = \frac{1}{2} (\Phi_{|*,0\rangle} + \Phi_{|*,1\rangle}). \quad (3.5)$$

In other words,  $\Phi_{\text{avg}}$  is maximal if  $\hat{U}(T)$  (in the computational subspace of the two qubits) has the form

$$\hat{U}(T) = e^{i\alpha} \begin{bmatrix} 0 & 1 \\ 1 & 0 \end{bmatrix} \otimes \begin{bmatrix} 1 & 0 \\ 0 & e^{i(\gamma-\alpha)} \end{bmatrix}. \quad (3.6)$$

For a given gate time the phase error can be calculated and subsequently corrected as this gate is not entangling. In fact, an entangling gate would be detected by deteriorating  $\Phi_{\text{avg}}$  and given that the qubit controls are local and the two qubits are uncoupled, no entanglement is generated.

### 3.3 Applying DRAG

The DRAG method [38, 86, 92] strongly reduces leakage to the  $|2\rangle$  state with a two quadrature drive. Here we show that this method does not provide a sizeable improvement over a single Gaussian envelope. We transform  $\hat{H}^R$  a second time along the lines of Eq. (3.2) using the transformation matrix

$$\hat{V}(t) = \exp\left(-i\frac{\Omega_X}{2\beta} \sum_{j=1}^2 \left[\lambda_j^{(1)} \hat{\sigma}_{j,j-1}^{y(1)} + \lambda_j^{(2)} \hat{\sigma}_{j,j-1}^{y(2)}\right]\right).$$

This is the two-qubit version of the DRAG transformation [86, 92]. The parameter  $\beta$  selects which transition is suppressed. A first order expansion in  $\eta = \Omega_X(t)/\beta \ll 1$  gives

$$\hat{H}^V = \hat{H}_{\text{diag}} + \hat{H}_Y + \hat{H}_X^{(1)} + \hat{H}_X^{(2)}$$

The diagonal terms are of  $O(\eta^2)$ , hence  $\hat{H}_{\text{diag}}$  is neglected on our level of approximation.  $\hat{H}_Y$  contains a term generated by the time-derivative in Eq. (3.2) as well as the  $Y$  drive

$$\hat{H}_Y = \left(\frac{\Omega_Y(t)}{2} + \frac{\dot{\Omega}_X(t)}{2\beta}\right) \sum_{j=1}^2 \left[\lambda_j^{(1)} \hat{\sigma}_{j,j-1}^{y(1)} + \lambda_j^{(2)} \hat{\sigma}_{j,j-1}^{y(2)}\right].$$

$\hat{H}_Y$  can be suppressed by choosing  $\Omega_Y(t) = -\dot{\Omega}_X(t)/\beta$ . This is the essence of the DRAG method [38]. The last two terms respectively drive the first and second qubit according to

$$\begin{aligned} \hat{H}_X^{(1)}(t) &= \Omega_X(t) \hat{\sigma}_{10}^{x(1)} + \lambda \frac{\beta - \Delta}{2\beta} \Omega_X(t) \hat{\sigma}_{21}^{x(1)} + \frac{\lambda \Delta}{8\beta^2} \Omega_X(t)^2 \hat{\sigma}_{20}^{x(1)}, \\ \hat{H}_X^{(2)}(t) &= \eta \frac{\beta - \delta + \Delta}{2\beta} \Omega_X(t) \hat{\sigma}_{10}^{x(2)} + \eta \lambda \frac{\beta - \delta}{2\beta} \Omega_X(t) \hat{\sigma}_{21}^{x(2)} + \frac{\eta^2 \lambda \Delta}{8\beta^2} \Omega_X^2(t) \hat{\sigma}_{20}^{x(2)}. \end{aligned}$$

Depending on the value of  $\beta$  a specific off resonant transition can be suppressed. If  $\beta = \delta$  the second qubit leakage transition is removed. However, since  $\delta < \Delta$  (by a factor  $> 7$  for the numbers in table 3.1) the compensation field  $\Omega_Y$  becomes large and strongly drives the other leakage transitions, i.e., introduces errors of a size comparable to what it is suppressing. Note, that for fast pulses with  $\beta = \delta$  the perturbation expansion in [38, 86, 92] naturally breaks down. Selecting  $\beta = \Delta$  suppresses the leakage transition of the first qubit, but does not solve the leading spectral crowding issue based on the smallness of  $\delta$ . We are explicitly highlighting this in Fig. 3.2. It shows the

fidelity, as a function of gate time, for the single quadrature Gaussian (thin lines) and DRAG (thick lines) solutions with  $\beta = \Delta$ .

The difference between the fidelity function  $\Phi_{\text{QPT}}$ , Eq. (2.6), and the special fidelity functions  $\Phi_{|*,i\rangle}$  and  $\Phi_{\text{avg}}$ , Eq. (3.4) and (3.5), show that while it is difficult to perform an  $\hat{X}$  gate on qubit 1 without affecting qubit 2, we can implement a high fidelity  $\hat{X}$  gate with an additional phase shift on the other qubit for  $T > 42$  ns. This marks a time limitation that for DRAG alone to produce a high-fidelity gate the time needs to be at least on the boundaries of the adiabatic regime.

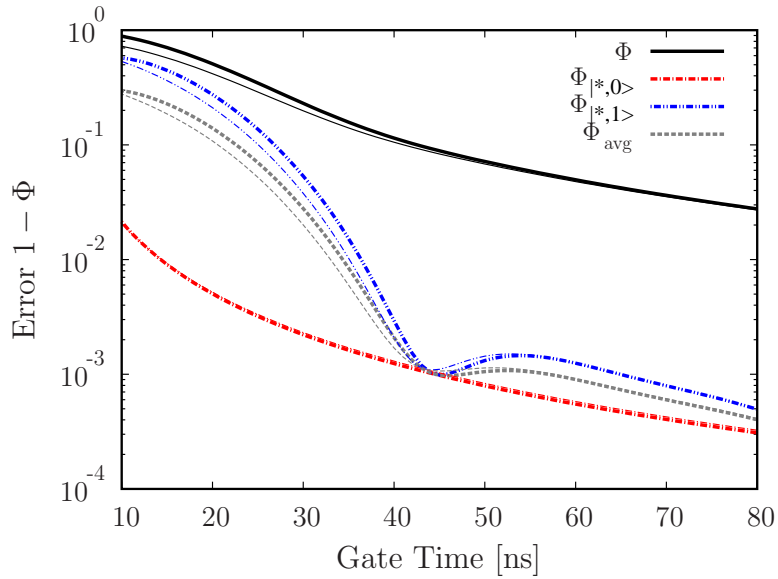


Figure 3.2: Error for a single control with a Gaussian pulse shape as a function of gate time and a single quadrature (thin lines) and for the DRAG method with  $\beta = \Delta$  (thick lines). The DRAG method gives only marginal improvements over the single quadrature Gaussian pulse shape for  $\Phi_{\text{avg}}$  which is slightly lower at the dip around 42 ns. The DRAG solution shown here is the optimal from picking  $\beta \in \{\Delta, \delta, \delta - \Delta\}$ .

### 3.4 Magnus Expansion

Here we show how to find an improved pulse capable of performing the desired gate faster and with better fidelity. The full effect of system and Hamiltonian is described by the time evolution operator defined in Eq. (2.2). This can in general not be computed in closed form even for driven two-state systems with notable exceptions [93]. Still being unitary, the solution of Eq. (2.2)

can be written as the exponential of an Hermitian matrix [87]. An expansion in this effective Hamiltonian gives the Magnus expansion

$$\hat{U}(T) = e^{-i \sum_k \hat{\Theta}_k(T)}. \quad (3.7)$$

The equation above still requires exponentiating a matrix. However the absence of time ordering considerably simplifies the derivation of an explicit expression for  $\hat{U}$ . The Magnus expansion is asymptotic. Here, it converges quickly as nested integrals lead to cancellations of fast oscillating terms. The constraints on the controls set by the zeroth order in the expansion will thus be most important. The first terms in the expansion are given by [87]

$$\begin{aligned} \hat{\Theta}_0(T) &= \int_0^T dt \hat{H}(t), \\ \hat{\Theta}_1(T) &= -\frac{i}{2} \int_0^T dt_2 \int_0^{t_2} dt_1 [\hat{H}(t_2), \hat{H}(t_1)]. \end{aligned}$$

$[\hat{H}(t_2), \hat{H}(t_1)]$  is the commutator of the Hamiltonian at different times. Higher order terms in the expansion can be worked out as nested commutators similar as those shown above.

We start with the system in the interaction frame (the transformation is given in section 3.1)

$$\hat{H}^I = \frac{\Omega_C}{2} \sum_{j=1}^2 \left[ \lambda_j^{(1)} e^{-i\delta_j^{(1)}t} |j-1\rangle\langle j|^{(1)} + \lambda_j^{(2)} e^{-i\delta_j^{(2)}t} |j-1\rangle\langle j|^{(2)} \right] + \text{h.c.}$$

Here we have combined  $\Omega_C = \Omega_X + i\Omega_Y$  and set  $\delta_1^{(1)} = 0, \delta_2^{(1)} = \Delta, \delta_1^{(2)} = \delta - \Delta$ , and  $\delta_2^{(2)} = \delta$ . In the interaction frame, the Hamiltonian is purely off-diagonal and the desired gate is changed by a phase on the  $|1\rangle$  state of the second qubit. This phase is known since any unitary transformation  $\hat{V}(t)$ , transforms the time evolution following  $\hat{U}^V(T) = \hat{V}(T) \hat{U}(T) \hat{V}^\dagger(0)$ . In Eq. (3.8)  $U_F$  transforms in this way. If the zeroth order term is to implement the gate, the control problem becomes

$$\hat{U}_F = e^{-i\hat{\Theta}_0} = e^{-i \int_0^T dt \hat{H}^I(t)}. \quad (3.8)$$

As an aside, this highlights why  $\Theta_0/T$  is often called the average Hamiltonian and  $\sum_k \hat{\Theta}_k(T)/T$  the effective Hamiltonian in NMR [87]. This and the form

$\hat{H}^I$  imposes restrictions on the control  $\Omega_C$

$$\frac{1}{2} \int_0^T dt \Omega_C = \pi \quad (3.9)$$

$$\frac{1}{2} \int_0^T dt e^{-i\Delta t} \Omega_C = 0 \quad (3.10)$$

$$\frac{1}{2} \int_0^T dt e^{-i\delta t} \Omega_C = 0 \quad (3.11)$$

$$\frac{1}{2} \int_0^T dt e^{-i(\delta-\Delta)t} \Omega_C = 0 \quad (3.12)$$

These constraints are the Fourier transforms of the control evaluated at the different detunings in the system as is familiar from spectroscopy at weak driving [87, 94–96] but here derived under intermediate-to-strong drive conditions. They state that the control should contain no power at the off-resonant frequencies. If  $\Omega_C$  is palindromic the complex conjugated equations are also satisfied. If equations (3.9-3.12) are met, the final unitary evolution will be  $e^{i\phi} \hat{\sigma}_x \otimes \mathbf{1}$ .

So that the zeroth order implements the gate, higher order terms have to be zero. Here is an example of the first order term  $\hat{\Theta}_1$ . It only gives extra terms on the diagonal and the  $0 \leftrightarrow 2$  transition. This calculation is quite involved and here is an example of the term involving  $|01\rangle\langle 01|$  (neglecting terms oscillating faster than  $\delta$ )

$$\begin{aligned} \langle 01 | \hat{\Theta}_1(T) | 01 \rangle &= \frac{1}{4} \int_0^T dt_2 \int_0^{t_2} dt_1 \Omega(t_1, t_2) \\ &\quad \times [1 + \cos(\delta(t_1 - t_2)) - \sin(\delta(t_1 - t_2))], \end{aligned}$$

with  $\Omega(t_1, t_2) = \Omega_X(t_2)\Omega_Y(t_1) - \Omega_X(t_1)\Omega_Y(t_2)$ . In the spirit of the Magnus expansion, all slow oscillating terms have the form above and are negligible if their integral is small. This suggest a control pulse where  $\Omega_X$  is modulated with a sinusoidal function

$$\begin{aligned} \Omega_X &= A_\pi e^{-\frac{1}{2\sigma^2}(t-\frac{T}{2})^2} \left( 1 - A \cos \left[ \omega_x \left( t - \frac{T}{2} \right) \right] \right), \\ \Omega_Y &= -\frac{1}{\beta} \dot{\Omega}_X. \end{aligned} \quad (3.13)$$

This is a Gaussian with added sideband modulation on the in-phase part  $\Omega_X$  supplemented by DRAG on the quadrature  $\Omega_Y$ . A frequency modulation with  $\cos(\omega_x t)$  for a bandwidth of  $\Omega_g < 2\omega_X$  can be seen as adding an effective

drive at  $\omega_X$  proportional to  $\Omega_g$ . This added drive can be used to counteract the population transfer of a specific transition. The absolute errors of Eqs. (3.10-3.12) are minimised by varying  $A, \omega_x, \beta$  yielding a pulse with a sideband modulation of  $\delta/2$

$$\begin{aligned}\Omega_X &= A_\pi e^{-\frac{18}{T^2}(t-\frac{T}{2})^2} \left( 1 - \cos \left( \frac{\delta}{2} \left( t - \frac{T}{2} \right) \right) \right), \\ \Omega_Y &= -\frac{1}{2\Delta} \dot{\Omega}_X.\end{aligned}\tag{3.14}$$

Here we chose  $\sigma = T/6$ . The factor of 2 in the denominator of  $\Omega_Y$  comes from the absence of control over the qubit frequency [86]. This is shown experimentally in ref. [97, 98]. The pulse is shown in Fig. 3.3 for  $T = 17$  ns and other parameters given by the values in table 3.1. In order for the pulse to produce the  $X$  gate  $A_\pi$  should be chosen so that relation (3.9) is satisfied. Given the shape of the pulse, we nickname this shape Weak AnHamonicity With Average Hamiltonian, WAHWAH [99].

### 3.4.1 Sideband Modulation

The solid black line in Fig. 3.4 shows the error of pulse (3.14) as function of gate time. Compared to the Gaussian and DRAG results, the error has a minimum (4%) at a shorter gate time, around 20 ns. The reduced fidelity functions  $\Phi_{|*,i\rangle}$  (red and blue lines) and  $\Phi_{\text{avg}}$  (grey line) give additional insight by allowing a phase shift on qubit 2. Comparing to Fig. 3.2, it is seen that the sideband modulated pulse attains a high fidelity ( $> 99.9\%$ ) in less than half the time (17 ns compared to 42 ns) of the Gaussian or DRAG solutions. The  $1 \leftrightarrow 2$  transition of the second qubit is still the limiting factor since the reduced error  $1 - \Phi_{|*,1\rangle}$  is always the biggest. Nonetheless for a specific gate time a high fidelity is possible.

The state populations during the pulse reveal the underlying mechanism. Figure 3.5 shows the populations for gate times 17 and 20 ns. In the latter there is still a net population in the  $|2\rangle$  state of the qubit 2 after the gate.

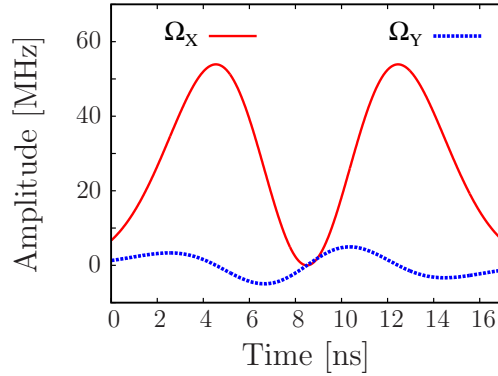


Figure 3.3: Example of the control functions of Eq. (3.13) for  $T = 17$  ns. The amplitude of  $\Omega_X$  is somewhat smaller than for a Gaussian only pulse used in figure 3.2.

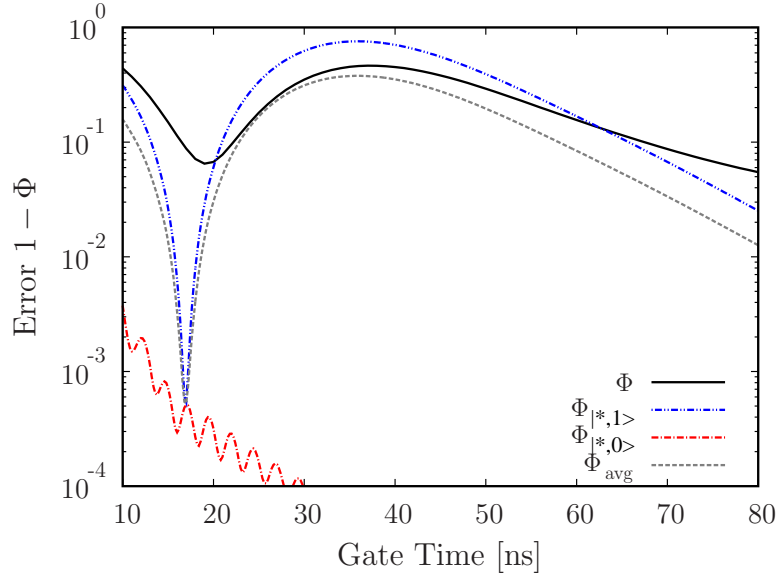


Figure 3.4: Error as a function of gate time for the pulse with sideband modulation. The target gate is  $\hat{\sigma}_x \otimes \mathbf{1}$ . At  $T \sim 17$  ns,  $\Phi_{\text{avg}}$  reaches a maximum. The gate fidelity functions are defined in Eqs. (2.6), (3.4) and (3.5).

For the former, there is no net change to the second qubit at the end. This suggests that the drive on the second qubit makes it perform a closed transition cycle in the  $(|1\rangle, |2\rangle)$  subspace, thus acquiring a local phase.

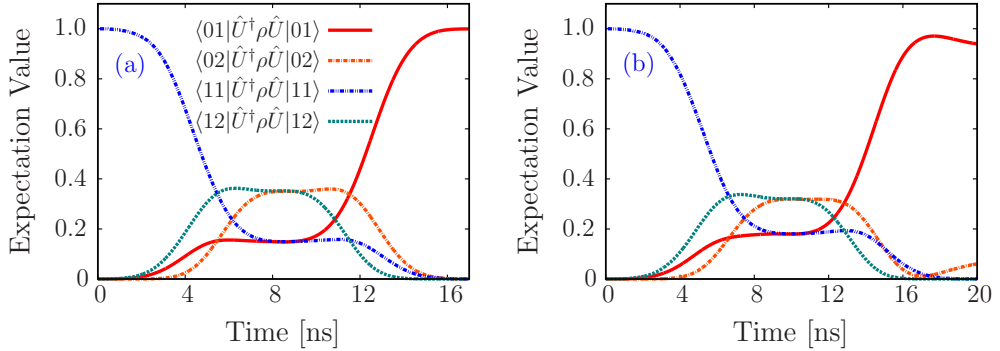


Figure 3.5: Populations of the states during the pulse sequence of Eq. (3.14) for gate time of 17 ns (a), and 20 ns (b). At 20 ns the pulse sequence clearly leaves part of the excitation in the  $\{|1\rangle, |2\rangle\}$  subspace of qubit two, while at 17 ns the trajectory is optimal in the sense that no net population transfer is present on qubit two.

Finally we note in this section that the method worked out here is not the

only way to determine new analytical results for pulse shapes. In general, the different terms of Eq. (3.7) need to combine into the correct gate in some manner, whereas we have enforced that this combination consists of all terms beyond the lowest one to vanish. Our approach has the advantage that it produces an intuitive result, providing frequency selectivity criteria Eqs. (3.9,3.10,3.11,3.12) in the form of the Fourier transform of the driving pulse.

### 3.4.2 Phase Correction

The average reduced fidelity (3.5) is insensitive to the phase of the second qubit and leads to a gate of the form of Eq. (3.6). This phase error does not influence population measurements after the gate; only the  $X$  and  $Y$  component have different contributions. The global phase  $\alpha$  and the phase error  $\gamma$  for specific gate times are plotted in Fig. 3.6. One can correct for this error in multiple ways. If there is a  $Z$  control available on the separate qubits [45] one can simply compensate the phase following

$$\frac{\pi}{2} = \int Z_1(t) dt$$

$$\alpha(T) = \int Z_2(t) dt$$

Instead of compensating the qubit phase, one can adjust the phase of the next gate in the  $XY$ -plane accordingly. This is possible because the phase error is constant given a set gate time, as shown in Fig. 3.6. In essence this is the same as changing the frame in the  $XY$  plane according to

$$X' = \cos(\alpha(T))X + \sin(\alpha(T))Y$$

$$Y' = -\sin(\alpha(T))X + \cos(\alpha(T))Y.$$

This technique is analogous to phase ramping as described in Refs. [38, 86] The phases in the leakage states are irrelevant, it is thus sufficient to correct the computational subspaces of the qubits individually.

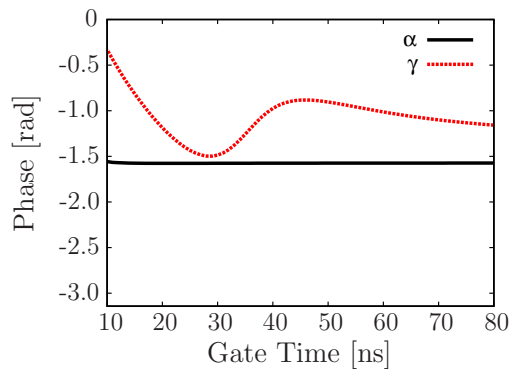


Figure 3.6: Phases as defined in Eq. (3.6) of the gate with the control sequence from Eq. (3.14). It is by these phases that the qubits or the subsequent gates need to be corrected.

### 3.4.3 Experimental Protocol

The procedure to implement the pulse on an actual experiment is

- Use spectroscopy to determine the qubit frequencies, yielding  $\delta$  and  $\Delta$ .
- Equation (3.14) gives the shape of the pulses for all possible gate times  $T$ . The normalisation parameter  $A_\pi$  is chosen so that the area theorem, Eq. (3.9), is satisfied, which in general requires numerical root finding.
- The gate time  $T$  is chosen so that the pulse sequence optimises the reduced average fidelity defined by Eq. (3.5).
- With the gate time known, the phase offset  $\alpha(T)$  is computed, so that it can be corrected according to the procedures given in section 3.4.2.

## 3.5 Conclusions

We have found numerical as well as analytical pulse shapes implementing single qubit gates in a 3D cavity coupled to two single junction Transmons. Such qubits are typically hindered by spectral crowding whereby leakage transitions lie close in frequency to main qubit  $0 \leftrightarrow 1$  transitions. We combine average Hamiltonian theory for arbitrary waveforms with the DRAG methodology. This shows that it is possible to find better controls using a sideband modulation.

# Chapter 4

## Multiparameter Pulses

The previous chapter showed a case where the target gate can be reached using an analytical pulse derived based on frequency selection criteria. The following chapter presents a case where there is significant gain in using a numerical pulse where each pixel is an individual parameter. These numerical pulses can be significantly faster. This is a big gain since gate speed helps mitigate the effects of decoherence. Additionally if a full scale quantum computer were to be built many quantum operations have to be performed and thus gate speed is crucial to limit computation times [100]. Furthermore, numerical pulses are designed with the full Hamiltonian; they don't require certain approximations to be made so that an analytical understanding of the pulse can be reached. In some cases this allows the pulse to reach a higher intrinsic fidelity.

In this chapter we show how OCT can improve on the analytical Wah-Wah pulse of chapter 3. The resulting pulses can be of arbitrary speed and don't suffer the phase problem. However, the main focus of this chapter will be to apply optimal control to find a fast and accurate pulse shape to speed up a controlled-Z gate between two qubits connected by a resonator [101–110]. The setting is motivated by superconducting qubits but has analogies in atomic physics [111], quantum dot [112, 113], and other resonator-based systems. We demonstrate the feasibility of these pulses by taking into account bandwidth limitations imposed by the experiment and provide a methodology for removing systematic errors that can practically affect the application of the control pulse. In chapter 4.2 we describe the system setting as well as conventional analytic methods [114] to create CZ gates. Here we show that those constructions are strongly limited by low qubit anharmonicity. Sec. 4.3 describes the implementation of optimal control to this system and its

results and Sec. 4.4 discusses potential error sources and their mitigation.

## 4.1 Numerical Optimised Wah-Wah Pulses

By using numerical methods one can go beyond the analytic methods discussed in the last chapter. Here is discussed how further improvements can be made with the GRAPE algorithm. The system of Eq. (3.3) is numerically optimised using the parameters in Tab. 3.1. Figure 4.1(a) is an example of a short (4 ns) high fidelity (99.999%) GRAPE pulse. This pulse has  $T \ll \pi/\delta$  and therefore the smallest spectral crowding frequency scale  $\delta$  does not impose a quantum speed limit. The limit rather seems to be set by the number of control parameters available. E.g., we have verified that if the size of a time step is 1 ns as in current experimental equipment, the shortest possible time is 8 ns. From numerical results we have not observed a quantum speed limit. By decreasing the gate time the pulse can be shortened at the expense of higher amplitudes. The pulse in figure 4.1(a) has large amplitudes at  $t = 0$  and  $t = T$ . These can be removed by adding penalties to the fidelity used by GRAPE [67]. Only a small increase in gate time is usually needed to enforce pulse sequences to start and end at zero amplitude. The numerical results show that no speed limit is set by the overlap of the control field in the frequency domain with different qubit transitions. Additionally, numerical pulse sequences don't leave a phase error on the second qubit, eliminating the need for post-processing. The pulse sequence presented in fig. 4.1(a) is an illustration of an extremely fast control. It highlights the theoretical bounds of control speed in this system, however, its bandwidth is larger than the capabilities of typical arbitrary waveform generators. Optimising pulses with longer gate times in GRAPE results in controls with less spectral weight at high frequencies. This can be seen in fig. 4.2(a) which is much slower but has almost all its spectral power below 500 MHz.

Numerical pulses are designed by gradient ascent, thus optimal pulses enjoy the property  $\nabla_{kj}\Phi_{\text{QPT}} \simeq 0$ , i.e. the first derivative of the fidelity with respect to control  $k$  and pixel  $j$  of the optimal solution is small, ideally zero if the optimum is found [61, 115]. In practice, one still has to investigate the sensitivity against timing and amplitude errors. To study this we dilate the length of each pixel by an amount  $\eta$ , i.e.  $\Delta t \rightarrow \eta\Delta t$  and add white Gaussian noise to the amplitude of each pixel. The standard deviation of the noise is  $\sigma_{\text{noise}}$ . The fidelity, averaged over the different noise realisations is shown in Fig. 4.1(b). The region of high fidelity ( $\Phi_{\text{QPT}} > 99.9\%$ ) indicates that the pulse is somewhat robust against parameter uncertainty, in particular against slight errors in the pulse amplitudes. This is in particular important

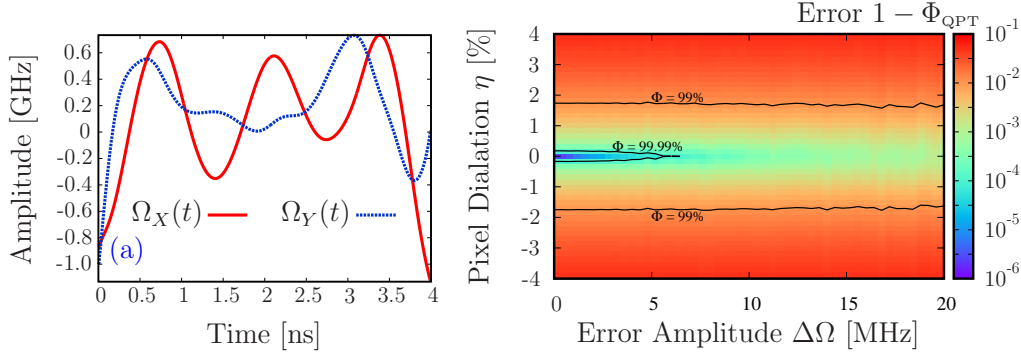


Figure 4.1: (a) Example of a numerically optimised pulse for gate time  $T = 4$  ns and  $\Delta t = 10$  ps. The pulses for shorter gate times are highly oscillating. The  $\Omega_Y$  control is usually not proportional to the derivative of  $\Omega_X$  highlighting at least a higher order of DRAG[38, 86]. (b) Study of the effect of errors on the pulse. The error amplitude  $\Delta\Omega$  is the standard deviation of the Gaussian distribution used to add noise to the pixels. The pixel time dilation error  $\eta$  is the percentage by which each pixel length is varied.

if the AWG implementing the pulse is digital.

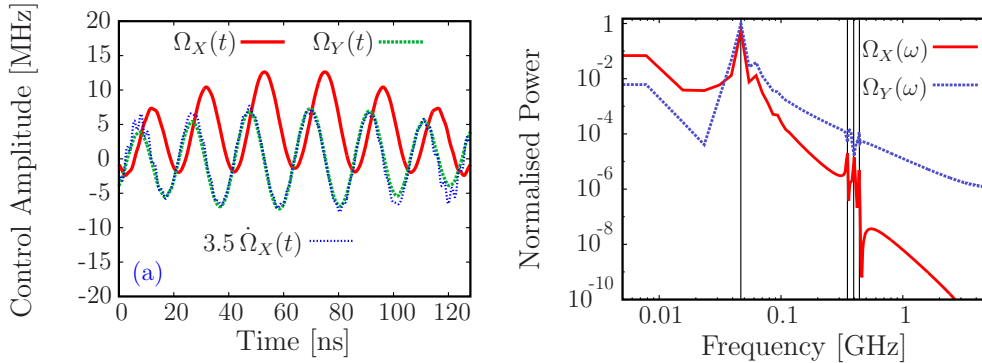


Figure 4.2: (a) Solution found by GRAPE for a long gate time, here  $\Delta t = 0.01$  ns and  $T = 130$  ns. The dotted line shows a rescaled version of the derivative of the  $\Omega_X$  control. (b) Fourier transform of the pulse shown in (a) found by GRAPE.

To get insight for the shape of the solutions we run the GRAPE algorithm for short time steps and longer gate times to increase the resolution of the discrete time Fourier transform (DTFT). These solutions show rapid oscillations, Fig. 4.2(a). The DTFT of the pulse sequence shows that both quadrature components have contributions at the energy splittings  $\delta$ ,  $\delta - \Delta$ ,  $\Delta$ ,  $2\delta - \Delta$ . This shows that the numerical solution augments the one based on the Magnus expansion by adding small further sideband drives. When going to shorter gate times Fourier analysis shows that the con-

tribution of the higher frequency components increases, making the Fourier transform less useful due to the lower frequency resolution. For faster pulses one could suggest that adding more sideband modulations could improve the results further.

## 4.2 Qubit-Resonator-Qubit Architecture

In many potential architectures for a quantum computer, the qubits are connected by strip-line resonators [116]. The strong coupling between qubit and resonator allows many Rabi oscillations before the quantum states decohere. In the following  $\hbar = 1$ . The system of interest is made of two qubits coupled to a bus resonator, the qubits are sufficiently far apart so that their direct coupling can be neglected. They are modelled by three level non-linear oscillators. The third level accounts for leakage and in the case of the CZ gate can be populated to perform the gate. The individual qubit Hamiltonians are

$$\hat{H}_{q_k} = \Delta_k |2\rangle_{kk}\langle 2| + \omega_k \hat{\sigma}_k^+ \hat{\sigma}_k^- ,$$

$\hat{\sigma}_k^+$  and  $\hat{\sigma}_k^-$  respectively create and destroy one excitation in qubit  $k$ ,  $\hat{\sigma}_k^\pm = \sum_n |n \pm 1\rangle_{kk}\langle n|$ .  $\omega_k$  is the  $0 \leftrightarrow 1$  transition frequency and  $\Delta_k$  is the anharmonicity. The bus, with transition frequency  $\omega_b$ , is harmonic and posses three levels:  $\hat{H}_b = \omega_b \hat{a}_b^\dagger \hat{a}_b$ . The dipolar coupling strength between the bus and qubit  $k$  satisfies  $g_k \ll \omega_k$  and therefore the rotating wave approximation holds. The system's total Hamiltonian in this approximation is

$$\hat{H} = \omega_b \hat{a}_b^\dagger \hat{a}_b + \sum_{k=1}^2 \left[ \Delta_k |2\rangle_{kk}\langle 2| + \omega_k \hat{\sigma}_k^+ \hat{\sigma}_k^- + \frac{g_k}{2} \left( \hat{\sigma}_k^+ \hat{a}_b + \hat{\sigma}_k^- \hat{a}_b^\dagger \right) \right] .$$

By the transformation  $\hat{H}^R = \hat{R}^\dagger \hat{H} \hat{R} - i \dot{\hat{R}}^\dagger \hat{R}$  where

$$\hat{R} = \left( \sum_{j=0}^2 \exp\{-ij\omega_b t\} |j\rangle\langle j| \right)^{\otimes 3} ,$$

we move to the rotating frame in which energies are measured with respect to the transition frequency of the bus. The Hamiltonian is

$$\hat{H}^R = \sum_{k=1}^2 \left[ \delta_k(t) \hat{n}_k + \Delta_k |2\rangle_{kk}\langle 2| + \frac{g_k}{2} \left( \hat{\sigma}_k^+ \hat{a}_b + \hat{\sigma}_k^- \hat{a}_b^\dagger \right) \right] \quad (4.1)$$

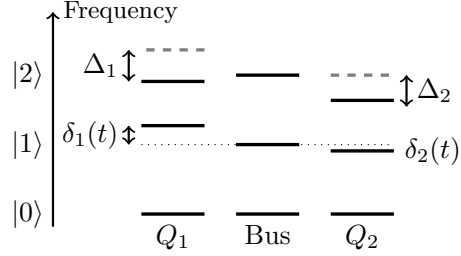


Figure 4.3: Sketch of the system where each element has three levels. The bus is harmonic and the qubits have anharmonicity  $\Delta_k$ .

where  $\hat{n}_k = \hat{\sigma}_k^+ \hat{\sigma}_k^-$  is the number operator for qubit  $k$ . The time dependence of the qubit-resonator detuning  $\delta_k(t) = \omega_k(t) - \omega_b$  is made explicit to indicate the controls. The energy levels are sketched in Fig. 4.3. The Hilbert space size is 27 dimensional and Hamiltonian (4.1) conserves the number of excitations. We make use of this to reduce the size of the Hilbert space since only computational states — states in which the qubits have at most one excitation — are of interest as well as the states that can be reached from these computational states. Therefore we only need to study the 10 states with at most 2 quanta. The model is valid for transmons [33] and phase qubits [25]. When dealing with the latter, the anharmonicity is a function of the qubit transition frequency and therefore a function of the controls  $\Delta_k = \Delta_k(\delta_k(t))$ . However for transmon qubits in the limit of large Josephson energy to charge energy it can be kept constant [33] to sufficient precision.

### 4.2.1 Analytic CZ Gate

In the Qubit-Bus-Qubit system, the entangling gate needed to form a universal set of gates, is the CZ defined by  $|ij\rangle \mapsto (-1)^{ij} |ij\rangle$ . It is realised with 2 iSWAPs and a conditional rotation through a  $|2\rangle$  state [114]. A sketch of the pulse sequence is shown in Fig. 4.4. The  $2\pi$  rotation through the  $|2\rangle$  state only takes place when both qubits are in the  $|1\rangle$  state and leaves a phase of  $\pi$  onto that state; this can entangle the qubits. This  $2\pi$  rotation is referred to as the Strauch gate [117]. This sequence is slow due to the shifting of states in and out of the resonator. An improved analytic pulse sequence based on few parameters has been found in Ref. *et al.* [110]. This work considers an alternate approach based on numerical methods.

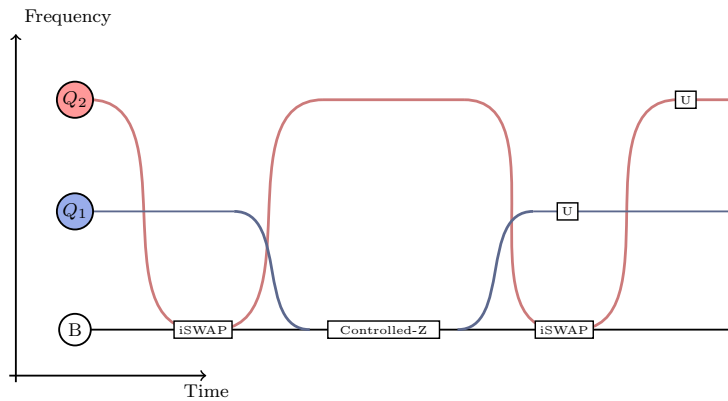


Figure 4.4: Sketch showing how the qubit's frequency is changed as function of time to create a CZ gate.

### 4.2.2 Limitations from Weak Anharmonicity

The fidelity of a Strauch gate is degraded by the presence of other levels in the system. To illustrate this we consider a simplified model compared to Hamiltonian (4.1); a three level anharmonic qubit coupled to a resonator

$$\hat{H}_{\text{QB}} = \underbrace{\omega_{\text{b}} (\hat{a}^\dagger \hat{a} + \hat{\sigma}^+ \hat{\sigma}^-)}_{\hat{H}_I} + \underbrace{\delta \hat{\sigma}^+ \hat{\sigma}^- + \Delta |2\rangle \langle 2| + \frac{g}{2} (\hat{\sigma}^+ \hat{a} + \hat{\sigma}^- \hat{a}^\dagger)}_{\hat{H}_{II}}$$

where  $\delta = \omega_{\text{q}} - \omega_{\text{b}}$ . This Hamiltonian conserves excitation number and thus is block diagonal with at most 3x3 blocks. For the block with  $n$  excitations  $\hat{H}_I$  is diagonal with identical values of  $n\omega_{\text{b}}$ . Focusing on  $n = 2$  the bare states are  $|2, 0\rangle$ ,  $|1, 1\rangle$  and  $|0, 2\rangle$ . The Hamiltonian is

$$\hat{H}^{(2)} = \begin{bmatrix} 2\omega_{\text{b}} + 2\delta + \Delta & \sqrt{2}g & 0 \\ \sqrt{2}g & 2\omega_{\text{b}} + \delta & \sqrt{2}g \\ 0 & \sqrt{2}g & 2\omega_{\text{b}} \end{bmatrix}. \quad (4.2)$$

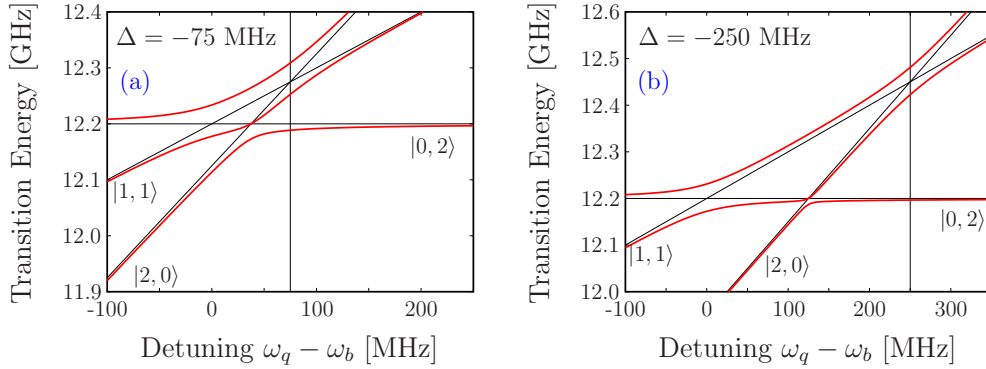


Figure 4.5: Energy of the dressed states in the three level Jaynes-Cummings model with  $\omega_{\text{b}} = 6.1$  GHz and  $T_{\text{swap}} = 12$  ns, i.e. the time it takes to swap a single excitation between the qubit and the bus. The three light black lines indicate the bare states whilst the vertical black line is  $-\Delta/2$ . (a) Dressed states with  $-75$  MHz anharmonicity and (b) dressed states with  $-250$  MHz anharmonicity.

Figure 4.5 shows the eigenvalues of  $\hat{H}^{(2)}$  for two different anharmonicities. The fine black lines represent energies of the uncoupled system, i.e. the bare states. A CZ gate is made by a  $2\pi$  rotation through the qubit's second excited state i.e.  $|1, 1\rangle \odot |2, 0\rangle$ . This is made possible by the anti-crossing indicated by the vertical black line in Fig. 4.5. This is when the qubit's  $|1\rangle \leftrightarrow |2\rangle$  transition is on resonance with the bus. The additional level  $|0, 2\rangle$  is an unwanted

state; any population entering it will decrease the gate's fidelity. Hamiltonian (4.2) shows that, the larger the anharmonicity is, the further away the  $|0, 2\rangle$  state is detuned. To clearly see its influence, the time evolved populations, shown in Fig. 4.6, are computed with  $\delta = -\Delta$  and for two different values of  $\Delta$ ; one small and one large. When  $\Delta$  is small, the Strauch gate performs badly as shown by Fig. 4.7. With  $-250$  MHz anharmonicity the leakage to  $|0, 2\rangle$  is at maximum 5%, this is still large. Figure 4.7 shows that the phase difference at the end of the  $2\pi$  rotation between the time evolved state looping from and to  $|1, 1\rangle$  and the reference  $\exp\{-i(2\omega_b - \Delta)t\}$  has a small deviation from  $\pi$ . The discrepancy is due to leakage to the  $|0, 2\rangle$  state. Such phenomena and multi-step swapping warrant a numerical approach to the problem of CZ gate design in the Qubit-Bus-Qubit architecture where the full Hamiltonian up to  $n = 2$  quanta is considered. Algorithms that maximise fidelity such as GRAPE and the quasi-Newton BFGS method [82] naturally suppress leakage which decreases fidelity [67] as defined.

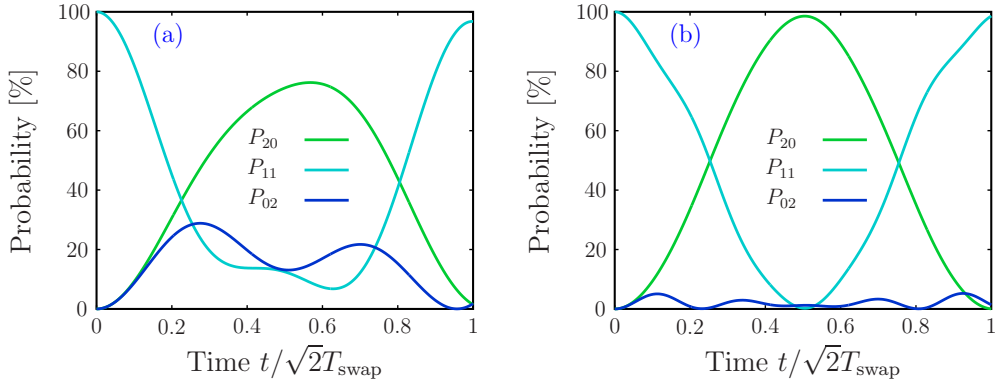


Figure 4.6: Time evolution of the populations computed using the spectrum of Fig. 4.5 at  $\delta = -\Delta$ . Time is normalised to the duration of a  $2\pi$  rotation through the qubit's  $|2\rangle$  state. If the anharmonicity is too small the effect of the second state of the bus will be large. This degrades the fidelity of the Strauch gate. (a) Population against time with  $-75$  MHz anharmonicity and (b) population against time with  $-250$  MHz anharmonicity.

### 4.3 Controlled-Z Gate Design by OCT

This section describes the GRAPE implementation to the problem at hand. We show how to deal with the effect of the electronics and how to include the non-linear behaviour of the anharmonicity arising when using phase qubits. We then apply gradient ascent to systems with different parameter values

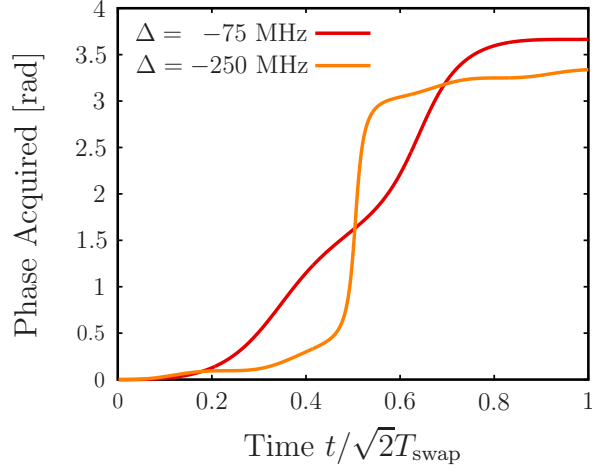


Figure 4.7: Phase difference between  $\langle 1, 1 | \exp\{-i\hat{H}t\} | 1, 1 \rangle$  and  $\exp\{-i(2\omega_b - \Delta)t\}$ . The discrepancy at the end of the gate is due to the presence of the unwanted  $|2\rangle$  state of the bus.

to illustrate key features of the system. We also benchmark the numerical pulses on a system corresponding to real qubits. Since only unitary evolution will be considered, the overlap between the target  $\hat{U}_t$  and achieved gate  $\hat{U}$ , defined in Eq. (2.6) serves as a fidelity function.

### 4.3.1 Including Electronic Transfer Functions

The arbitrary waveform generator (AWG) creating the control pulses has a limited bandwidth. Additionally the lines and remaining electronics between the AWG and qubits can distort the pulses. For this reason, the input control sent to the AWG will differ from the control applied by the qubits. In good approximation, this transfer is described by a linear causal transfer function [118]. When optimising the pulse shapes it must be ensured that the result is experimentally feasible. However the nature of the problem would require including numerical derivatives of measured transfer function data in the pulse optimisation. We avoid numerical derivatives by convoluting the pulses with a Gaussian to suppress high frequencies

$$\delta_{\text{qubit}}(t) = \int_{-\infty}^{\infty} \exp\left\{-\frac{(t-\tau)^2}{2\sigma^2}\right\} \delta(\tau) d\tau. \quad (4.3)$$

$\delta_{\text{qubit}}$  is the pulse shape that the qubit should see. The gradient is found with the chain rule [119]. The standard deviation  $\sigma$  should be chosen to reflect

the capabilities of the AWG. In an experimental implementation, it would be necessary to deconvolve the pulse in the qubit control software to take into account the true transfer function, which typically must be measured. If the bandwidth of the pulse given by the optimisation algorithm is small as guaranteed by our filtering procedure, then this deconvolution is easy and pulse shapes remain feasible.

### 4.3.2 Frequency Dependent Anharmonicity

When optimising pulses for a system where part of the Hamiltonian depends non-linearly on the controls the gradient rules of [52] must take the non-linearity into account. Such a situation can arise when optimising pulses for phase qubits where the anharmonicity depends non-linearly on the qubit frequency. Appendix A of [85] shows how to obtain the analytic formula of the gradient where the Hamiltonian depends linearly on the controls  $\hat{H}(t) = \hat{H}_d + \sum_k \delta_k(t) \hat{H}_k$ . Here is shown how to include non-linearities. We assume that in the Hamiltonian there are some parameters  $\Delta_l$  that depend non-linearly on the controls, i.e.  $\Delta_l = \Delta_l(\{\delta_k(t)\})$ . The total Hamiltonian at time  $j\Delta T$  becomes

$$\hat{H}(j\Delta T) = \hat{H}_d + \sum_k \delta_{kj} \hat{H}_k + \sum_l \Delta_l(\{\delta_{kj}\}) \hat{H}_{l,\text{nl}}. \quad (4.4)$$

The gradient of the time evolution operator  $\hat{U}_j$  of time-slice  $j$ , with respect to pixel  $\delta_{kj}$  of control  $k$ , is only sensitive to small variations around the value assumed by that pixel. Therefore we linearise the Hamiltonian at each iteration. If pixel  $kj$  assumes the value  $\delta_{kj}^{(n)}$  at iteration  $n$  the Hamiltonian can be approximated by  $\hat{H}(j\Delta T) \simeq \hat{H}'_d + \sum_k \delta_{kj} \hat{H}'_k$  where the drift and controls of this linearised Hamiltonian are

$$\hat{H}'_d = \hat{H}_d + \sum_l \Delta_l(\{\delta_{kj}^{(n)}\}) \hat{H}_{l,\text{nl}}, \quad (4.5)$$

$$\hat{H}'_k = \hat{H}_k + \sum_l \left. \frac{\partial \Delta_l(\{\delta_{kj}\})}{\partial \delta_{kj}} \right|_{\delta_{kj}^{(n)}} \hat{H}_{l,\text{nl}}. \quad (4.6)$$

This enables us to compute the gradient using the rules given in [52, 85]. At each iteration the control fields change and so do the linearised Hamiltonians  $\hat{H}'_d$  and  $\hat{H}'_k$ .

In the case of phase qubits, the dependency of the anharmonicity  $\Delta_k$  on the qubit frequency  $\delta_k$  can either be found numerically with a discrete variable representation [120] of the qubit's full potential or through measurement with high-power spectroscopy [69].

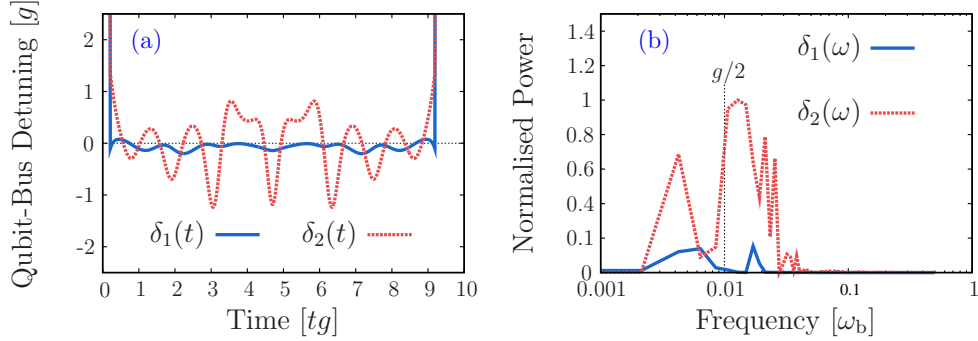


Figure 4.8: (a) Control pulses for a gate time slightly above  $T_{\text{QSL}}$ . (b) Discrete Fourier Transform of (a) showing that most of the spectral power is at small frequencies of order  $g$ .

### 4.3.3 Numerical Results

Here we assume that both qubits have the same anharmonicity  $\Delta_1 = \Delta_2 = \Delta = -0.1\omega_b$  and coupling  $g_1 = g_2 = g = 0.02\omega_b$ . Time will be indicated in dimensionless units of  $tg$  with  $g$  in radians  $s^{-1}$ . The desired gate fidelity is  $1 - 10^{-4}$ . At the start and end of the gate both qubits are far of resonance at their parking frequencies. This is included in the code by adding several buffer pixels, held at a constant detuning, before and after the gate.

The control pulses, found without Gaussian convolution, for a gate time of  $9 tg$  are shown in Fig. 4.8(a). Figure 4.8(b) shows the Discrete Fourier Transform (DFT) of these pulses: most of the oscillations in  $\delta_1(t)$  and  $\delta_2(t)$  have frequency components of the order of the qubit-bus coupling constant  $g/\sqrt{2}$ . This is because the CZ gate is made using  $|2\rangle$  states.

Figure 4.8 shows that the controls for qubit two oscillate at much larger amplitude than those for qubit one. We will later demonstrate that qubit 2 and the resonator populate their  $|2\rangle$  states similar to the Strauch gate in the pulse sequence. As the CZ gate is symmetric under the exchange of qubits, a control-target terminology to distinguish these qubits would be inappropriate. Instead, the qubit with smaller oscillations will be referred to as *Ginger* whereas the other will be called *Fred*. The next section explores what motivates the symmetry breaking apparent in these pulses

### Effect of Anharmonicity

As just stated, the CZ gate is symmetric under qubit exchange, however, the underlying Hamiltonian need not be. The main aspect breaking the symmetry is the anharmonicity of the qubit. This was studied with several different

combinations of qubit anharmonicities:  $\Delta_1, \Delta_2 \in \{-0.1, -0.2, -0.3\}$ . The allowed gate time was  $9 \text{ tg}$ . Because the Strauch method uses the  $|2\rangle$  state of the bus, the more linear qubit takes on the role of Fred since it is easier to drive the  $|1, 1\rangle \leftrightarrow |0, 2\rangle$  transition with the bus. The reason is: the greater the anharmonicity, the greater the qubit has to move away from the  $\delta = 0$  qubit-bus resonance, which is also crucial for  $|0, 1\rangle \leftrightarrow |1, 0\rangle$  exchanges. Figures 4.9(a) and 4.9(b) show two pulses for which  $(\Delta_1, \Delta_2) = (-0.3, -0.1)$  and  $(\Delta_1, \Delta_2) = (-0.1, -0.3)$  respectively. In both cases the search was nudged by means of asymmetric initial conditions, to choose qubit two as Fred. In the first case when the most linear qubit was chosen as Fred the target gate error of  $10^{-4}$  was reached. When the wrong qubit was assigned as Fred in the initial conditions, the code was not able to reach the target gate fidelity reaching only  $1 - \Phi_{\text{QPT}} \simeq 5.5 \cdot 10^{-3}$ . The choice as to which qubit assumes which role can either be enforced through asymmetric initial conditions or left up to GRAPE/BFGS with symmetric initial conditions. In the latter case the algorithm converges slower in the initial steps. The anharmonicity of Ginger does not play such an important role as Fred's. Figure 4.8 shows a pulse with  $(\Delta_1, \Delta_2) = (-0.1, -0.1)$ . The pulse of Fred is almost identical to the one in Fig. 4.9(a). However since Ginger is more linear than in Fig. 4.9(a) its control pulse has picked up some additional modulation which could be interpreted as to minimise leakage to the qubit  $|2\rangle$  state.

The populations associated to the pulse shown in Fig. 4.9(a) are displayed in Fig. 4.10; the  $|2\rangle$  state of the bus is highly used. Some of the excitation is

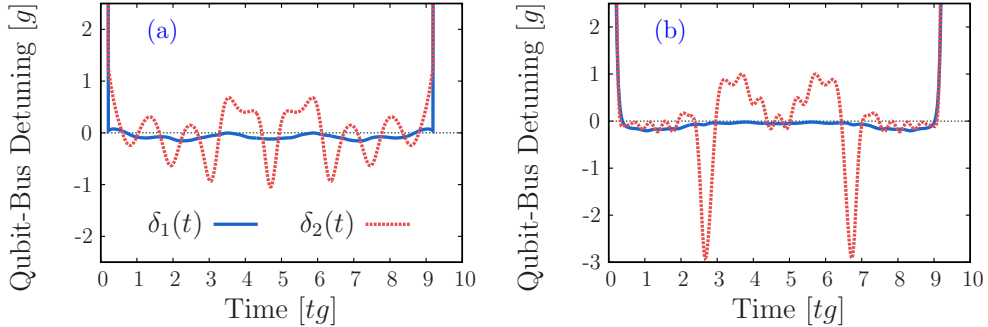


Figure 4.9: Comparison of the choice of Ginger and Fred. (a)  $(\Delta_1, \Delta_2) = (-0.3, -0.1)$ . Qubit 2, chosen as Fred, is the most linear. The optimisation was successful reaching  $\Phi_{\text{QPT}} = 99.99\%$ . (b)  $(\Delta_1, \Delta_2) = (-0.1, -0.3)$ . Qubit 2, chosen as Ginger, is the most linear. The optimisation was unsuccessful reaching only  $99.95\%$ . In both cases asymmetric initial conditions were used to force GRAPE to chose qubit 2 as Fred. Only the case shown in figure (a) resulted in good convergence.

transferred to the  $|2\rangle$  state of Fred but the  $|2\rangle$  state of Ginger remains empty, confirming our interpretation of the role of both qubits.

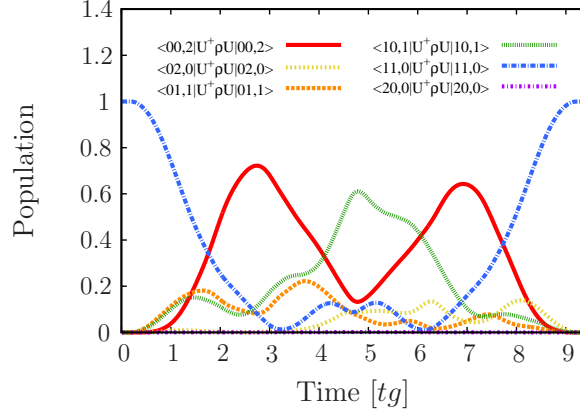


Figure 4.10: Populations assuming the input state is  $\rho_{in} = |11, 0\rangle\langle 11, 0|$  for the pulse of Fig. 4.9(a). It shows that the  $|2\rangle$  state of the bus is highly solicited to realise the CZ gate. However the  $|2\rangle$  state of the most non-linear qubit is not used at all.

However the pulses need not be asymmetric. If both qubits are identical and the initial conditions are symmetric, the resulting pulse sequence will be symmetric. Such a symmetric pulse is shown in Fig. 4.11.

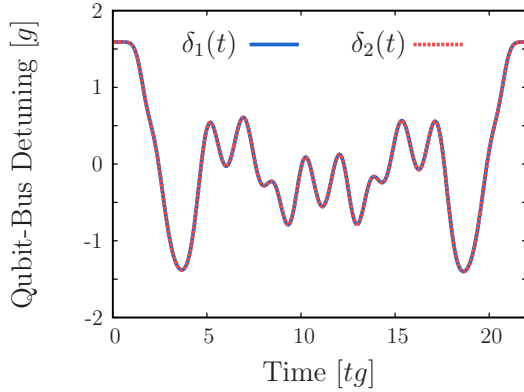


Figure 4.11: Control pulse with perfect fidelity (up to machine precision) for identical qubits and symmetric initial conditions. The control pulses producing the CZ gate are identical for both qubits showing that the two pulses need not be asymmetric. The qubit parameters were  $g_1/2\pi = g_2/2\pi = 50$  MHz and  $\Delta_1 = \Delta_2 = 60$  MHz.

### Influence of Impulse Response

As can be seen from Fig. 4.8(b) the DFT of the unfiltered pulse has almost all its power at low frequencies. This suggests that introducing a filter function in GRAPE should not significantly deteriorate the gate's performance. Therefore, in the control landscape, the optimal solutions with and without filter function should lie close together. The procedure is first to search for

a pulse without the filter function and then to rerun the optimisation with the filter function using the previously found pulse as the initial condition. The Gaussian impulse response has standard deviation of  $\sigma \cong 4 \omega_b^{-1}$ , chosen so that the 3 dB attenuation lies slightly above  $g = 0.02\omega_b$ . This function was then used to find a pulse sequence with the pulses shown in Fig. 4.8 as starting point. The output is shown in Fig. 4.12. As seen from the figures, the pulse found with the filter function is almost identical to the one found with a perfect impulse response. However the sharp corners have been smoothed out due to the high frequency filtering. This is encouraging since typical AWGs have a bandwidth of 500 MHz and most coupling strengths are in the range 20 – 70 MHz. Given the small effect of the impulse response, the subsequent optimisation will be done in one step using Gaussian convolution.

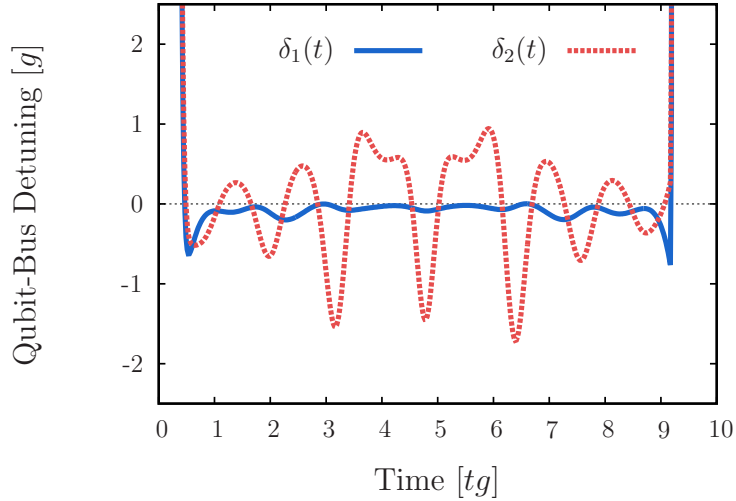


Figure 4.12: Effect of the filter function on the pulse sequence. The pulse from Fig. 4.8 was used as a starting point for the gradient ascent. Given that most of the spectral weight was initially at low frequencies, the Gaussian convolution has hardly any effect and the target fidelity of 99.99% is retrieved after only a few iterations.

#### 4.3.4 Benchmarking

To benchmark the performance of the numerical pulses against existing ones, the GRAPE method is applied to phase qubits in the RezQu architecture. The values<sup>1</sup> for the parameters in the Hamiltonian are shown in Tab. 4.1.

<sup>1</sup>The values for the parameters in the Hamiltonian correspond to a sample of the John Martinis group.

The non-linear behaviour of the qubit's anharmonicity was determined by high power spectroscopy [69]. The anharmonicities for this chip are very low and as indicated from section 4.2.2, would produce Strauch gates with extremely low fidelities.

Table 4.1: Parameters of the phase qubits. These values were used in the pulses presented in this document. The swap bus time  $T_{\text{swap}}$  is the time required to swap a quanta between the qubit and bus, i.e.  $|1, 0\rangle \rightarrow |0, 1\rangle$ . It is related to coupling strength by  $g_k = (2T_{\text{swap},k})^{-1}$ .

Element	Parameter	Value	unit
Bus	$\omega_b$ Frequency	6.1	GHz
Qubit 1	$\omega_1$ parking frequency	6.778	GHz
	$\Delta_1$ Anharmonicity	-71	MHz
	swap bus time	12.6	ns
Qubit 2	$g_1$ coupling strength	40	MHz
	$\omega_2$ parking frequency	6.607	GHz
	$\Delta_2$ Anharmonicity	-59	MHz
	swap bus time	9.2	ns
	$g_2$ coupling strength	54	MHz

In some situations the time it takes for a given state to evolve into an orthogonal state is bounded from below. This lower bound is the quantum speed limit (QSL) [121, 122]. This sets a minimum time  $T_{\text{QSL}}$  in which a gate can be done. When the gate time is above this speed limit, numerical pulses have perfect fidelity up to machine precision. This is shown in Fig. 4.13 where the gate time is progressively decreased. As long as  $T_{\text{Gate}} > T_{\text{QSL}}$  the pulse error is zero down to machine precision. For the system with values given by 4.1, the QSL is less than half of the time it takes the analytic pulse sequence of Fig. 4.4. We find  $T_{\text{QSL}} = 34$  ns. Below the quantum speed limit the fidelity degrades very rapidly. An error-free (up to machine precision) pulse is shown in Fig. 4.14(a). As seen in Fig. 4.14(b), a DFT shows that there is hardly any spectral power above 500 MHz thus making the pulse experimentally realistic. Fig. 4.15 shows the populations in the 2<sup>nd</sup> excitation subspace illustrating the increased complexity of these fast gates, defying, for now, a simple physical picture.

Note that in some cases, in particular for transmons that are operated through the resonator requiring a somewhat open resonator, one may desire an idle frequency that is more detuned from the resonator than assumed here. This would lead to slightly steeper initial and final slopes but does not change our conclusions.

Figure 4.13: Scan of the gate duration to find the quantum speed limit for phase qubits with the values of Tab. 4.1. The found quantum speed limit  $T_{\text{QSL}} = 34$  ns is twice as fast as the sequential pulse using the Strauch gate which takes  $T_{\text{Strauch}} = 76$  ns. Above the quantum speed limit, the numerical pulses are perfect up to machine precision.

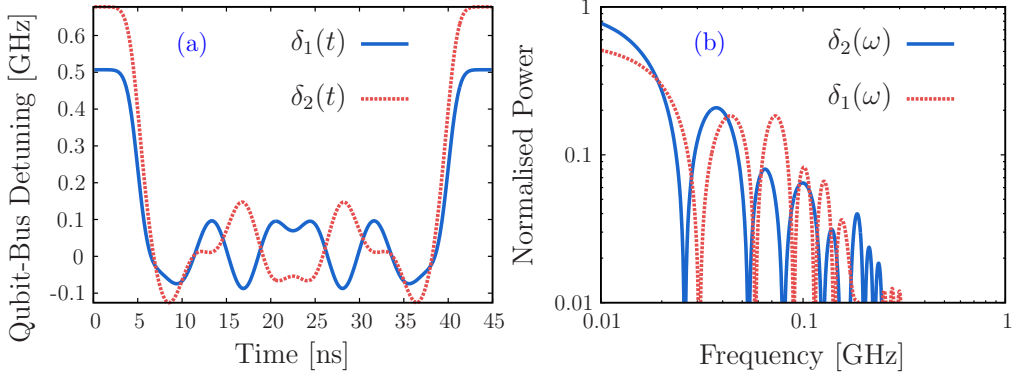
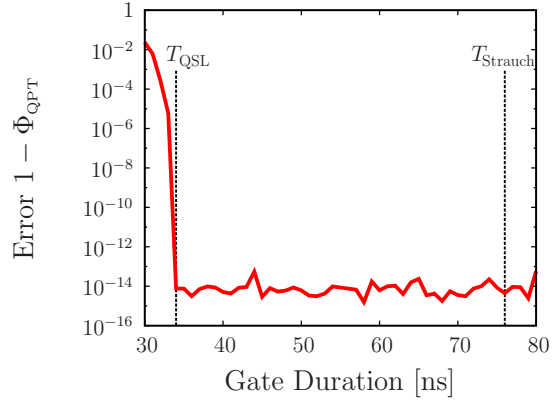


Figure 4.14: Summary of a numerical CZ gate design. Despite the low anharmonicities the pulses are able to reach very high fidelities. (a) Control pulse with  $1 - 10^{-14}$  intrinsic fidelity. The gate time is slightly above the quantum speed limit, i.e.  $T_{\text{Gate}} = 35$  ns. (b) Normalised spectrum of the ZPA corresponding to the GRAPE pulse shown in (a). Almost all the spectral power is within a few hundred MHz, thus the pulse is experimentally feasible.

## 4.4 CZ Error Sources and Mitigation Strategies

The previous section showed that CZ gates with arbitrary intrinsic fidelities can be generated even for low anharmonicity qubits. However, in experimental conditions these high quality pulses are rapidly degraded by various errors. The following section reviews them and discusses how to overcome them.

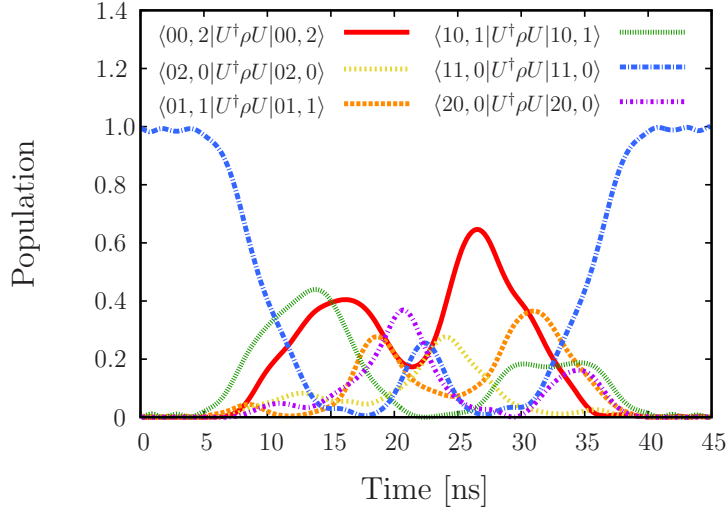


Figure 4.15: Populations of the two excitation sub-space associated to the GRAPE pulse shown in Fig. 4.14(a). As can be seen, an analytical picture similar to that shown in section 4.2.1 is no longer possible.

#### 4.4.1 Intrinsic Pulse Robustness

Gradient ascent engineered pulses enjoy an almost null first derivative with respect to the individual control pixels. Thus to first order, random fluctuations of the pulse amplitude do not severely impact the fidelity. This was checked by perturbing the controls with white Gaussian noise with a standard deviation given by  $\sigma_E = \Delta\delta_{k_j}/\delta_{k_j}$ . Figure 4.16 shows that a 1% relative variation of the control field amplitude decreases a 99.99% intrinsic fidelity pulse to 99.95%. Therefore random fluctuations in pulse amplitude are of little consequence on these pulses [61, 115].

#### 4.4.2 Systematic Errors

Some systematic errors will effect the pulses in a more significant way than the random fluctuations of pulse amplitude. There are three main errors that have been identified: calibration errors, timing errors and parameter errors. All are described below.

##### Calibration Errors: Control Pulse Amplitude to Qubit Frequency

Although we optimise the qubit frequency in our numerics, the true control is the amplitude of the Z pulse (ZPA), a voltage pulse applied to the qubit. The ZPA is related to the frequency of the qubit through a calibration curve.

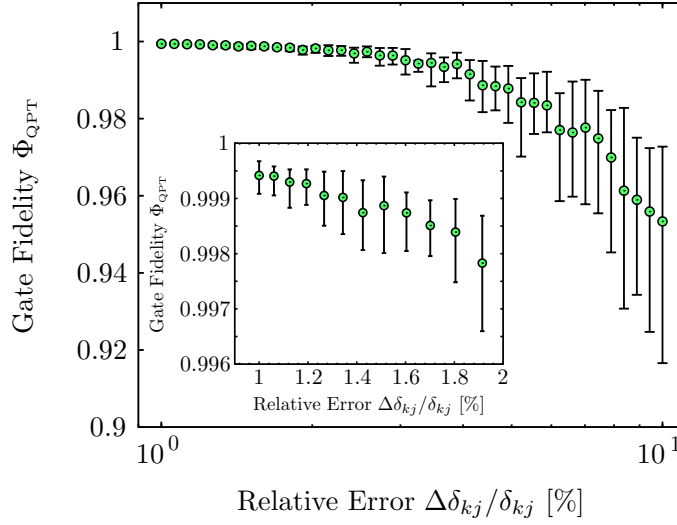


Figure 4.16: Error introduced by randomly changing the amplitude of the controls. The relative error is expressed in  $\Delta\delta_{kj}/\delta_{kj}$ . The system considered was the Qubit-Bus-Qubit with constant anharmonicity.

This curve must be measured using spectroscopy and errors in it will cause errors in qubit frequency, see Fig. 4.17(a) for a sketch. The bus frequency does not enter the Hamiltonian (4.1). However it must be known so as to give the qubits the right ZPA to put them on resonance with the bus. A constant and systematic shift of the pulse with respect to the resonance point produces phase and leakage errors. The situation is sketched in Fig. 4.17(b) where qubit 1 undershoots the bus by an amount  $\Delta\omega_{b,1}$  and qubit 2 overshoots the bus by  $\Delta\omega_{b,2}$ .

Off resonance from the bus, calibration errors have little effect since qubit and resonator cannot exchange quanta. Therefore this error is modelled by a systematic shift in the qubit frequency changing the resonance point with the bus

$$\delta_k(t) \mapsto \delta_k(t) + \Delta\omega_{b,k}.$$

This shift also displaces the qubit parking frequency, which, in experiment, is typically held constant at all times [123]. This discrepancy between experiment and model is acceptable due to the lack of exchange of quanta far of resonance. The Hamiltonian with error terms is

$$\hat{H}^R = \underbrace{\sum_{k=1}^2 \delta_k(t) \hat{n}_k}_{\text{Controls}} + \underbrace{\sum_{k=1}^2 \left[ \Delta\omega_{b,k} \hat{n}_k + \Delta_k \hat{\Pi}_{2,k} + \frac{g_k}{2} \left( \hat{\sigma}_k^+ \hat{a}_b + \hat{\sigma}_k^- \hat{a}_b^\dagger \right) \right]}_{\text{Drift with errors}}.$$

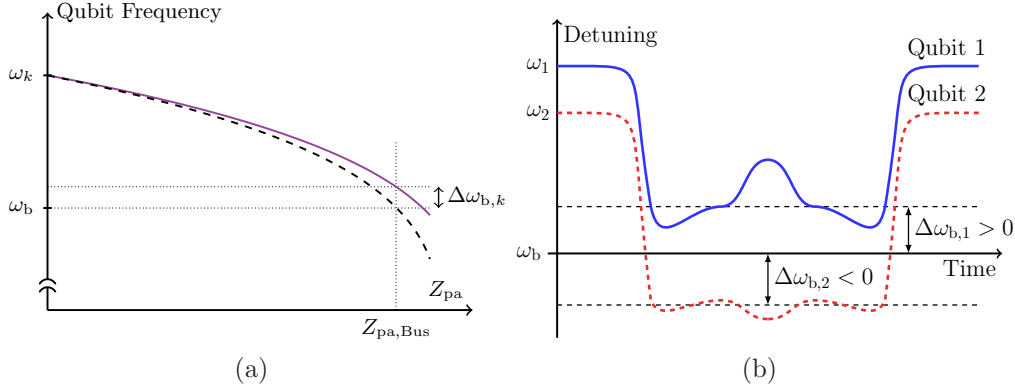


Figure 4.17: Calibration errors result in a DC offset of the pulse. The “true” calibration curve – dashed line – is approximated by the solid line which is the measured calibration curve. This discrepancy causes the qubit-bus resonance to be missed by  $\Delta\omega_{b,k}$ . (b) DC offset in the pulse amplitudes. The qubit parking frequency  $\omega_{Q_k}$  is left unchanged. However, the resonance point is missed; the pulses perform their oscillations around  $\omega_b + \Delta\omega_{b,k}$  instead of  $\omega_b$ .

The effect of the calibration error on the Fidelity (2.6) is shown in Fig. 4.18(a). A pulse was first optimised with  $(\Delta\omega_{b,1}, \Delta\omega_{b,2}) = (0, 0)$  and then the fidelity is recomputed for different values of the error. The central high fidelity region is very small; although the first derivative  $\partial\Phi/\partial\Delta\omega_{b,k}$  is close to zero near the optimum the second derivative is very strong. This shows how small errors ruin the pulse.

If a single control amplitude at a given time is viewed as a degree of freedom, pulse optimisation is a highly under-constrained non-linear problem given the limited number of independent parameters in the target gate. Robust control exploits the surplus of degrees of freedom to make a pulse sequence robust over a larger parameter range [124]. However in this case such methods fail since the error is on the control Hamiltonians and not the drift. To remove the calibration error a different approach must be used.

We propose to manually introduce a controllable DC offset in the pulse. The effect of this offset on various quantities can be determined both in simulations and experiment. Comparing the two gives the optimal DC offset needed to compensate the error. In simulation, we compute the time evolution operator which lets us know how big leakage and phase errors are. In an experiment, leakage can be measured by qubit population and phases are accessible with Ramsey measurements.

We illustrate this first with qubit population by scanning  $(\Delta\omega_{b,1}, \Delta\omega_{b,2})$  and computing the population of qubit one after the gate. Figure 4.18(b) shows the magnitude of  $[\hat{U}]_{10,10}$ . It is the entry of the time evolution operator

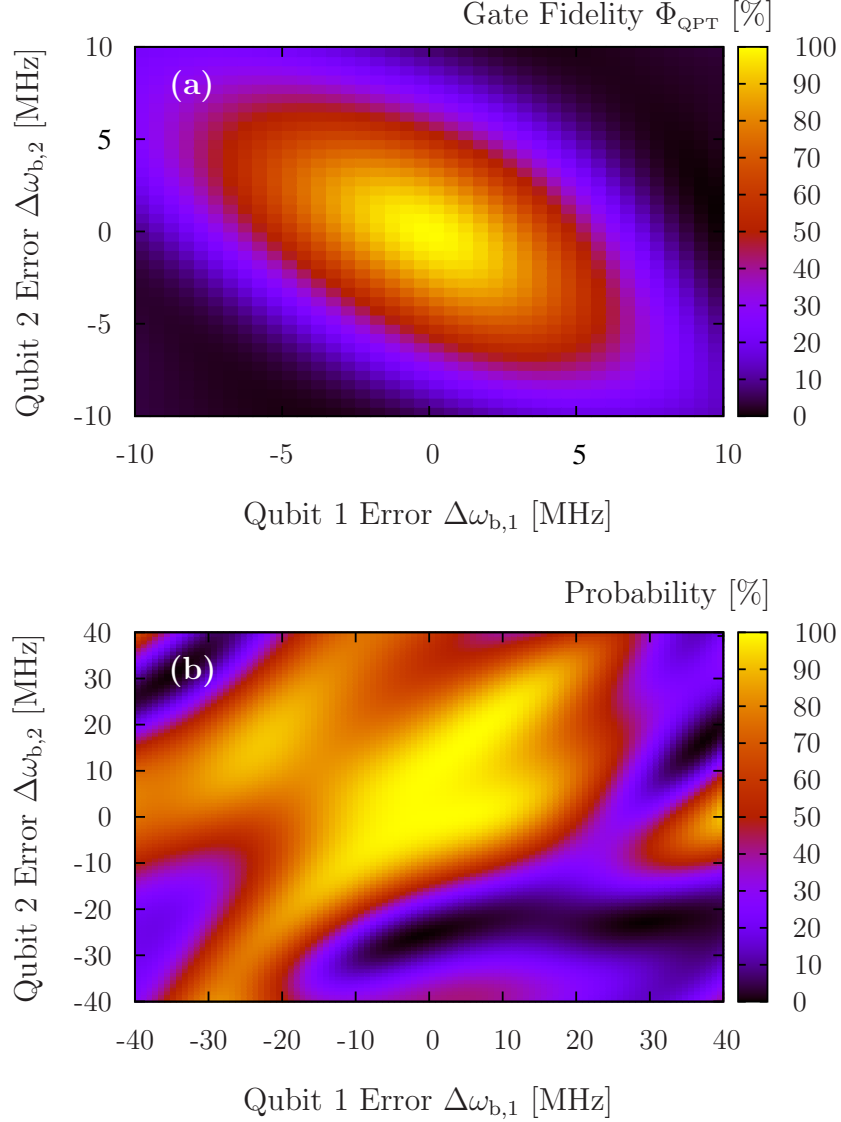


Figure 4.18: (a) Loss of fidelity due to over and undershoot of the bus-qubit resonance frequency arising from systematic calibration errors. As can be seen errors on the bus frequency of less than 0.1% ruin the pulses. (b) Scan of  $|U_{10,10}|^2$  as function of the calibration error. Away from the resonance point  $(\Delta\omega_{b,1}, \Delta\omega_{b,2}) = (0, 0)$  leakage starts to manifest itself as a decrease in  $|U_{10,10}|^2$ . The many features in the plot allow for a good correction of the error.

quantifying population transfer from state  $|10,0\rangle$  to itself. For an ideal CZ  $|\langle \hat{U} \rangle_{10,10}|^2 = 1$ , however when changing the DC offset this value decreases. The strong effect of the error is thus used to our advantage since the many features in the  $(\Delta\omega_{b,1}, \Delta\omega_{b,2})$  error landscape allow an easy comparison between experiment and simulation. Similar data could be obtained with an experiment, comparing it to the simulation would give the DC offset needed to correct the errors.

### Timing Errors

Another error source is the relative timing between the two pulses. This arises if the wires taking pulse one from the AWG to qubit one differ in length from those to qubit two. Pulses offset in time by  $\Delta\tau$ , as sketched in Fig. 4.19(a), lose their fidelity as shown by Fig. 4.19(b). This error can be removed by introducing a time shift between the pulses and scanning the time shift until leakage/fidelity is minimised/optimised. As seen from Fig. 4.19(b) the relative timing between the pulses should be accurate to within  $\approx 100$  ps.

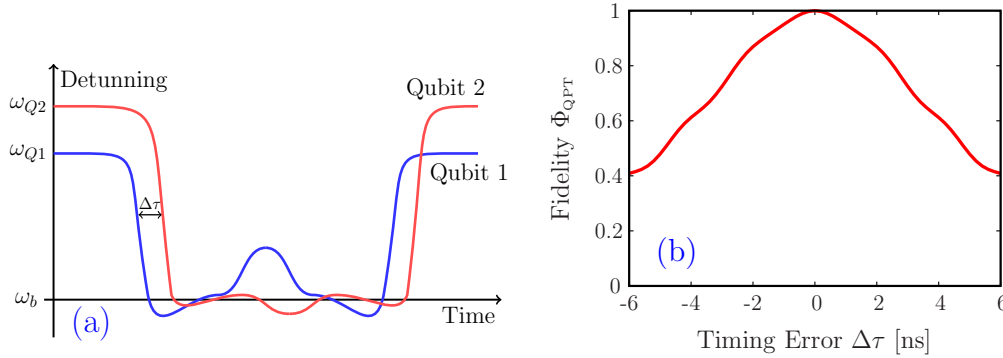


Figure 4.19: Relative timing errors. (a) Sketch of pulse relative timing errors. Both pulses have the intended shape but are offset in time by an amount  $\Delta\tau$ . (b) Degradation of the fidelity as function of the timing error.

### Hamiltonian Parameter Errors

Gradient ascent engineered pulses rely on knowing the Hamiltonian to optimise the pulse. However the parameters entering the model need to be measured and thus come with some amount of uncertainty and error. The pulses designed with these parameters will perform sub-optimally. In the Qubit-Bus-Qubit system, there are four parameters that are susceptible to

these error:  $\{\Delta_1, \Delta_2, g_1, g_2\}$ . For instance, Fig. 4.20 shows fidelity degradation as function of errors on the coupling strength and anharmonicity of qubit 1. The pulse was optimised to have a target error of  $10^{-5}$ . If a pulse fidelity of 99.9% is sufficient, the intrinsic pulse robustness, i.e.  $\partial\Phi/\partial g_k \approx 0$  and  $\partial\Phi/\partial\Delta_k \approx 0$  allows us to tolerate an error of up to 1.5% in coupling strength and 1.2% in anharmonicity.

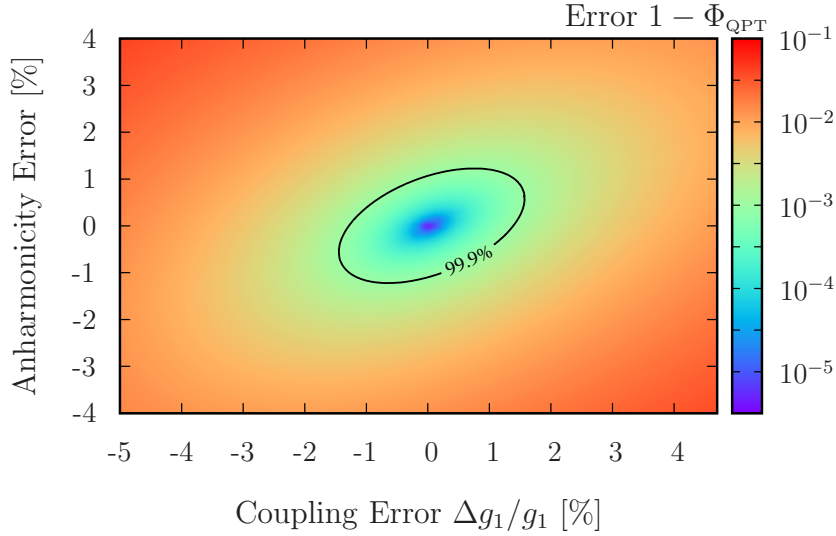


Figure 4.20: Degradation in fidelity due to errors in the parameters of the Hamiltonian. The anharmonicity error is  $\Delta(\Delta_1)/\Delta_i$ . The pulse was optimised with a target error of  $10^{-5}$ . If a fidelity of 99.9% is sufficient, the intrinsic robustness of the pulse can support errors of up to 1.5% in coupling strength and 1.2% in anharmonicity.

## 4.5 Conclusions

Numerically optimised Wah-Wah pulses show that qubits can still be addressed individually with short gate times. Faster control pulses require more bandwidth and amplitude, therefore the limiting factor is the capabilities of the arbitrary waveform generator. No speed limit has been observed in numerically optimised pulses for two 3D transmons, which is contrary to the believe that spectral crowding limits the scalability of the 3D cavity architecture in cQED.

We develop fast pulses implementing an entangling gate, the CZ, between two qutrits through a bus. These demonstrate a factor 2 speed up in CZ gates as well as the possibility to reach arbitrary intrinsic gate fidelity as long as

the gate time is above the quantum speed limit. It turns out that the optimal pulses break the symmetry of the target gate and make active use of non-computational excited states. We have also shown how errors arising from realistic experimental conditions can be negated.

The controls we found typically lead to occupation of the resonator during gate operation. This may be a disadvantage if there is strong Purcell decay from the cavity as necessitated in architectures where control and/or readout are done through the cavity [20, 23, 116]. However it is not a limitation in situations when control and readout are done directly on the qubits and the main decoherence sources are connected to the qubits themselves [114, 123]. In the former case, one would like to keep the qubits far detuned from the cavity and use a dispersive gate [103]. The precise crossover between these regimes and optimality under decay are topics for future research. Further work in cavity-mediated gates [103, 110] discusses a variety of strategies found by hand, smooth few-parameter pulses that all take longer time and are less adapted to imperfections of the system and thus may be a stepping stone towards optimised gates.



# Chapter 5

## Non-Unitary Targets

The previous chapters focused on creating high fidelity gates for quantum computing. This is only one of the ingredients needed to make a quantum computer. Another is measurement, the qubit states need to be determined with high fidelity. The read out mechanism depends on the type of superconducting qubits being used. For instance transmon qubits are typically read out through a resonator [33, 125] whilst phase qubit readout is based on tunnelling out of a metastable well [126, 127]. This tunnelling mechanism can also be used to create a microwave photon counter named the Josephson photomultiplier (JPM) [128]. These phase qubit detectors rely on a measurement pulse that causes a state dependent tunnelling event. Here will be shown how to optimise this pulse with optimal control. The target time evolution cannot be described by a unitary matrix since it is irreversible and relies on incoherent processes. However, In most optimal control experiments the target time evolution is a unitary operator. A few examples of this include quantum gates for quantum computing, the evolution of many electron systems under Hamiltonian dynamics [129] as well as evolution under a non-linear Schrödinger equation [130]. Optimisation towards a unitary gate can also be done in the presence of non-unitary dynamics [83, 131]. Thus, in this chapter we expand the GRAPE algorithm to the case where the target is a non-unitary quantum channel. This allows us to optimise measurement pulses for phase qubits and JPMs.

### 5.1 Optimal Control Algorithm

An open quantum system with Markovian dynamics follows the time evolution given by a Lindblad master equation, see Eq. (2.3). The time evolved

---

In preparation D. J. Egger & F. K. Wilhelm

density matrix can be found by vectorising the master equation. Vectorisation is done by applying the identity  $\text{col}(ABC) = (C^T \otimes A)\text{col}(B)$  to Eq. (2.3). Here  $\text{col}(X) = \vec{X}$  denotes column stacking of the matrix  $X$ . The result is a first order differential equation for the vectorised density matrix  $\vec{\rho}$

$$\dot{\vec{\rho}} = \mathcal{S} \vec{\rho}.$$

This equation is similar to the Schrödinger equation and can be solved by exponentiating the generator  $\mathcal{S}$ . The time evolution is thus given by the Liouville superoperator  $\mathcal{T}$  defined in Eq. (2.4). For a column stacked vectorised master equation the generator is

$$\mathcal{S}(t) = i \left( \hat{H}^T \otimes \mathbb{1} - \mathbb{1} \otimes \hat{H} \right) + \sum_l \gamma_l \left( \hat{L}_l^* \otimes \hat{L}_l - \frac{1}{2} \hat{L}_l^T \hat{L}_l^* \otimes \mathbb{1} - \frac{1}{2} \mathbb{1} \otimes \hat{L}_l^\dagger \hat{L}_l \right) \quad (5.1)$$

where  $\hat{H}$  is the Hamiltonian and  $\hat{L}_l$  is the Lindblad operator associated to the incoherent process with rate  $\gamma_l$ . Within this generator are hidden the control fields  $\mathbf{u}(t)$ . They can be located in the Hamiltonian  $\hat{H}$  which, as in the GRAPE algorithm [52], is separated into drift  $\hat{H}_d$  and controls  $\hat{H}_k$ . However they can also control some of the rates such that the set of rates can be split into controllable rates and drift rates  $\{\gamma_l\} = \{\gamma_{l,d}, \gamma_{l,c}(\mathbf{u}(t))\}$ . This suggests a drift-control decomposition for the generator

$$\mathcal{S}(t) = \mathcal{S}_d + \sum_k f_k(\mathbf{u}(t)) \mathcal{S}_k.$$

The drift term  $\mathcal{S}_d$  is the part of Eq. (5.1) containing the drift Hamiltonian  $\hat{H}_d$  and the Lindblad operators corresponding to the drift rates  $\gamma_{l,d}$ . The control part is the remaining part of Eq. (5.1). It contains terms dependent on  $\mathbf{u}(t)$ . The functions  $f_k$  account for possible non linear behaviours with respect to  $\mathbf{u}(t)$ . However, these functions  $f_k$  are known and assumed to be differentiable allowing us to use the chain rule when computing gradients with respect to the controls.

Similarly to the GRAPE algorithm described in section 2.3 the controls are pixelised and the Liouville superoperator  $\mathcal{T}(T)$  is approximated by

$$\mathcal{T}(T) = \prod_{j=N-1}^0 e^{\mathcal{S}(j\Delta T)\Delta T}$$

where  $\mathcal{S}(j\Delta T)$  is the generator evaluated at pixels  $\mathbf{u}(j\Delta T)$ . This time evolution corresponds to a quantum channel which we wish to optimise. To

do so a fidelity measure based on Choi matrices is constructed. The Choi matrix, defined in section 2.1, is related to the Liouville supermatrix  $\mathcal{T}$  by reorganising the elements according to

$$C_{d\alpha+\beta, d\alpha'+\beta'} = \mathcal{T}_{d\beta'+\beta, d\alpha'+\alpha}, \quad (5.2)$$

where  $d$  is the dimension of the Hilbert space and  $\alpha, \alpha', \beta, \beta' \in \{1, \dots, d\}$ . This is shown by noticing that the vectorised matrix  $|i\rangle\langle j|$  is the unit vector  $\hat{e}_{dj+i}$  with 1 on entry  $dj+i$  and zero elsewhere. Therefore with  $[\mathcal{E}(|i\rangle\langle j|)]_{\beta, \beta'} = \mathcal{T}_{d\beta'+\beta, dj+i}$  and Eq. (2.5) which defines the Choi matrix, the above identity ensues. A natural way to measure how close the realised quantum channel is to a target channel, described by a Choi matrix  $C_t$ , is through the channel fidelity [132]

$$\Phi_{\text{ch}} = \frac{1}{d^2} \left( \text{Tr} \left\{ \sqrt{\sqrt{C_t} C[\mathbf{u}] \sqrt{C_t}} \right\} \right)^2.$$

This fidelity is very similar to the fidelity between two states  $\rho$  and  $\sigma$  given by  $\mathcal{F} = \text{Tr} \sqrt{\sqrt{\rho} \sigma \sqrt{\rho}}$  [1]. This comes as no surprise since the Choi matrices are, up to their trace, equivalent to density operators. The channel fidelity  $\Phi_{\text{ch}}$  has the pleasing property that, when both channels are unitary, it equals the gate overlap fidelity  $\Phi_{\text{QPT}}$  defined in Eq. (2.6). However it is not suitable for a pulse optimisation algorithm due to the square root which prevents an analytical expression for the gradient. Instead we define a fidelity starting from the square of the Frobenius norm

$$\|C_t - C[\mathbf{u}]\|^2 = \text{Tr} \{C_t^2\} + \text{Tr} \{C[\mathbf{u}]^2\} - 2 \text{Re} \text{Tr} \{C_t^\dagger C[\mathbf{u}]\}.$$

The equality follows from the definition of the Frobenius norm. As the realised channel approaches the target one, the error  $\|C_t - C[\mathbf{u}]\|^2$  is reduced. This prompts the following definition for the fidelity

$$\Phi'_{\text{ch}} = \text{Re} \text{Tr} \{C_t^\dagger C[\mathbf{u}]\}. \quad (5.3)$$

Its gradient with respect to the control pixels is

$$\nabla_{kj} \Phi'_{\text{ch}} = \text{Re} \text{Tr} \left\{ C_t^\dagger \frac{\partial C[\mathbf{u}]}{\partial u_{kj}} \right\}. \quad (5.4)$$

The gradient of the Choi matrix is found by computing the gradient of the Liouville superoperator and rearranging the terms according to Eq. (5.2). The procedure to compute the gradient of  $\mathcal{T}$  follows the same idea as for the

unitary case presented in section 2.3. However, since in a generic open system  $\mathcal{S}$  is not necessarily normal [85], the procedure of computing the gradient of a single pixel using eigenvalues does not work. Instead the identity

$$\left. \frac{d}{dx} e^{A+xB} \right|_{x=0} = e^A \int_0^1 e^{-A\tau} B e^{A\tau} d\tau \quad (5.5)$$

is used. The latter can be evaluated exactly using augmented matrix exponentials [83]

$$\exp \begin{pmatrix} A & B \\ 0 & A \end{pmatrix} = \begin{pmatrix} e^A & \int_0^1 e^{A(1-\tau)} B e^{A\tau} d\tau \\ 0 & e^A \end{pmatrix}. \quad (5.6)$$

Thus for computing  $\partial\mathcal{T}/\partial u_{kj}$  one sets  $A = \mathcal{S}(j\Delta T)\Delta T$  and  $B = \mathcal{S}_k\Delta T$ . Given that the augmented matrix can be defective, its exponential is computed with Ward's Padé approximation [133, 134]. Finally all elements are in place to successfully optimise the pulse of a non-unitary process towards a target non-unitary channel using the GRAPE and BFGS algorithms described in section 2.4. The fidelity is given by Eq. (5.3) whilst its gradient is found from Eqs. (5.4) through (5.6).

## 5.2 Optimisation of a Phase Qubit Measurement Pulse

The flux biased phase qubit is a superconducting circuit made of a large area Josephson junction shunted by an inductor. Threading an external flux through this loop makes the energy levels tunable and also allows for easy readout [126, 127]. Josephson photomultipliers allow single photon detection in the microwave regime and are also based on a phase qubit like architecture [128, 135]. Here we will show how to optimise a measurement pulse for a phase qubit using the methods described in the previous section. The phase qubit [136, 137], flux biased by  $\varphi_b$  but without current bias, is described by the Hamiltonian

$$\hat{H} = E_c \hat{N}^2 + E_J \left( \frac{1}{2\beta} (\hat{\varphi} - \varphi_b)^2 - \cos \hat{\varphi} \right). \quad (5.7)$$

The charging energy is  $E_c = 2e^2/C$  and the Josephson coupling energy is  $E_J = I_0\hbar/2e$ . The qubit is coupled to the external bias flux  $\Phi_0\varphi_b$  by the constant  $\beta = 2eLI_0/\hbar$ . The critical current of the JJ is  $I_0$  and its associated capacitance is  $C$  whilst the shunt inductance is  $L$ . When biased a little below

## 5.2. OPTIMISATION OF A PHASE QUBIT MEASUREMENT PULSE 71

$\varphi_b = 2\pi$  the potential is an asymmetric double well with a shallow and a deep well. The qubit states  $|0\rangle$  and  $|1\rangle$  are formed out of the two lowest states of the shallow well. By raising the bias closer to  $2\pi$ , the shallow well becomes shallower allowing the  $|1\rangle$  and  $|0\rangle$  state to tunnel into the deeper well. The tunnelling rate  $\gamma_1$  of  $|1\rangle$  is typically much higher than that of  $|0\rangle$  i.e.  $\gamma_0$ . This rate difference allows the measurement to discriminate between  $|0\rangle$  and  $|1\rangle$ . The flux change resulting from a tunnelling event is picked up by a SQUID and is interpreted as the qubit being in the  $|1\rangle$  state [136]. This prompts a three state description of the qubit formed by the basis  $\{|0\rangle, |1\rangle, |m\rangle\}$ .  $|m\rangle$  is a combination of all the states that  $|0\rangle$  and  $|1\rangle$  can incoherently tunnel into. These incoherent rates depend on  $\varphi_b$  and will be described later.

The control problem is to optimise a measurement pulse  $\varphi_b(t)$  of duration  $T_{\text{meas}}$  that maximises the contrast

$$\xi = \langle m | \hat{\rho}_1(T_{\text{meas}}) | m \rangle - \langle m | \hat{\rho}_0(T_{\text{meas}}) | m \rangle .$$

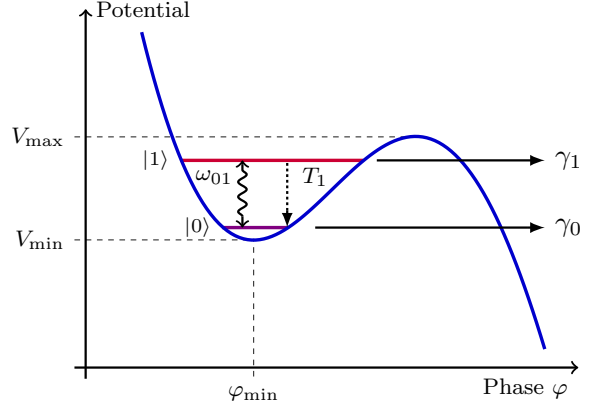
$\hat{\rho}_i$  is the time evolved density matrix corresponding to the initial state  $|i\rangle\langle i|$ . This target can be shaped into a Choi matrix given by

$$C_t = |1\rangle\langle 1| \otimes |m\rangle\langle m| + \sum_{i,j \in \{0,m\}} |i\rangle\langle j| \otimes |i\rangle\langle j| .$$

Since the tunnelling is incoherent the coherences between  $|1\rangle$  and  $|m\rangle$  are not preserved as the ideal quantum channel maps  $|1\rangle\langle 1|$  to  $|m\rangle\langle m|$ . This gives the first part of  $C_t$ . The second states that the elements  $|0\rangle\langle 0|$ ,  $|m\rangle\langle 0|$ ,  $|0\rangle\langle m|$  and  $|m\rangle\langle m|$  should be left untouched.

Before and after the measurement pulse, the qubit is at a reference bias  $\varphi_{\text{ref}}$  chosen such that tunnelling out of  $|1\rangle$  is suppressed. Indeed it is expected that coherent operations are done between  $|0\rangle$  and  $|1\rangle$  before the measurement pulse. Therefore the states should not tunnel out of the shallow well. However the shape of the wavefunctions  $\psi_i(\varphi, \varphi_b) = \langle \varphi | i \rangle$  for  $i = 0, 1$  change with bias flux. Thus changing  $\varphi_b$  can induce  $|0\rangle \leftrightarrow |1\rangle$  transitions through Landau-Zener type physics. This creates dark counts. To avoid such effects an adiabatic pulse should be used since slow changes in the potential will keep the system in  $|0\rangle$  if it started in  $|0\rangle$ . However,  $|1\rangle \rightarrow |0\rangle$  relaxation, graphically illustrated in Fig. 5.1, causes missed counts. This degradation in contrast can be mitigated by using a fast pulse. This interplay between Landau-Zener like behaviour and energy relaxation prompts the use of optimal control theory to shape the measurement pulse. The optimal pulse should reduce dark and missed counts. The former are reduced by the optimal shape whilst that latter are mitigated by forcing  $|1\rangle$  to tunnel before relaxation happens.

Figure 5.1: Sketch of the phase qubit's potential focusing on the shallow well. The wavy line indicates the  $0 \leftrightarrow 1$  transition frequency which is a coherent process and enters in the Hamiltonian. Controllable incoherent processes are indicated by solid straight lines whereas the uncontrollable  $T_1$  relaxation process is constant.



### 5.2.1 Phase Qubit Model

For an arbitrary bias flux the three level model Hamiltonian is expressed with respect to a reference bias  $\varphi_{\text{ref}}$  by

$$\hat{H} = P\hat{H}_{\text{ref}}P^{-1} \quad \text{with} \quad P = \begin{pmatrix} \eta & \sqrt{1-\eta^2} & 0 \\ \sqrt{1-\eta^2} & -\eta & 0 \\ 0 & 0 & 1 \end{pmatrix}. \quad (5.8)$$

$\hat{H}_{\text{ref}} = \omega_{\text{ref}}|1\rangle\langle 1|$  is the Hamiltonian at the reference bias where  $\omega_{\text{ref}}$  is the corresponding  $0 \leftrightarrow 1$  transition frequency. The unitary matrix  $P$  results from the Landau-Zener physics arising between  $|0\rangle$  and  $|1\rangle$  when changing the bias flux. Its single parameter  $\eta$  is the overlap between the logical zero state and itself at different bias values

$$\eta(\varphi_b) = \int \psi_0^*(\varphi, \varphi_b) \psi_0(\varphi, \varphi_{\text{ref}}) d\varphi.$$

The wave functions are found with a discrete variable representation (DVR) [120]. This consists of diagonalising the phase qubit Hamiltonian (5.7) in a discretised eigenbasis of  $\hat{\varphi}$  for different flux biases. The resulting eigenvalues are the energy levels and the associated eigenvectors are the wavefunctions as function of phase  $\varphi$ . This yields  $\eta$  which is then fitted to a third order polynomial, see Fig. 5.2. The fit to a polynomial preserves the analytical aspect of the gradient computation.

The incoherent processes are described by the Lindblad operators

$$\begin{aligned} \hat{L}_{0 \rightarrow m} &= \sqrt{\gamma_0} |m\rangle\langle 0| \\ \hat{L}_{1 \rightarrow m} &= \sqrt{\gamma_1} |m\rangle\langle 1| \\ \hat{L}_{1 \rightarrow 0} &= \sqrt{\gamma_{1 \rightarrow 0}} |0\rangle\langle 1| \end{aligned}$$

## 5.2. OPTIMISATION OF A PHASE QUBIT MEASUREMENT PULSE 73

Whilst the relaxation rate  $\gamma_{1 \rightarrow 0} = T_1^{-1}$  is constant, the tunnelling rates  $\gamma_0$  and  $\gamma_1$  depend on the bias flux. They are found by approximating the potential well by a third order polynomial [126] and using the WKB approximation. This is described in Weiss [138], the result is

$$\gamma_0(\alpha) \simeq 6\omega \sqrt{\frac{\alpha}{\pi}} e^{-\frac{6}{5}\alpha}, \quad (5.9)$$

$$\gamma_1(\alpha) \simeq 432\omega \sqrt{\frac{\alpha^3}{\pi}} e^{-\frac{6}{5}\alpha}. \quad (5.10)$$

$\omega$  is the  $0 \leftrightarrow 1$  transition frequency in the harmonic approximation. We make this approximation more exact by using the DVR of the potential and then finding the eigenenergies for  $|0\rangle$  and  $|1\rangle$  in the shallow well at different bias values. The data for the  $0 \leftrightarrow 1$  transition frequency is fitted to the five parameter function  $a(b + c\varphi_b)^d + e$  so that analytical gradients can be computed. The dimensionless parameter  $\alpha$  also depends on the bias flux, it is given by

$$\alpha(\varphi_b) = 6 \frac{V_{\max} - V_{\min}}{\sqrt{2E_J E_c}(\beta^{-1} + \cos \varphi_{\min})}. \quad (5.11)$$

The potential extrema  $V_{\max/\min}$  are defined in Fig. 5.1. The phase value corresponding to the minimum is  $\varphi_{\min}$ . These quantities all depend on the bias flux. The derivation of this formula is based on the expression of  $\alpha$  found from the WKB approximation and the parameters entering the third order approximation of the qubit's potential. Some additional details are given in appendix A. Although not explicitly indicated, the potential extrema  $V_{\min/\max}$  and the location of the minimum  $\varphi_{\min}$  depend on the bias flux.  $\alpha$  is found numerically by solving for the different terms in Eq. (5.11) for different values of  $\varphi_b$ . The result is shown in Fig. 5.2 the numerical data is then fitted to a second order polynomial to preserve analyticity when computing gradients for the pulse optimisation. In summary, the drift generator of the Liouville superoperator is

$$\mathcal{S}_d = \gamma_{1 \rightarrow 0} \left( |0\rangle\langle 1| \otimes |0\rangle\langle 1| - \frac{1}{2} (|1\rangle\langle 1| \otimes \mathbb{1} + \mathbb{1} \otimes |1\rangle\langle 1|) \right).$$

The control generator is

$$\begin{aligned} \mathcal{S}_c = & i \left( (P \hat{H}_{\text{ref}} P^{-1})^T \otimes \mathbb{1} - \mathbb{1} \otimes P \hat{H}_{\text{ref}} P^{-1} \right) \\ & + \sum_{j=0}^1 \gamma_j(\varphi_b) \left( |m\rangle\langle j| \otimes |m\rangle\langle j| - \frac{1}{2} (|j\rangle\langle j| \otimes \mathbb{1} + \mathbb{1} \otimes |j\rangle\langle j|) \right). \end{aligned}$$

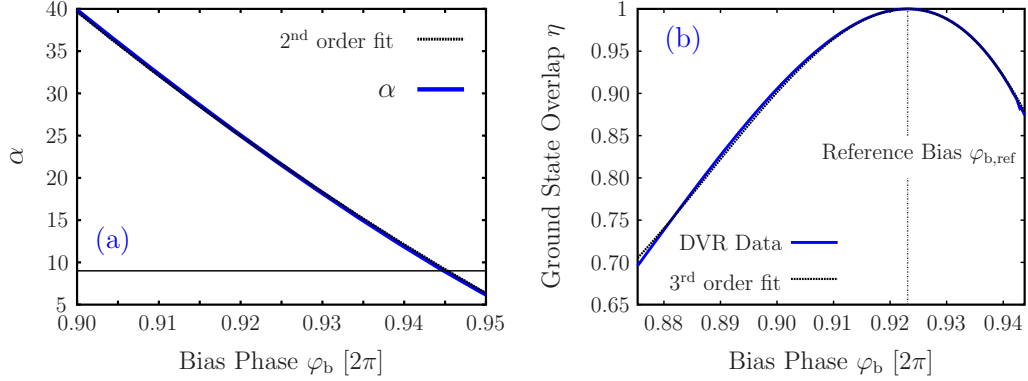


Figure 5.2: Parameters of the phase qubit model. Note that all polynomial fits are carried out over the small range of bias phase necessary to perform the measurement pulse optimisation. (a) parameter controlling the tunnelling rates. The solid line shows the value of  $\alpha$  as computed by Eq. (5.11) whilst the dashed line shows a second order fit. (b)  $|0\rangle \leftrightarrow |1\rangle$  state mixing parameter  $\eta$  as function of the bias phase. The solid line indicates DVR data whilst the dashed line is a third order polynomial fit to the DVR data.

In the first term, the dependence on the bias flux is located in the  $\eta$  parameter in the unitary matrix  $P$ . The non-linearity of this expression in the control  $\varphi_b$  can easily be taken into account in the optimisation using the chain rule.

### 5.2.2 Optimisation Results

The parameters used in the optimisation correspond to typical phase qubit values [126]. These are shown in Tab. 5.1. Sharp jumps in the bias flux can be viewed as Stückelberg oscillations. To prevent this, the pulses are convoluted with a Gaussian. This also results in pulses that are feasible with modern electronics. The optimisation of several pulses of variable time is shown in Fig. 5.3. The first and last two ns are held constant and only change due to variations in the optimisation pixels through the effect of the convolution. The initial solution is a smoothed square pulse. The optimisation adds a bump on the initial rise of the pulse to kick out the  $|1\rangle$  state. It also changes the initial flank of the pulse to avoid population transfer from  $|0\rangle$  to  $|1\rangle$ . This is best seen in Fig. 5.4 where the time evolution resulting from a 10 ns pulse is shown. The pulse fails to let the  $|1\rangle$  state tunnel out. The pulse defects are corrected by the optimisation. Although the rate of change of the flux bias is high during the rising edge, the optimised pulse hardly transfers any population from  $|0\rangle$  to  $|1\rangle$ . The high increase of the optimised pulse makes  $|1\rangle$  tunnel faster as indicated by the  $|1\rangle$  and  $|m\rangle$  populations of Fig. 5.4.

## 5.2. OPTIMISATION OF A PHASE QUBIT MEASUREMENT PULSE75

Table 5.1: Values used in the phase qubit model.

Name	Symbol	Value	unit
Critical Current	$I_0$	2	$\mu A$
Junction Capacitance	$C$	1	$pF$
Flux coupling	$\beta$	4.375	-
Energy Relaxation	$T_1$	500	ns

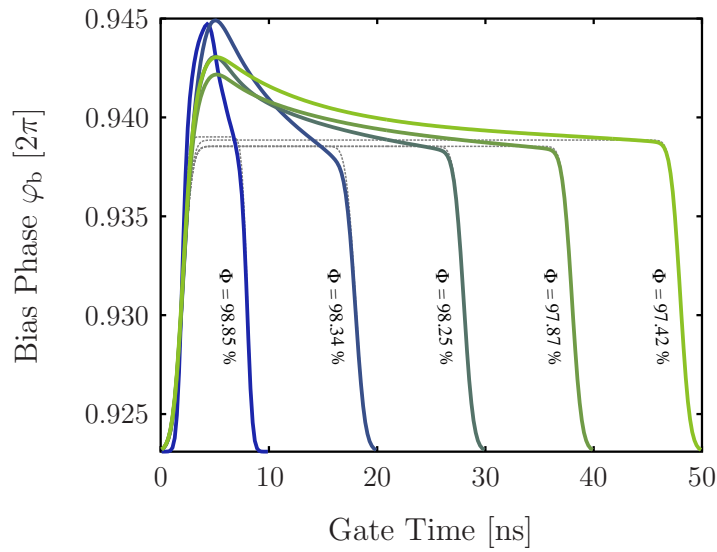


Figure 5.3: Optimal pulses for different gate durations with their corresponding fidelities. The dashed lines show the initial guess. As can be seen the fidelity of the optimal pulses is high even for the fast pulses.

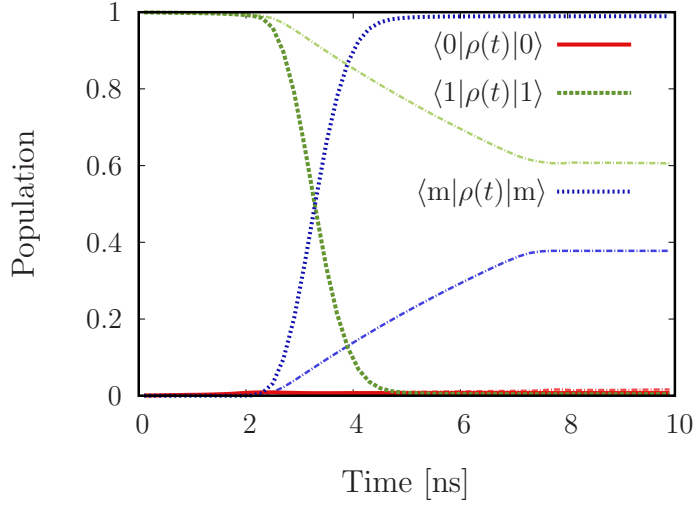


Figure 5.4: Time evolution of the populations for the 10 ns pulse of Fig. 5.3 starting from the  $|1\rangle|1\rangle$  state. As can be seen the initial pulse (corresponding to the thin lines) has a non optimal pulse that fails to transfer population to  $|m\rangle$  this would result in missed counts. The optimal pulse (thick lines) corrects for this as well as preventing population transfers between  $|0\rangle$  and  $|1\rangle$ .

Faster pulses than those in Fig. 5.3 were optimised. A 1.4 ns pulse is shown in Fig. 5.5. However, faster pulses can not be made in this model since it relies upon having at least two states in the meta stable well. This imposes a restriction on the maximum bias flux. Approximating the potential with a third order polynomial and asking for at least two levels in the well leads to the approximate condition  $\alpha > 9$ , details are in appendix A. This threshold value is shown by the horizontal line in Fig. 5.2 and corresponds to a flux bias of  $0.9454 \cdot 2\pi$ . In the pulse optimisation, the flux bias is constrained to be below this value. Thus, upon examining the optimal pulse in Fig. 5.5 it can be seen that the pulse has reached this limit. Therefore the tunnelling rate out of  $|1\rangle$  has reached its maximum within the validity of the three level model.

## 5.2. OPTIMISATION OF A PHASE QUBIT MEASUREMENT PULSE 77

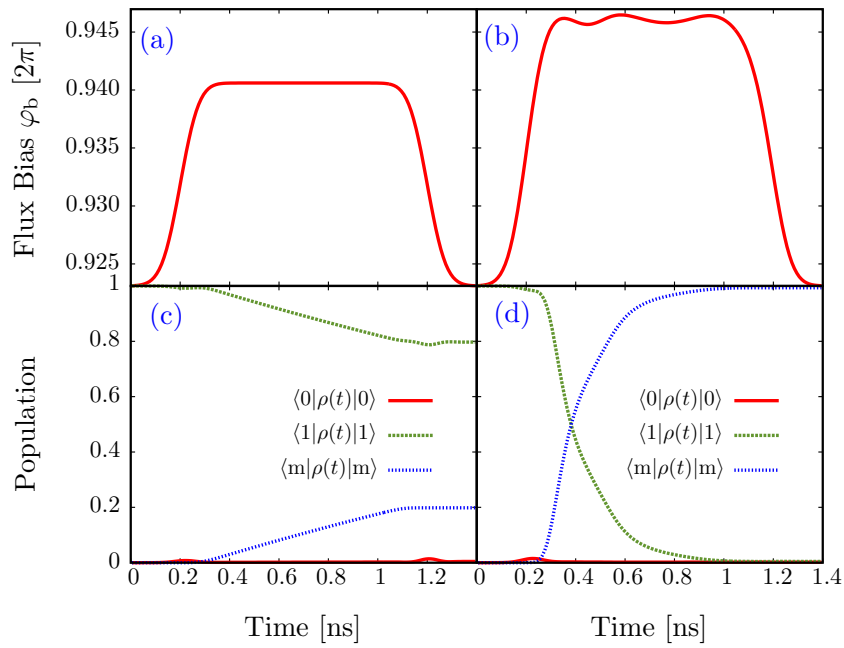


Figure 5.5: Optimisation of a fast readout pulse. (a) initial pulse sequence. (b) Optimised pulse shape. (c) Initial time evolution of populations. Again, the unoptimised pulse fails to let  $|1\rangle$  tunnel into  $|m\rangle$ . (d) Time evolution of populations after pulse optimisation resulting in a high contrast of 98.2%.

### 5.3 Outlook and Conclusions

We have extended the optimal control GRAPE algorithm so that quantum channels with non-unitary time evolutions as target can be optimised. The algorithm was illustrated within the framework of optimising a measurement pulse for a phase qubit where the measurement process relies on incoherent tunnelling processes. The simple model shows a rich interplay between Landau-Zener type physics and the incoherent dynamics. The three level model discussed here is a good starting point for creating a measurement pulse. Going beyond this model could be done in the experiments themselves by using the methodology developed in the next chapter. Measurement is important for superconducting qubits. Optimising pulses for different setups will require additional developments in OCT and could be the topic of future research.

# Chapter 6

## Adaptation by Hybrid Optimal Control

The previous chapters discussed analytical and numerical pulses within the context of superconducting qubits. The engineering of these pulses is open-loop in that a model is assumed and from this model a pulse shape is created. This pulse shape is then meant to be used in experiments. However when the quantum system is improperly characterised, this will fail and the pulse will need to be tuned to the real system. For analytical pulse shapes, with few parameters, this tuning can, to some extent, be carried out manually. Due to the lack of analytical understanding and the large search space, this approach fails for numerical pulses with many parameters. This chapter presents a method to automate the pulse tune-up based on Adaptation by Hybrid Optimal Control (AdHOC). This method is not restricted to superconducting qubits but applies to all fields of quantum optimal control such as controlling the cooperative effects of driving and dissipation [139], to control non-integrable quantum many-body [140] and many electron [129] systems, generating matter-wave entanglement [141, 142] and quantum information devices [38, 115, 143].

### 6.1 OCT and Improperly Characterised Systems

Optimal control theory pulses are designed based on the best available knowledge of the system. This can be insufficient for two reasons i) In many cases, the underlying model cannot be solved with sufficient precision as in the case

---

Published in D. J. Egger & F. K. Wilhelm, Phys. Rev. Lett. **112**, 240503 (2014)

of many-body systems [129] ii) in quantum systems that are engineered or when a human-made apparatus is a key part of the setup, parameters need to be measured with precision compatible with the control task at hand [144], which is often not possible. This necessity to precisely know the underlying model strongly limits harvesting the benefits of optimal control in complex quantum systems.

Here we solve this problem with a hybrid open/closed-loop optimal control method called Adaptation by hybrid optimal control (Ad-HOC). It is designed to overcome shortcomings of the assumed physical model [145], errors on the controls themselves and inaccurate knowledge of the parameters. It starts with a gradient search on a model with the best reasonably achievable accuracy. Ad-HOC then uses the physical system itself as a feed-back to calibrate the control pulses. The gradient search approaches a favourable control over a large distance based on theory and simulation whilst the closed-loop design, done directly on the experiment, takes into account all experimental details [146]. Additionally, the performance index in gradient search can impose extra conditions such as limitations to the fields or robustness. We demonstrate this approach along three tasks: We first show in section 6.2 that pulses can be optimised using only feedback from the experiment. Then, in section 6.2.2, we give an additional example on tuning-up a few parameter analytic pulse. Finally we demonstrate in section 6.3 the efficiency of the hybrid method for a many parameter numerical pulse within the architecture of two superconducting qubits[19]. The latter are particularly sensitive to calibration errors, see section 4.4, making them ideal for testing Ad-HOC.

### 6.1.1 Problem Setting

Delicate engineering of controlled quantum systems, in particular the need to isolate quantum systems from their environment, makes quantum control setups very complex. Such an experiment, sketched in Fig. 6.1 is made of the system to be controlled and the unit (the AWG) producing the control pulses. The pulses are brought from the latter to the former by a chain of electronic or optical components referred to as *control transfer chain*, modelled in section 6.1.2. In this setup, four different mechanisms will degrade the fidelity of an OCT designed pulse. i) Parameter measurement: The quantum system to be controlled is modelled by a drift and control Hamiltonians  $\hat{H} = \hat{H}_d + \sum_i u_i(t) \hat{H}_{c,i}$  with  $\mathbf{u}(t)$  the control fields to be shaped. Imprecise characterisation of parameters entering the drift  $\hat{H}_d$  and controls  $\hat{H}_{c,i}$  will degrade fidelity. ii) Improper characterisation of the control transfer chain's distortion of the pulses [119, 142]. iii) Signal calibration: in practice the control unit generates an electrical signal or laser impulse which is related

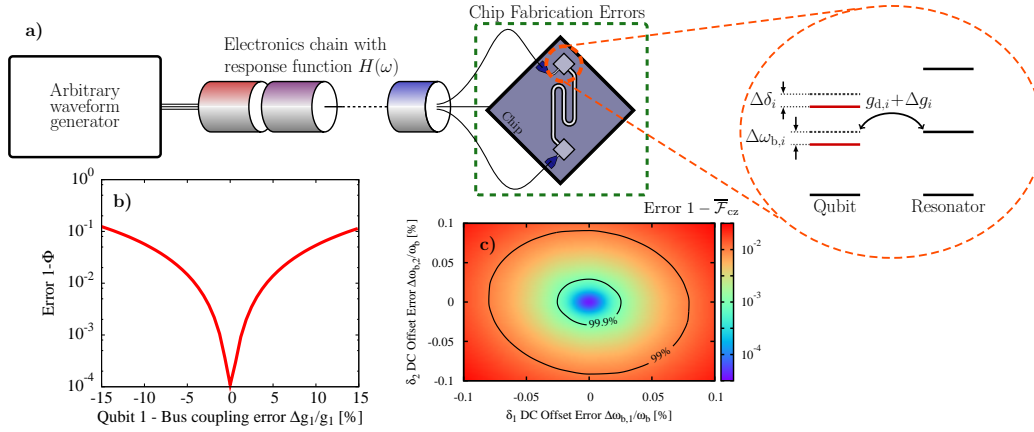


Figure 6.1: a) Sketch of quantum control experiment. The unit generating the control pulses, typically an arbitrary waveform generator (AWG), at room temperature generates the control pulses that are sent through the control transfer chain (sketched as the chain of cylinders) to finally reach the quantum system, often cooled to less than a Kelvin. Error sources are in the parameters modelling the “chip”, the electronics and the calibration of the control signals. Figures b) and c) relate to a CZ gate within the framework of two qubits coupled through a bus resonator. b) Degradation of a 99.99% fidelity CZ gate assuming only an error on the coupling between qubit 1 and the bus. As can be seen the gate fidelity degrades quickly. c) Degradation of CZ gate, optimised to machine precision, due to calibration errors in the qubit controls causing the resonance point with the bus to be missed by an amount  $\Delta\omega_{b,i}$ . The two circles indicate the 99% and 99.9% fidelity limits. Such errors heavily degrade the gate performance.

to  $\mathbf{u}(t)$ . Imprecisions in this relation, e.g. a constant offset, generate errors on the controls themselves which are notoriously hard to correct. iv) Effects that are not taken into account in  $\hat{H}$ . Among many examples are other idling components of a complex quantum system such as a quantum processor, spurious two level fluctuators in Josephson Junctions, as well as slow non-Markovian noise. Errors in parameters can be addressed using broadband control [124, 147] which often leads to cumbersome pulses. Furthermore, no such approach is known for uncertain transfer functions. Practically, these functions as well as the linearity of the signal transfer are extremely hard to verify with the needed precision.

### 6.1.2 Modelling of the Control Transfer Chain

The transfer chain between the quantum system and the AWG can be taken into account in the optimisation [119, 142]. The difficulty is to know its effects (even non-linearities may play a role) to high enough accuracy so as not to degrade OCT designed pulses. This in practice cannot be achieved. Here we describe how control transfer chains can be modelled and how output signals from the AWG relate to the control fields  $\mathbf{u}(t)$  used in the Hamiltonian. The voltages  $\mathbf{V}(t)$  produced by the AWG are not identical to the functions  $\mathbf{u}(t)$ . Instead they are related through a calibration curve  $\mathbf{C}$ . Furthermore the impulse response of the transfer chain  $h$  between the AWG and the experiment can distort the pulses. Thus whilst the AWG produces  $\mathbf{V}(t)$  the quantum system actually receives

$$\mathbf{u}(t) = \int_0^t d\tau (\mathbf{C} \circ \mathbf{V})(t - \tau) h(\tau). \quad (6.1)$$

This can be taken into account using the methodology of Ref. [119] if  $\mathbf{C}$  and  $h$  are precisely known. Practically, these functions as well as the linearity of the signal transfer stipulated in Eq. (6.1) are extremely hard to verify with the needed precision. Whereas errors in parameters of the system can be addressed using broadband control [124, 147, 148], no such approach is known for uncertain transfer functions.

### 6.1.3 Proposed Method

In order to address imperfections of the model, the control loop can be closed by using the experiment itself as feed-back to calibrate the control pulses. An initial gradient search [52, 83] of the optimal pulse is performed with the

best model of the system. This gives control pulses that yield high fidelity on the model but perform sub-optimally in the real system. They still lie close to the optimal point in the control landscape of the actual system given that it is approximated by the model, typically in the basin of attraction of the desired minimum. A set of similar pulses (with model parameters drawn from the error bars of the initial characterisation of the system) are sent to the experiment and their performance measured. The pulses are then updated and the procedure is iterated until either a target performance is reached or convergence halts. Given that it is time consuming to measure the performance of pulses we chose the Nelder-Mead algorithm [149]. It is robust and typically only evaluates 1-2 pulses per iteration. Once the calibration is done, the pulses can be used. At a latter time a few pulse calibration iterations correct for drifts in parameter values and experiments can resume. The Ad-HOC protocol is illustrated in Fig. 6.2. Note that the precise experimental parameters are never identified. Also, this procedure hinges on an efficient method to experimentally measure the performance index. Here, the performance index is the process fidelity which can be measured using Randomised Benchmarking [76, 78, 79], discussed in section 2.2.1. Other than more standard process tomography, it is significantly faster to measure and minimises the impact of state preparation and measurement errors. As shown in [150], randomised benchmarking is well-adapted to fast experimentation and catches a variety of practical errors of different scales.

## 6.2 Closed Loop Demonstration

To show that a pulse can be optimised based only on its performance index we consider random gate synthesis. Then we further demonstrate the closed loop optimisation on a few parameter analytical pulse.

### 6.2.1 Random Gate Synthesis

Inside a black box is a two level system in which the drift and control Hamiltonians are both random Hermitian matrices

$$\hat{H}(t) = \begin{pmatrix} H_1^d & H_2^d + iH_3^d \\ H_2^d - iH_3^d & H_4^d \end{pmatrix} + u(t) \begin{pmatrix} H_1^c & H_2^c + iH_3^c \\ H_2^c - iH_3^c & H_4^c \end{pmatrix}.$$

The random variables  $H_i^x \in \mathbb{R}$  are uniformly distributed in  $[-0.5, 0.5]$ . The black box input is a pulse and the output its fidelity with respect to a target random unitary matrix. For each realisation we seek a different control  $u(t)$  to optimise the fidelity  $\Phi_{\text{QPT}} = |\text{Tr}\{\hat{U}_{\text{rand}}^\dagger \hat{U}\}|^2/4$ . Figure 6.3 shows the mean

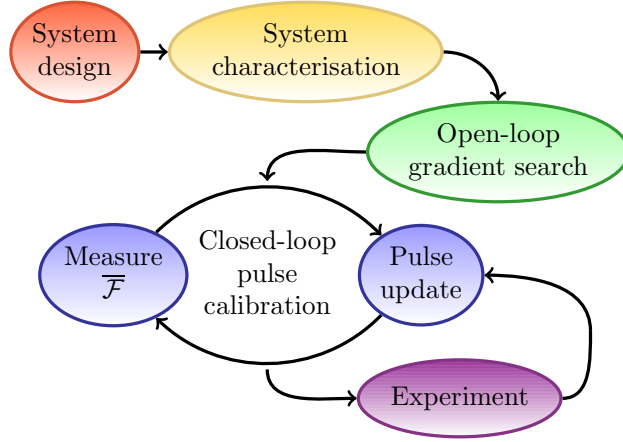


Figure 6.2: Sketch of the Ad-HOC protocol. The physical system and surrounding control and measurement apparatus are designed taking control problems into consideration. The system is then characterised with the best possible precision. Using the parameters from this characterisation the control pulses are created. These are then fine tuned to the system using closed-loop OCT. The pulses are then ready to be used in the experiment and can be recalibrated at a later time to account for drift.

and median error as function of iteration for 100 different realisations of the two level system and target. A histogram of the number of runs required to reach  $1 - 10^{-5}$  fidelity is shown in Fig. 6.4. Instances that converged poorly can be attributed to realisations that are hard to control in the given time, as the commutator between  $\hat{H}^d$  and  $\hat{H}^c$  turns out to be too small. To confirm this statement we plot the number of times  $\Phi_{\text{OPT}}$  was evaluated as function of the smallest relevant matrix norm, defined as

$$\eta = \max \left\{ \left\| \left[ \hat{H}^d, \hat{H}^c \right] \right\|, \left\| \left[ \hat{H}^d, \left[ \hat{H}^d, \hat{H}^c \right] \right] \right\|, \left\| \left[ \hat{H}^c, \left[ \hat{H}^d, \hat{H}^c \right] \right] \right\| \right\}. \quad (6.2)$$

$\| \cdot \|$  is the max norm. The smaller  $\eta$  is, the harder the system is to control. This is reflected in Fig. 6.4. Overall for controllable systems the number of evaluations of  $\Phi$  is low especially since the starting point for the optimisation was the null control  $u(t) = 0 \forall t$ . At very small values of  $\eta$  the system tends to be uncontrollable and some target gates cannot be reached. Two bad instances were removed from the data. These had very small commutator norms and failed to converge.

It is important to recognise in Fig. 6.3 that while demonstrating the power of the closed-loop part of Ad-HOC it also highlights that closed loop control alone needs a large number of steps necessary for a rather elementary control task. Going down this convergence curve with gradient search drastically

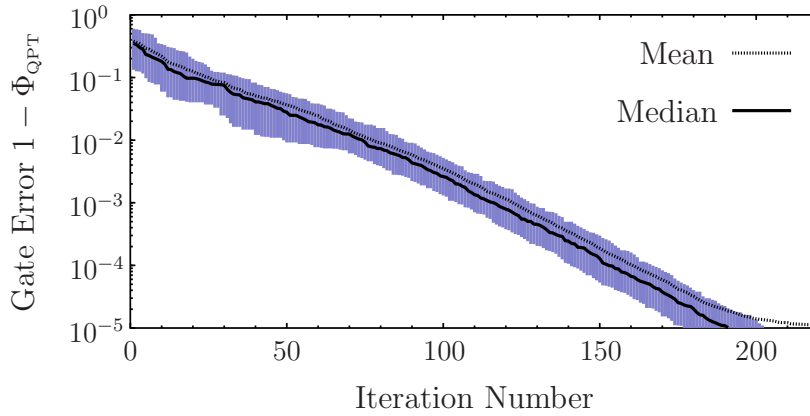


Figure 6.3: Convergence plot showing the optimisation of random gates. 100 pulses were optimised each for a different realisation of the random two level system. The target fidelity of  $1 - 10^{-5}$  is reached rapidly in most cases as indicated by the median. The shaded area includes 68% of all runs centred around the median.

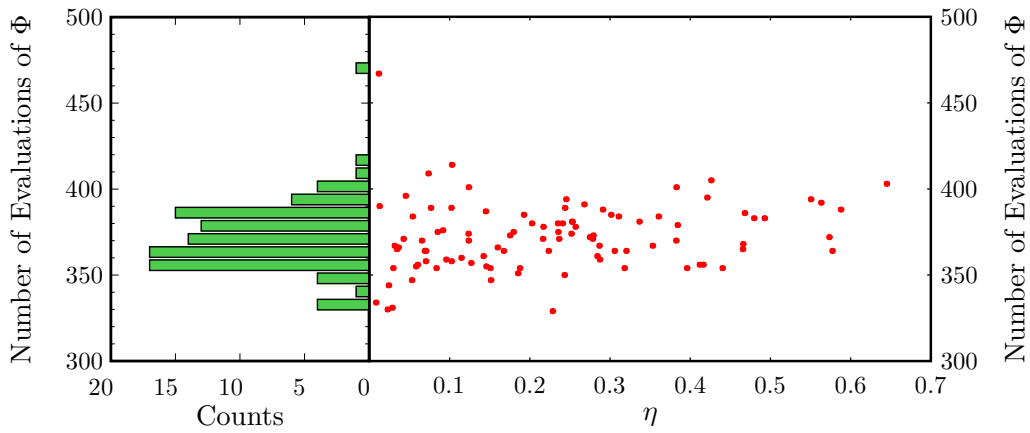


Figure 6.4: Number of evaluations of the fidelity as function of the biggest relevant norm  $\eta$  defined in Eq. (6.2). In this data two points with particularly small  $\eta$  failed to converge and were excluded from the data.

reduces the number of steps to about 50 iterations per order of magnitude error reduction.

### 6.2.2 Few Parameter Pulse Closed-Loop Optimisation Example: Finding DRAG

In a two level system an  $\hat{X}$  gate can be implemented by applying a pulse of area  $\pi$  on the  $\Omega_x$  component of the driving field. However, when a third level is present this is no longer sufficient and DRAG pulses are needed [38, 86]. Generally, full characterisation of the third level - its anharmonicity and coupling ratio, is an extra characterisation step that can be avoided using Ad-HOC. The Hamiltonian for an anharmonic three level system, driven on resonance and in the frame rotating at the frequency of the drive field is

$$\hat{H} = \begin{pmatrix} 0 & 0 & 0 \\ 0 & 0 & 0 \\ 0 & 0 & \Delta \end{pmatrix} + \frac{\Omega_x(t)}{2} \begin{pmatrix} 0 & 1 & 0 \\ 1 & 0 & \sqrt{2} \\ 0 & \sqrt{2} & 0 \end{pmatrix} + i \frac{\Omega_y(t)}{2} \begin{pmatrix} 0 & -1 & 0 \\ 1 & 0 & -\sqrt{2} \\ 0 & \sqrt{2} & 0 \end{pmatrix}.$$

$\Delta$  is the anharmonicity also called qubit non-linearity. To drive the  $0 \leftrightarrow 1$  transition without driving  $1 \leftrightarrow 2$  the  $\Omega_y$  quadrature has to be set to the derivative of  $\Omega_x(t)$  scaled by  $-1/2\Delta$ . To show that few parameter pulses can be quickly calibrated, we assume that the anharmonicity is not known and that the initial pulse is a Gaussian with the wrong area

$$\Omega_{x,\text{initial}}(t) = A \exp \left\{ -\frac{t^2}{2\sigma^2} \right\} \quad \Omega_{y,\text{initial}}(t) = 0.$$

Here  $A$  and  $\sigma$  are chosen at random. The calibration protocol has to find the correct values for  $A$ ,  $\sigma$  and  $\Delta$  such that the time evolution is

$$\hat{U}_{\text{target}} = \begin{pmatrix} 0 & 1 & 0 \\ 1 & 0 & 0 \\ 0 & 0 & e^{i\varphi} \end{pmatrix}$$

An example of the pulses are shown in Fig. 6.5. Figures 6.5(a) and 6.5(c) respectively show the pulses before and after the optimisation which took only 76 evaluations of the fidelity function  $\Phi = |\text{Tr}\{\hat{X}^\dagger \hat{U}\}|^2/9$ . As can be seen by Fig. 6.5(b) the initial pulse is unable to drive any transitions since the amplitude of the pulse is too weak. The fidelity as function of iteration number for these pulses is shown in Fig. 6.6. Closed-loop optimisation quickly finds the optimal pulse.

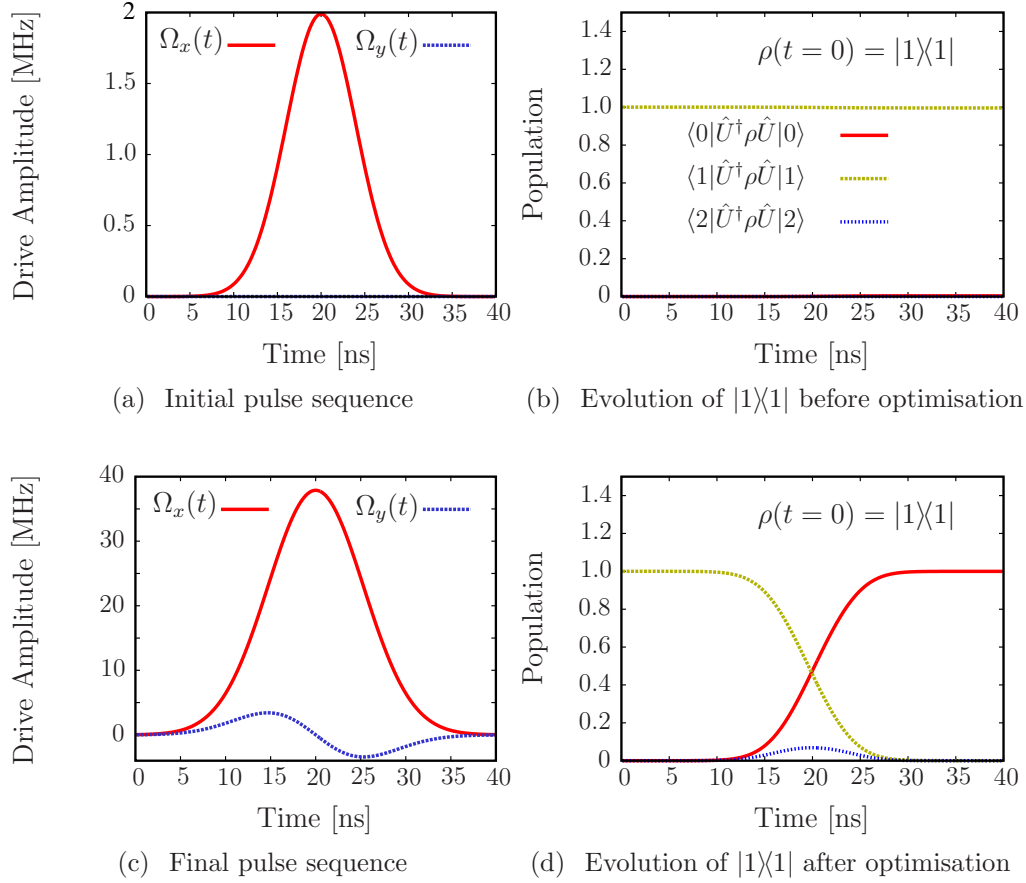


Figure 6.5: Control pulse of a weakly non-linear three level system. The target time evolution is an  $\hat{X}$  gate. A bad initial pulse fails to produce the desired time evolution. (a) and (b) show the initial pulse and the corresponding population evolution when starting with  $|1\rangle\langle 1|$ . The final pulse, found after few iterations, produces an  $\hat{X}$  gate while minimising leakage, see (c) and (d) respectively for pulse and population as function of time.

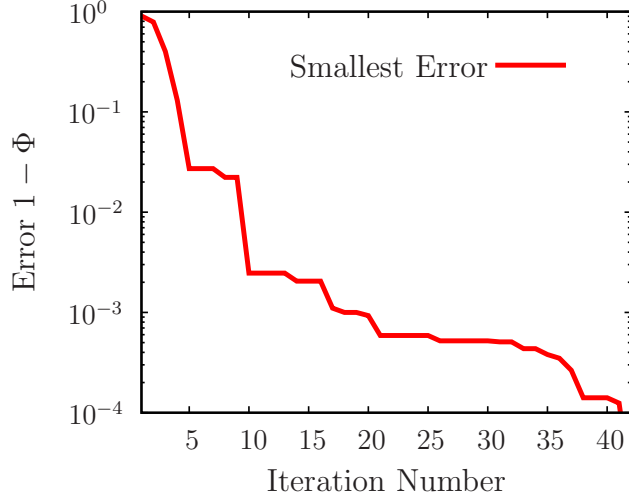


Figure 6.6: Improvement of the fidelity as function of iteration number for the pulses of Fig. 6.5.

### 6.3 Numerical Demonstration for a Realistic Setting

To demonstrate hybrid optimal control in a more complicated yet realistic and genuine system, we choose to create a CZ gate between two superconducting qubits in the qubit-bus-qubit system [114]. In quantum information it is paramount to have extremely high fidelity gates [51] and the systems are well described by the typical setup of Fig. 6.1 with the addition that the quantum system is at the coldest stage in a dilution cryostat. The qubit-bus-qubit Hamiltonian, described in section 4.2, is particularly vulnerable to errors on the controls and parameters as shown in section 4.4. For instance Fig. 6.1b shows the degradation of fidelity due to an error on a single parameter. Fig. 6.1c shows the impact of a DC offset  $\Delta\omega_{b,i}$  on the controls caused by a miscalibration between the AWG's output voltage and the corresponding qubit frequency. This makes the qubit miss the resonance point with the bus. These examples illustrate how severely single errors can impact gate fidelities. In fact, albeit the initial numerical optimisation leading to a pulse that is first-order insensitive to errors, the second derivative is large, making this an example that is specifically unforgiving to model uncertainty and the ideal case for showing Ad-HOC's performance.

First, a gradient search optimises down to machine precision the error of a CZ gate using the quantum process fidelity  $\Phi_{\text{QPT}} = |\text{Tr}\{\hat{U}_{\text{CZ}}^\dagger \hat{U}[\delta_1, \delta_2]\}|^2/d^2$ .  $\Phi_{\text{QPT}}$  measures the overlap between the ideal CZ gate  $\hat{U}_{\text{CZ}}$  and the gate imple-

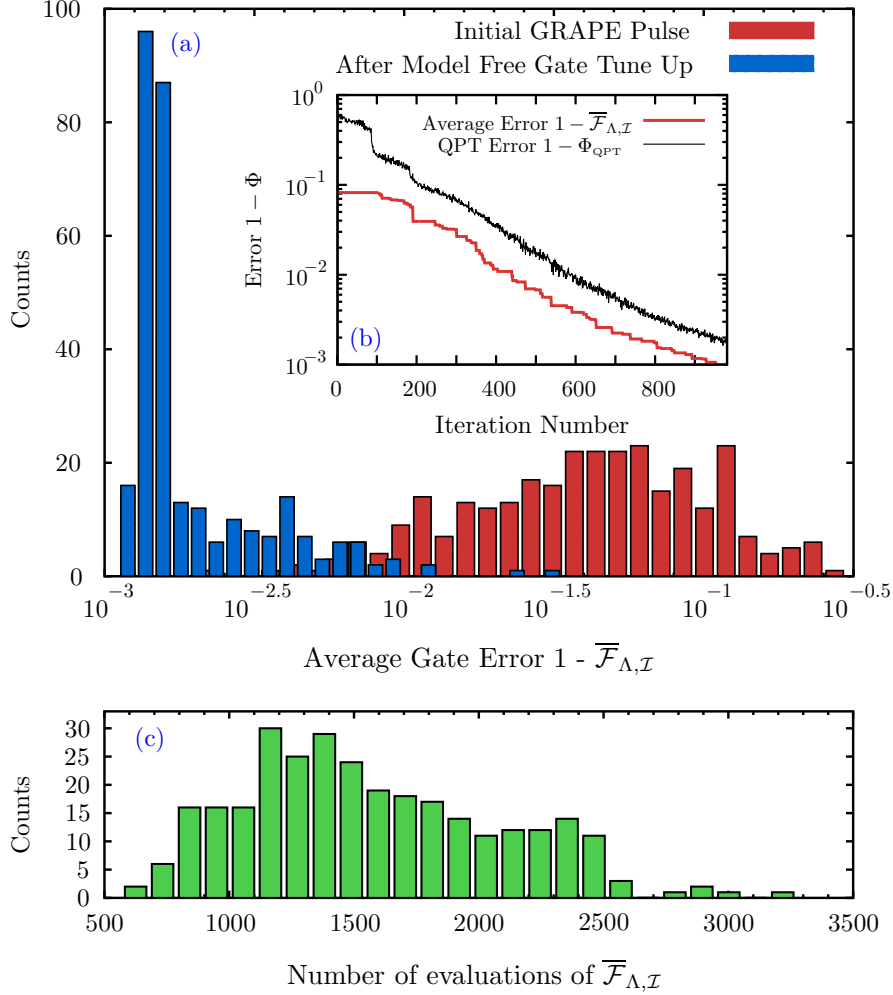


Figure 6.7: Debugging procedure for parameter errors, control transfer chain errors and control DC offset errors. The error of the initial pulse was minimised using a gradient search down to machine precision. The pulses are then calibrated to a specific realisation of the system. (a) Histograms for 300 system realisations. The red histograms show the fidelity of the initial uncalibrated numerical pulse. The blue histograms show the improvement in average gate fidelity after running Ad-HOC. (b) Gate errors as function of the calibration algorithms iteration number. (c) Histograms of the number of times the average gate fidelity had to be evaluated in order to calibrate the pulse to the different system realisations, i.e. to take the red histograms to the blue ones.

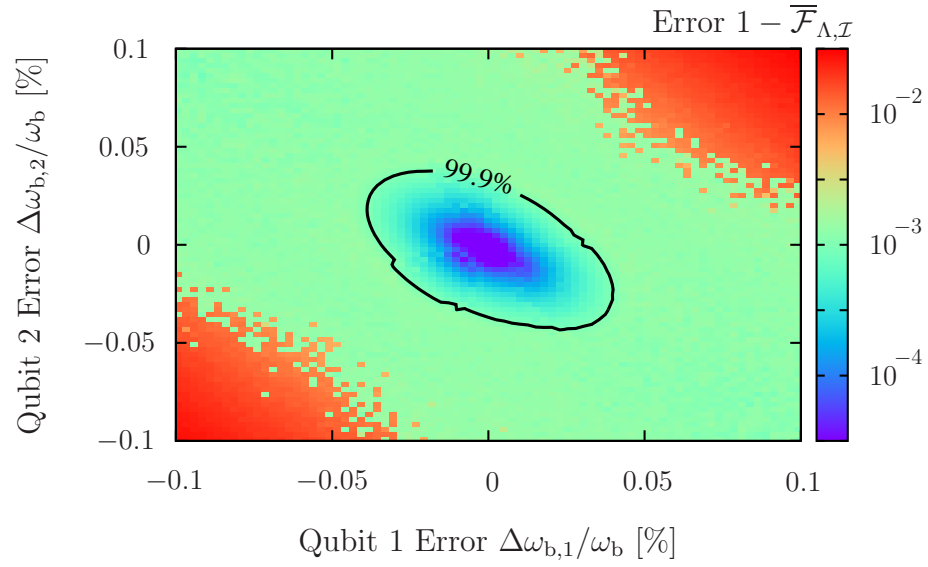


Figure 6.8: Average error for the CZ gate as function of the DC offset error  $\Delta\omega_{b,i}$  introduced by miscalibrating the AWG's output to the qubit frequency. Ad-HOC greatly improves the fidelity of the pulse as can be seen by comparing to Fig. 6.1(c) where the pulses found by OCT were not calibrated to the system. The central region of high fidelity does not change since the target fidelity for the calibration protocol was 99.9%.

mented by the controls  $\delta_i$ .  $d$  is the dimension of the Hilbert space. Next, the parameters in the model  $g_i$  and  $\Delta_i$ , as well as the DC offsets  $\Delta\omega_{b,i}$  and the standard deviation of the transfer chain’s impulse response are promoted to random variables following Gaussian statistics with variances reflecting the precision of actual measurements [151]. The parameters used are given in Tab. 6.1. We then compute the average gate fidelity  $\overline{\mathcal{F}}$  for many different realisations of the system. This is shown in Fig. 6.7(a) by the red histograms. As expected the fidelities are nowhere close to optimal ranging between 99% and 68%, clearly insufficient for quantum computing. Finally each instance is reoptimised using the closed loop part of Ad-HOC resulting in the blue histograms in Fig. 6.7(a). Ad-HOC increased the fidelity by more than an order of magnitude. Fig. 6.7(b) shows a typical decrease in error during the closed loop optimisation. As  $\overline{\mathcal{F}}$  is being maximised,  $\Phi_{\text{QPT}}$ , computed for comparison, also increases. The corresponding number of required evaluations of  $\overline{\mathcal{F}}$  for each realisation is shown in Fig. 6.7(c). A further illustration of the protocol’s performance is shown in Fig. 6.8. In this case only the control DC offset error  $\Delta\omega_{b,i}$  was present. As can be seen by comparing to Fig. 6.1(c) the fidelity has been increased over a wide range of possible  $\Delta\omega_{b,i}$ ’s. This shows how successful Ad-HOC is in dealing with errors on the controls themselves.

Table 6.1: Parameters used in the qubit-bus-qubit model. The coupling strength  $g$  is given as function of the Qubit-Bus swap time by  $(2T_{\text{swap}})^{-1}$ . The imprecision is given relative to the parameter it refers to. When promoting the parameters to random variables this imprecision serves as standard deviation. When performing the closed loop optimisation, the AWG voltage calibration  $\Delta\omega_{b,i}$  is chosen randomly with mean zero and standard deviation of 0.1% of the bus frequency. System realisations with unphysical parameters are discarded, e.g.  $\sigma_{\text{filt}}$  cannot be smaller than zero.

Name	Symbol	Q. 1	Q. 2	unit	Imprecision
Q.-Bus Swap Time	$T_{\text{swap},i}$	12.6	9.2	ns	-
Q.-Bus Coupling Strength	$g_i$	40	54	MHz	4.0%
Q. non-linearity	$\Delta_i$	-59	-71	MHz	4.0%
Bus Frequency	$\omega_b$	6.1		GHz	0.1%
Convolution function error	$\sigma_{\text{filt}}$	1		ns	40.0%

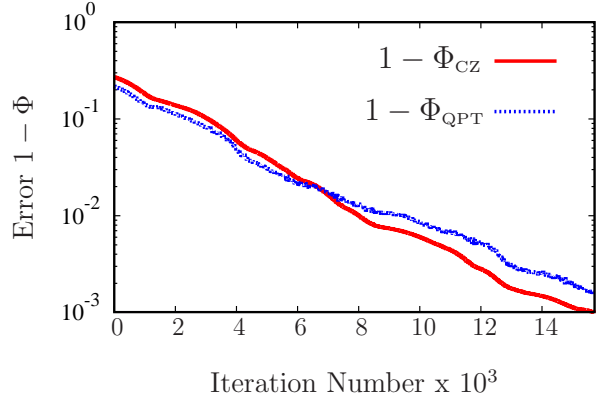


Figure 6.9: Model free calibration with a gate tailored fidelity. At each iteration the gate overlap fidelity is also computed and, as can be seen, optimising  $\Phi_{\text{CZ}}$  also optimises  $\Phi$ .

### 6.3.1 Gate-Taylored Quality Parameters Optimisation

The previous sections emphasize randomised benchmarking as the fidelity measure. This fidelity is applicable when the desired gate is a Clifford gate. Here is shown that a gate specific fidelity can also be used to calibrate the pulse. We illustrate this with the optimisation of a CZ gate. We define the following fidelity measure

$$\Phi_{\text{CZ}} = \sum_{ij \in \{01,10,11\}} \frac{|U_{ij,ij}|^2}{6} [1 + (-1)^{ij} \cos(\arg(U_{ij,ij}))].$$

Here  $U_{ij,ij}$  is the element of the time evolution operator mapping the state  $|ij\rangle$  onto itself. The terms  $|U_{ij,ij}|^2$  are the qubit populations after the pulse sequence for a specific input state. The argument of these terms can be found using Ramsey measurements. A gate that is unitary and optimises  $\Phi_{\text{CZ}}$  has to be a good CZ gate. An example of this fidelity as function of the iteration number is shown in Fig. 6.9. The initial pulse was optimised by GRAPE up to 80% fidelity using  $\Phi = |\text{Tr}\{\hat{U}_{\text{CZ}}^\dagger \hat{U}\}|^2/d^2$ . The remaining calibration was done with the model free part of Ad-HOC. The target fidelity was set to be  $\Phi_{\text{CZ}} = 99.9\%$ . It can be seen that the intrinsic gate fidelity follows closely.

## 6.4 Robustness

In the previous examples the sampling of the integral in Eq. (2.7) introduces noise into the fidelity measure. Noise would also be present in an experiment but for different reasons. Here is further investigated the effect of noise on convergence. We consider the fidelity  $\Phi$  which can be computed without introducing noise. A noiseless run of closed-loop optimisation is compared to a noisy run. Noise is artificially added to  $\Phi$  by a depolarising channel [1]

acting  $n$  times out of  $m$  with uniform probability  $p$ . The smaller  $m$  is, the more sampling noise is added to  $\Phi$ . The noisy fidelity used was

$$\Phi_{\text{noisy}} = \frac{n}{md} + \frac{m-n}{m}\Phi$$

where  $d$  is the dimension of the Hilbert space. The noisy and noiseless optimisations are shown in Fig. 6.10, they converge at the same speed until the noisy case halts. This termination results from the increase in fidelity, averaged over several iterations, being smaller than the noise threshold  $\Delta\Phi_{\text{th}}$ . For this case, the threshold is

$$\Delta\Phi_{\text{th}} = \frac{d\Phi_{\text{dep.}} - \bar{p} - \sigma_p}{d(1 - \bar{p} - \sigma_p)} - \frac{d\Phi_{\text{dep.}} - \bar{p} + \sigma_p}{d(1 - \bar{p} + \sigma_p)}.$$

The estimation of  $p$  is  $\bar{p} \pm \sigma_p = n/m \pm 1/12\sqrt{m}$ , the factor 12 comes from the uniform distribution. When, on average, an operation on the Nelder-Mead simplex improves  $\Phi$  of the worst pulse by less than a threshold difference  $\Delta\Phi_{\text{th}}$ , the optimisation will not be able to improve the fidelity any longer because the experiment cannot distinguish fidelities sufficiently well. This is illustrated in Fig. 6.10(b) showing the difference between successive iterations of fidelity of the worst pulse  $\Phi_w$  in the pulse simplex.

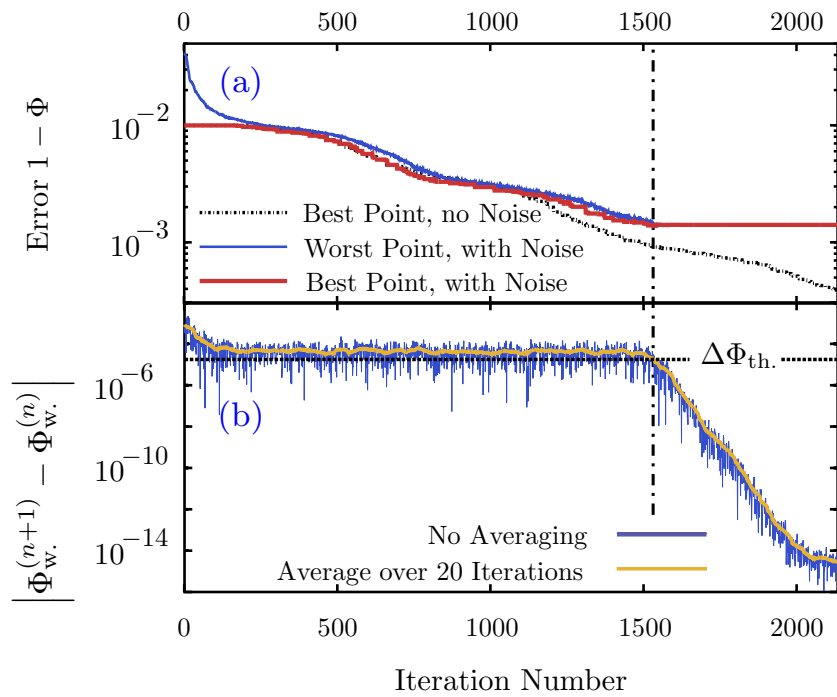


Figure 6.10: (a) Convergence speed of a single optimisation comparing the cases when a depolarising channel adds noise and when the optimisation is noiseless. (b) Difference in fidelity of the worst point in the simplex between subsequent iterations in a noisy optimisation. As long as, on average, this difference is greater than the noise level, the optimisation continues.

## 6.5 Conclusions

Model-free calibration was pioneered in [146] using genetic algorithms, which we typically found 1.5 orders of magnitude slower in convergence. The Nelder-Mead algorithm has been used in tuning dynamical decoupling sequences in [152] and is part of the CRAB optimal control scheme [140] without initial gradient search. The closed-loop part of Ad-HOC has been experimentally implemented for a CZ gate done between two coupled superconducting qubits [150] and enabled the high gate fidelities in [75].

In conclusion we have demonstrated Adaptive Hybrid Optimal Control (Ad-HOC), a protocol for overcoming model imperfection and incompleteness afflicting the design of control pulses for quantum systems. The protocol is efficient and can be applied to almost arbitrary quantum control experiments as it can be used with any fidelity measure that captures the essence of the desired time evolution. We showed that noise does not affect convergence speed but rather the terminal fidelity. Therefore higher fidelity can be gained by increasing the measurement precision. Ad-HOC, overcomes model inaccuracies and errors on the controls themselves.



**Part III**

**Quantum Simulations**



# Chapter 7

## Left-Handed Transmission Lines

*Chantre*  
*Et l'unique cordeau des trompettes marines*

Apollinaire

Quantum optics addresses the interaction of quanta of matter — atoms — with quanta of electromagnetic fields — photons. This is beautifully realised in cavity quantum electrodynamics (QED) [153], where the interaction between those units is made strong by confining the field into a small mode volume [116]. Circuit QED takes this further by confining microwave photons in a quasi 1D strip-line cavity and using superconducting qubits as *artificial* atoms with a large dipole moment [20, 116]. Next to being a promising architecture for quantum computing, a multitude of basic quantum optical effects has been demonstrated [154]. Going beyond what can be reached in atomic systems, an ultrastrong coupling regime — where the coupling strength becomes comparable to the atomic energy scales — has been proposed [155] and achieved [156, 157]. Furthermore in the circuit QED approach, elements are entirely human-made and can hence be flexibly engineered. This can lead to coupling to multiple modes [158–162] either in the same or distinct cavities. There is a wealth of proposals exploiting these features to create complex photonic states [163–165] involving a large number of cavities. Parallel to these developments are those of left-handed meta-materials. They have a wide variety of applications in photonics from the microwave to the visible range such as invisibility cloaks and perfect flat lenses [166, 167]. For

---

Published in D. J. Egger & F. K. Wilhelm, Phys. Rev. Lett. **111**, 163601 (2013)

classical guided microwaves, left-handed transmission lines have been proposed [168] and studied [169] on the macroscopic scale. In the following we show how a hybrid transmission line, made of left and right-handed media, coupled to a flux qubit gives rise to ultrastrong multi-mode coupling. We then show how this system can be used as an analogue quantum simulator for the Spin-Boson model [170].

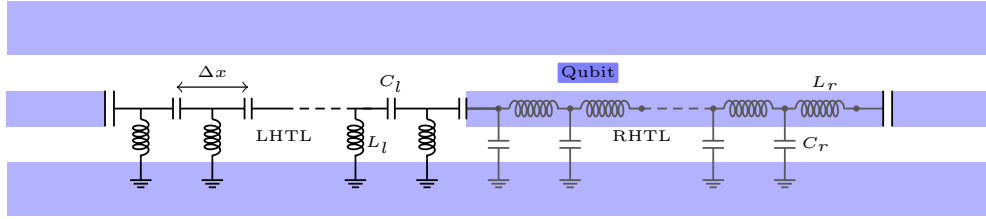


Figure 7.1: Discrete LHTL coupled to a continuous RHTL . The regular right-handed part of the transmission line is on the right, connected to a left-handed line shown on the left. The terminating capacitors allow to externally access the modes. The qubit couples to the right-handed component. Additional stray inductances and capacitances in the left handed line can be taken into account as shown by Eleftheriades, *et al.* [168]. They do not change the physics. The light blue areas indicate strip-lines and ground planes.

## 7.1 The System

In one-dimension, left-handedness is defined as the wave vector  $\mathbf{k}_l$  and the Poynting vector having opposite orientation; the phase and group-velocity are opposite corresponding to a falling dispersion relation  $\partial\omega(k)/\partial k < 0$ . This can be achieved [168] by a discrete array of series capacitors and parallel inductors to ground, see Fig. 7.1. A low loss left-handed transmission line (LHTL) can be realised with superconductors [169, 171]. This is the dual (inductors and capacitors interchanged) of the usual [172] discrete representation of the right-handed transmission line (RHTL). In practice, the LHTL remains a metamaterial composed of discrete elements, whereas the RHTL is a metal strip represented as the continuum limit of a ladder network [172].

### 7.1.1 Equations of Motion

The right and left-handed parts of the transmission line are respectively shown in the right and left side of Figure 7.1. In terms of magnetic flux  $\Phi$

their uncoupled Lagrangians [116, 173] are

$$\begin{aligned}\mathcal{L}_r &= \sum_{n<0} \left[ \frac{1}{2} C_r \dot{\Phi}_n^2 - \frac{1}{2L_r} (\Phi_n - \Phi_{n-1})^2 \right] \\ \mathcal{L}_l &= \sum_{n>0} \left[ \frac{1}{2} C_l (\dot{\Phi}_n - \dot{\Phi}_{n+1})^2 - \frac{1}{2L_l} \Phi_n^2 \right]\end{aligned}$$

$C_r$  and  $L_r$  are the capacitance and inductance of the discrete model of the RHTL which will then be taken to the continuum limit.  $C_l$  and  $L_l$  are the capacitance and inductance of a unit cell of the LHTL. Through the Euler-Lagrange equation, these Lagrangians produce the following equations of motion

$$\frac{1}{C_r L_r} (\Phi_{n-1} - 2\Phi_n + \Phi_{n+1}) = \ddot{\Phi}_n \quad (7.1)$$

$$C_l L_l (\ddot{\Phi}_{n-1} - 2\ddot{\Phi}_n + \ddot{\Phi}_{n+1}) = \Phi_n \quad (7.2)$$

The latter are none other than Kirchoff's current law for each cell of the transmission line. This is seen by noting that, for the case of the RHTL, the voltage on capacitor  $n$  is  $V_n = -\dot{\Phi}_n$  and the current flowing through this capacitor is  $I_{C_n} = C_r \dot{V}_n$ . The flux difference between two nodes relates to current through  $\Phi_n - \Phi_{n-1} = L_r I_{n-1}$ . Thus Eq. (7.1) is none other than  $I_n - I_{n-1} = I_{C_n}$ . Similar reasoning applies to the LHTL.

We can understand the physics of this line as follows: For any ladder network with discrete time-translation symmetry, the eigenmodes are (propagating or decaying) plane waves with a dispersion relation derived from the solutions of [172]

$$\sin\left(\frac{k\Delta x}{2}\right) = \pm \frac{1}{2} i \sqrt{\frac{Z_s}{Z_p}} \quad (7.3)$$

For a RHTL, substituting impedances of the series elements  $Z_s = i\omega L_r$  and parallel elements  $Z_p = (i\omega C_r)^{-1}$  gives the usual dispersion

$$\omega_r(k_r) = \frac{2}{\sqrt{C_r L_r}} \sin\left(\frac{k_r \Delta x}{2}\right) \xrightarrow{\text{continuum}} \frac{k_r}{\sqrt{c_r l_r}}$$

For the LHTL, we interchange the roles of inductors and capacitors and obtain from Eq. (7.3) propagating modes (real-valued  $k$  for real  $\omega$ ) with the opposite dispersion relation

$$\omega_l(k_l) = \frac{1}{2\sqrt{C_l L_l} \sin\left(\frac{k_l \Delta x}{2}\right)} \quad (7.4)$$

Here,  $C_{l/r}$  and  $L_{l/r}$  are capacitances and inductances as defined in Fig. 7.1 and  $c_r$  and  $l_r$  are the capacitance and inductance per unit length in the RHTL.  $\Delta x$  is the size of a unit cell. In the LHTL the frequency cut-off due to Bragg reflection is a low frequency cut-off and is given by  $\omega_{\text{IR}} = 1/2\sqrt{C_l L_l}$ .

### 7.1.2 Density of Modes of the Coupled Left and Right-Handed Transmission Lines

Unusual physics arises when right- and left-handed media are interfaced [166]. We realise this with a coupled transmission line (CTL) shown in Fig. 7.1, a discrete LHTL coupled to a RHTL to be taken into the continuum limit. Here we show that close to the infra-red cut-off, introduced by the LHTL, the modes in the RHTL are very similar in frequency and spatial profile. The density of modes is obtained by solving a boundary value problem for the voltage along the CTL.

#### Voltage and Current

The voltage can be decomposed into two plane waves  $V^+$  ( $V^-$ ), originating in the RHTL (LHTL), and propagating towards the boundary. The waves propagating along the CTL must have the same energy therefore we set  $\omega_l = \omega_r = \omega$ . These two dimensionless voltages with unit amplitude are

$$V_n^+(t) = e^{-i\omega t} \begin{cases} e^{-ik_r n \Delta x} + \Gamma^+ e^{ik_r n \Delta x} & n \geq 0 \\ T^+ e^{ik_l n \Delta x} & n \leq 0 \end{cases} \quad \text{and} \quad (7.5)$$

$$V_n^-(t) = e^{-i\omega t} \begin{cases} T^- e^{ik_r n \Delta x} & n \geq 0 \\ e^{-ik_l n \Delta x} + \Gamma^- e^{ik_l n \Delta x} & n \leq 0 \end{cases} . \quad (7.6)$$

When the waves encounter the interface at cell  $n = 0$  they are partially transmitted and reflected;  $\Gamma^\pm$  and  $T^\pm$  are the reflection and transmission coefficients for  $V^\pm$ ; they will be determined later by continuity of the voltage and current at the boundary. It is important to note that in the left-handed line the group velocity is negative: the sign of the wave vector is opposite to the Poynting vector. The voltages given by (7.5) and (7.6) are associated with currents found through Kirchoff's laws in the appropriate part of the line. These are  $I_{n-1} - I_n = i\omega C_r V_{n-1}$  in the RHTL and  $I_n - I_{n+1} = iV_n/\omega L_l$  in the LHTL. It is more common to express currents using impedances. Following

[172] the impedances of the RHTL and LHTL,  $Z_r$  and  $Z_l$  respectively, are

$$Z_r = -\frac{V_n^-}{I_n^-} = -\frac{e^{-ik_r\Delta x} - 1}{i\omega C_r} \xrightarrow{\Delta x \rightarrow 0} \sqrt{\frac{L_r}{C_r}}. \quad (7.7)$$

$$Z_l = \frac{V_n^+}{I_n^+} = -i\omega L_l (1 - e^{-ik_l\Delta x}) = \sqrt{\frac{L_l}{C_l} \left(1 - \frac{\omega_{\text{IR}}^2}{\omega^2}\right)} - \frac{i}{2\omega C_l} \quad (7.8)$$

When taking the continuum limit, the dispersion relation was used and the usual form for the impedance of a continuous strip line is recovered. Since  $\omega \geq \omega_{\text{IR}}$  the quantity under the square root is always positive. Furthermore the impedances enjoy the property that  $|Z_r| = \sqrt{L_r/C_r}$  and  $|Z_l| = \sqrt{L_l/C_l}$ . The terms featuring a frequency dependency are the result of the discreteness of the model. This can further be confirmed by taking the long wavelength limit; when  $\lambda \gg \Delta x$  it is expected that the discrete transmission lines behave like continuous ones. For the LHTL the long wavelengths are achieved by the limit  $\omega \rightarrow \infty$  for which  $Z_l \rightarrow \sqrt{L_l/C_l}$ . Making use of the impedance the currents are given by

$$I_n^+(t) = e^{-i\omega t} \begin{cases} \frac{1}{Z_r} e^{-ik_r n \Delta x} - \frac{\Gamma^+}{Z_r} e^{ik_r n \Delta x} & n \leq 0 \\ \frac{T^+}{Z_l} e^{ik_l n \Delta x} & n \geq 0 \end{cases} \quad \text{and} \quad (7.9)$$

$$I_n^-(t) = e^{-i\omega t} \begin{cases} -\frac{T^-}{Z_r} e^{ik_r n \Delta x} & n \leq 0 \\ -\frac{1}{Z_l^*} e^{-ik_l n \Delta x} + \frac{\Gamma^-}{Z_l} e^{ik_l n \Delta x} & n \geq 0 \end{cases}. \quad (7.10)$$

To fully determine the voltage and currents along the CTL the reflection and transmission coefficients need to be found. Imposing voltage and current continuity across the interface results in the equations

$$\begin{cases} T^\pm = \Gamma^\pm + 1 \\ \frac{T^+}{Z_l} = \frac{1}{Z_r^*} - \frac{\Gamma^+}{Z_r} \\ \frac{T^-}{Z_r} = \frac{1}{Z_l^*} - \frac{\Gamma^-}{Z_l} \end{cases}$$

Which are solved by

$$\Gamma^+ = \frac{Z_l - Z_r^*}{Z_l + Z_r} \frac{Z_r}{Z_r^*},$$

$$\Gamma^- = \frac{Z_r - Z_l^*}{Z_l + Z_r} \frac{Z_l}{Z_l^*}.$$

These coefficients enjoy the property  $|\Gamma^+|^2 = |\Gamma^-|^2$ .

### Power Flow in the CTL

Given that the CTL is a passive system energy flowing in the RHTL must be equal to energy flowing in the LH TL. This consistency check is shown here. The time averaged power along a transmission line is  $P_{av}^\pm = \text{Re}[V_n^\pm I_n^{\pm*}]/2$ . It is important to note that we expect the outcome to be independent of the position along the CTL since there are no power sinks or sources. Thus, in terms of time averaged power, the following must hold

$$\frac{1}{2} \text{Re} [V_{n<0} I_{n<0}^*] = \frac{1}{2} \text{Re} [V_{n>0} I_{n>0}^*]$$

If the + solution is considered, i.e. voltage given by (7.5) and current by (7.9), then the energy flows in the RHTL and LH TL are respectively

$$P_{av}^{r+} = \frac{1}{2} \text{Re} \left[ \frac{1}{Z_r} - \frac{|\Gamma^+|^2}{Z_r} - \frac{\Gamma^{+*}}{Z_r^*} e^{ik_r n \Delta x} + \frac{\Gamma^+}{Z_r} e^{-ik_r n \Delta x} \right] = \frac{2 \text{Re}(Z_l)}{|Z_r + Z_l|^2}$$

$$P_{av}^{l+} = \frac{1}{2} \text{Re} \left[ \frac{|\Gamma^+|^2}{Z_l^*} \right] = \frac{2 \text{Re}(Z_l)}{|Z_r + Z_l|^2}$$

This result was reached by using the expression of the reflection and transmission coefficients in terms of impedance. The two terms with  $\Gamma^+ e^{-ik_r}/Z_r$  arise from the interference between incoming wave and reflected wave, however they do not contribute to the power since  $A - A^* \in i\mathbb{R}$ . By comparing these two equations it is immediately seen that  $P_{av}^{r+} = P_{av}^{l+}$ , i.e. energy is conserved. The same reasoning applies if the - solutions of voltage and current are considered.

### Impedance Matching

For the two parts of the line to be able to communicate, the energy flow across the boundary must be greater than zero. Using  $Z_r^2 = L_r/C_r$  and

writing  $P_{\text{av}}^+$  as function of frequency yields

$$P_{\text{av}}^+(\omega) = \frac{2\sqrt{\frac{L_l}{C_l} \left(1 - \frac{\omega_{\text{IR}}^2}{\omega^2}\right)}}{\frac{L_r}{C_r} + \frac{L_l}{C_l} + 2\sqrt{\frac{L_r L_l}{C_r C_l} \left(1 - \frac{\omega_{\text{IR}}^2}{\omega^2}\right)}}$$

The flow of power across the boundary is thus maximum when the impedances are matched in magnitude i.e.  $L_r/C_r = L_l/C_l$ . In this case and since the voltage is taken to have unit amplitude, the maximum power is  $(2Z_r)^{-1}$ . This corresponds to the limit  $\omega \rightarrow \infty$  for which the two lines are perfectly matched. Additionally and regardless of impedance, the following properties hold when going closer in frequency to the IR cut-off

$$\begin{aligned} \lim_{\omega \rightarrow \omega_{\text{IR}}} P_{\text{av}} &= 0 \\ \lim_{\omega \rightarrow \omega_{\text{IR}}} \frac{\partial P_{\text{av}}}{\partial \omega} &= \infty \end{aligned}$$

The power flow as function of frequency increases monotonically. The infinite slope of  $P_{\text{av}}(\omega)$  at  $\omega_{\text{IR}}$  guarantees that the first mode will have non-zero power flowing across the boundary. An example of the power across the boundary of a 50  $\Omega$  CTL is shown in Fig. 7.2. The black dots represent the normal modes of Fig. 7.3. The lowest mode obtained in a real geometry, with frequency  $\omega_1/2\pi = 4.149$  GHz has a power flow of 42.1% of the maximum despite the fact that  $P_{\text{av}}(\omega_{\text{IR}}) = 0$ .

### Normal Modes of the Coupled Transmission Line

The voltage along the line, for mode  $k$ , at node  $n$  and time  $t$  is given by a superposition of  $V^+$  and  $V^-$

$$V_{n,k}(t) = V_{n,k}^+(t) + V_0^{(k)} e^{i\Delta\phi_k} V_{n,k}^-(t).$$

It has a frequency  $\omega_k$  and wave vectors  $k_{r,l}(\omega_k)$ . The mode dependent, real coefficients  $V_0^{(k)}$  and  $\Delta\phi_k$  are used to match phases and amplitudes. The discussions in the last sections were restricted to the interface and along the lines but did not include effects linked to the finite length of the CTL. The boundary conditions for an open-circuited CTL are given by charge neutrality: the spatial integral of the voltage must vanish at the extremities of the TL [116]. The voltage integrals  $\theta^-$  and  $\theta^+$  are respectively found from

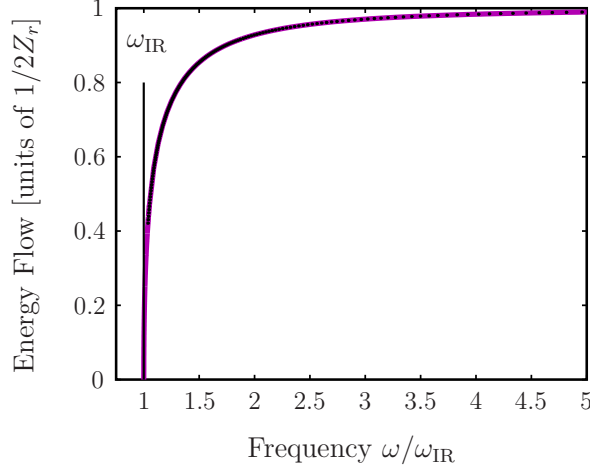


Figure 7.2: Power flow across the boundary as function of mode frequency. The black dots indicate the frequency of the numerically found modes discussed in Fig. 7.3.

equations (7.5) and (7.6)

$$\theta_n^+(t) = e^{-i\omega t} \begin{cases} -\frac{1}{ik_r \Delta x} e^{-ik_r n \Delta x} + \frac{\Gamma^+}{ik_r} e^{ik_r n \Delta x} & n \leq 0 \\ \frac{T^+}{ik_l} e^{ik_l n \Delta x} & n \geq 0 \end{cases}$$

$$\theta_n^-(t) = e^{-i\omega t} \begin{cases} \frac{T^-}{ik_r} e^{ik_r n \Delta x} & n \leq 0 \\ -\frac{1}{ik_l} e^{-ik_l n \Delta x} + \frac{\Gamma^-}{ik_l} e^{ik_l n \Delta x} & n \geq 0 \end{cases}$$

The node in the right-handed line furthest away from the interface is labelled  $N_r$  and the one for the left-handed line is  $-N_l$ . The boundary conditions are  $|\theta_{N_r, k}|^2 = |\theta_{-N_l, k}|^2 = 0$ ; implying that a solution for the following non-linear system of equations has to be found

$$\begin{cases} 0 = \left| e^{-2ik_r N_r \Delta x} - \Gamma^+ - V_0^{(k)} T^- e^{i\Delta\phi_k} \right|^2 \\ 0 = \left| V_0^{(k)} e^{i2k_l N_l \Delta x} - V_0^{(k)} \Gamma^- - T^+ e^{-i\Delta\phi_k} \right|^2 \end{cases}.$$

It is understood that  $\Gamma^\pm$ ,  $T^\pm$ ,  $k_r$ ,  $k_l$ ,  $V_0^{(k)}$  and  $\Delta\phi_k$  all depend on the mode frequency  $\omega_k$ . This system has four parameters  $C_{r,l}$  and  $L_{r,l}$  and three unknowns. It is solved numerically by selecting the desired line capacitance and inductance and searching for  $(V_0^{(k)}, \Delta\phi_k, \omega_k)$  triplets. As example, three consecutive modes close to  $\omega_{\text{IR}}$ , supported by a  $50 \Omega$  CTL with  $c_r = 1667 \text{ fF}/\mu\text{m}$ ,

$l_r = 4167$  pH/ $\mu\text{m}$ ,  $C_l = 398$  fF and  $L_l = 995$  pH are shown in Fig. 7.3(a). The voltage at the unit cells is indicated by black dots and the coloured lines are to help visualise the modes. The LH TL is made of 200 cells and the RH TL is 3 cm long. The values for the capacitance and inductance were chosen so that the IR cut-off is at 4 GHz. Due to the hybrid nature of this new CTL, the closely spaced frequencies at this lower band-edge have nearly-identical spatial structures in the RH TL. The fast oscillation in the LH TL ensures orthogonality between modes. The density of modes is obtained by numerically finding all the normal modes. A key unusual feature of the LH TL, as compared to a regular RH TL, is the divergence of the density of modes (DoM) at a low-frequency bound  $\omega_{\text{IR}} = 1/2\sqrt{C_l L_l}$ , seen in Fig. 7.3(b), implying the existence of a quasi-continuous band even in a cavity. In the LH TL, low frequencies correspond to short wavelengths due to the falling dispersion relation  $\omega(k)$ . Thus, by only a small change in frequency, a new orthogonal mode can be found that is different by one node in the left-handed component. As the wavelength approaches the lattice constant, the dispersion relation in Eq. (7.4) becomes flat due to Bragg reflection [174] — the DoM develops a van-Hove-type singularity setting the aforementioned divergence at  $\omega_{\text{IR}}$ . Close to  $\omega_{\text{IR}}$  the RH TL provides a mere constant contribution thus the DoM is dominated by the divergence due to the LH TL and vice versa. In consequence, the DoM can be approximated by the sum of the densities in the uncoupled lines

$$\mathcal{D}(\omega) = \frac{4N_l\sqrt{C_l L_l}}{\pi} \tan \phi_L \sin \phi_L, \quad \phi_L = \frac{k_l(\omega)\Delta x}{2}. \quad (7.11)$$

$N_l$  is the number of cells in the LH TL. The agreement between this prediction and the numerically obtained modes of the full model is excellent up to small oscillations, see Fig. 7.3. To engineer the DoM, one can control  $\omega_{\text{IR}}$  by the mesh size and independently  $N_l$  by the length of the LH TL.

To provide good coupling between both components one would like to have an impedance  $Z_0$  (typically 50  $\Omega$ ) requiring  $C_l = (2\omega_{\text{IR}}Z_0)^{-1}$  and  $L_l = Z_0/2\omega_{\text{IR}}$ . Furthermore for coupling to qubits,  $\omega_{\text{IR}}$  should be chosen to lie around qubit frequencies (e.g. 4 GHz). The capacitances could be realised with interdigitated as well as with overlap capacitors and the parallel inductors could be realised with Josephson Junctions in the linear regime since they provide sufficient inductance in a small footprint.

## Disorder

Disorder in the LH TL has little effect on the DoM. This is shown as follows. The capacitance and inductance of unit cell  $n$  in the LH TL are assumed to

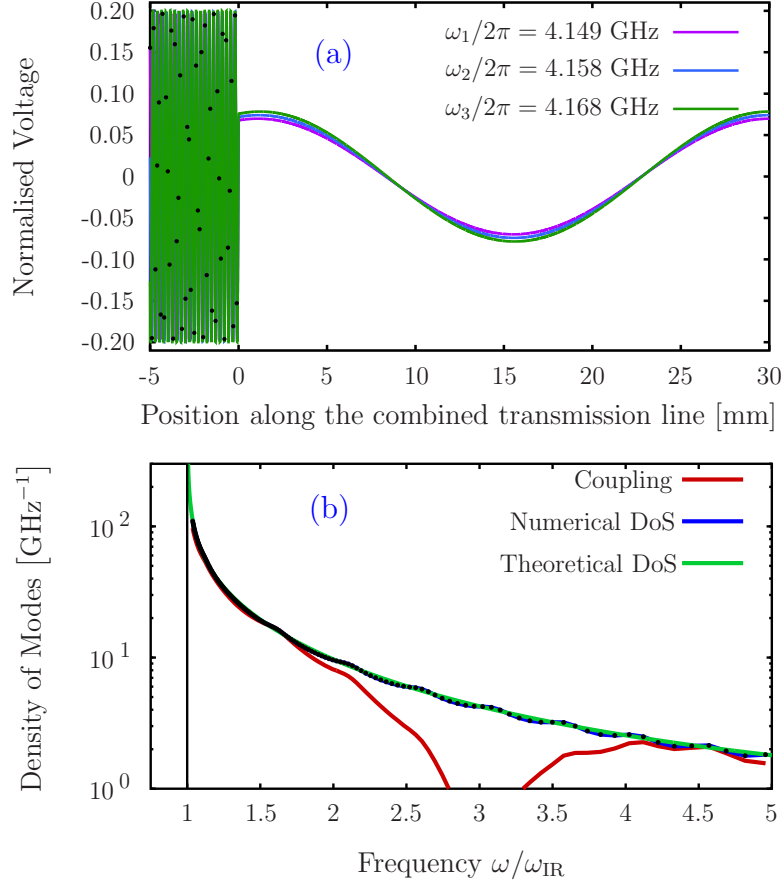


Figure 7.3: (a) Example of the first three consecutive normal modes, the voltage profiles in the RHTL are almost identical. The LHTL has 200 unit cells measuring  $100 \mu\text{m}$  each. In the LHTL the voltages at the discrete unit cells, for the first mode only, are shown by the black dots; the continuous lines serve as a guide to the eye to see the mode structure. Requiring a  $50 \Omega$  impedance and an IR cut-off at  $\omega_{\text{IR}}/2\pi = 4$  GHz sets  $C_l = 398$  fF and  $L_l = 995$  pH. The parameters for the RHTL were chosen so that it supports a full wavelength at  $\omega_{\text{IR}}$ . This sets the values for its total inductance and capacitance. Therefore a 3 cm long RHTL requires a capacitance and inductance per unit length of  $c_r = 1667$  fF/ $\mu\text{m}$  and  $l_r = 4167$  pH/ $\mu\text{m}$ . (b) Example of density of modes, showing a lower band-edge at  $\omega_{\text{IR}}$ . Dots indicate actual modes, the green curve the approximate formula which is in excellent agreement. The red curve shows the coupling strength between a 0.5 mm long flux qubit placed at a current anti-node of the transmission line, as in Fig. 7.1. Designing the qubit to couple to the 4.579 GHz mode with strength 460 MHz, results in ultrastrong-coupling to 50 modes within a  $\pm 460$  MHz range.

be  $C_l + \delta C_{l,n}$  and  $L_l + \delta L_{l,n}$  respectively. In the LHTL the plane wave Ansatz is no longer valid but serves as a starting point for perturbation theory. The frequency of mode  $k$  is perturbed by  $\delta\omega_k$  and its flux at each cell in the LHTL is  $\Phi_n^{(k)} + \delta\Phi_n^{(k)}$ . The equation of motion (7.2) has to be modified so that  $C_l$  and  $L_l$  depend on  $n$ . This results in a set of  $N_l$  equations, one for each unit cell in the LHTL. We simplify it by neglecting all second order terms of the form  $\delta C_{l,n}\delta\Phi_n^{(k)}$ , etc... This yields the matrix equation

$$\mathcal{M}\delta\Phi^{(k)} = \mathcal{B}\Phi^{(k)} + 4\sqrt{\frac{C_l}{L_l}} \sin\left(\frac{k_l(\omega_k)}{2}\right) \delta\omega_k \Phi^{(k)}, \quad (7.12)$$

where  $\Phi^{(k)} = (\Phi_0^{(k)}, \dots, \Phi_{-N_l}^{(k)})^T$  is the vector of unperturbed fluxes in the LHTL and  $\delta\Phi^{(k)} = (\delta\Phi_0^{(k)}, \dots, \delta\Phi_{-N_l}^{(k)})^T$  is the perturbation resulting from the disorder. The matrix  $\mathcal{M}$  is tridiagonal with  $L_l^{-1} - 2C_l\omega_k^2$  on the diagonal and  $\omega_k^2 C_l$  on the lower and upper diagonal. The matrix  $\mathcal{B}$  contains the disorder terms and is also tridiagonal with  $\delta L_{l,n}/L_l^2 + \omega_k^2(\delta C_{l,n} + \delta C_{l,n-1})$  on the diagonal,  $-\omega_k^2\delta C_{l,n-1}$  on the lower diagonal and  $-\omega_k^2\delta C_{l,n}$  on the upper diagonal. The flux at the interface, i.e.  $\Phi_0^{(k)} + \delta\Phi_0$ , is matched for both lines. This condition yields  $\delta\omega$  since in the RHTL the plane wave with frequency  $\omega_k + \delta\omega_k$  should have charge neutral boundary conditions, i.e.  $|\theta_{N_r,k}| = 0$ . With the flux at the interface known, Eq. (7.12) can be solved for the remaining  $\delta\Phi_n^{(k)}$  by computing the inverse of  $\mathcal{M}$ . An example of a DoM with disorder is shown in Fig. 7.4, the sharp rise in the DoM close to the IR cut-off remains but with fluctuations. This guarantees that disorder does not affect the mode pile-up at low frequencies. Furthermore since qubits are to be coupled to the RHTL, where small frequency shifts have little effect on the mode profile, the system is robust against disorder. An example of a perturbed mode close to  $\omega_{\text{IR}}$  is shown in Fig. 7.5.

Figure 7.4: Perturbed density of modes. The random variables  $\delta C_{l,n}$  and  $\delta L_{l,n}$  are chosen to be Gaussian with a zero mean and standard deviation of  $0.05C_l$  and  $0.1L_l$ . As can be seen, the perturbed DoM follows the unperturbed one but with some fluctuations. The black dots are the numerically found modes of Fig. 7.3 without disorder.

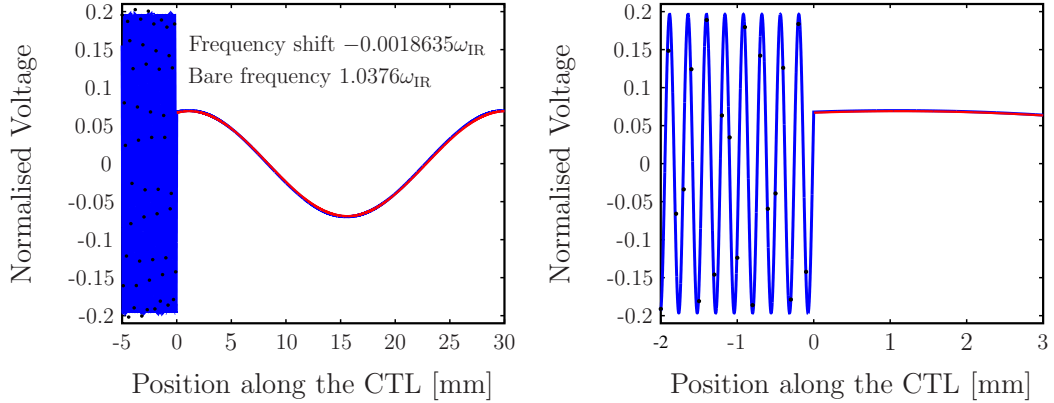
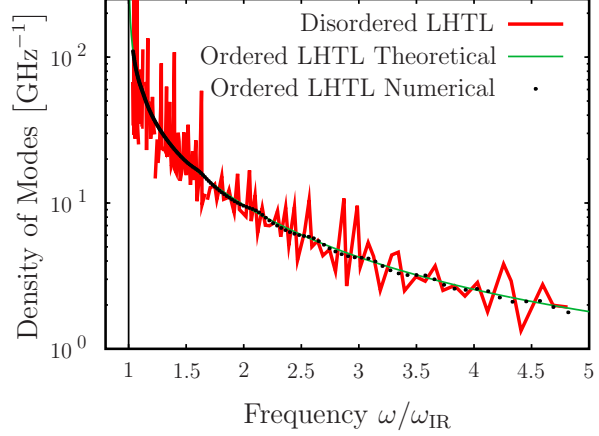


Figure 7.5: Voltage profile of a mode close to  $\omega_{\text{IR}}$ . The blue line is the unperturbed plane wave ansatz. Although the LHTL is not continuous, the line serves as a guide to the eye. The red line is the voltage profile in the RHTL when taking disorder in the LHTL into account. The black dots show the voltage in the disordered LHTL. As can be seen the black dots no longer align perfectly with the unperturbed mode.

## 7.2 Applications

The quantum behaviour of the CTL is obtained through canonical quantisation of the circuit in Fig. 7.1. This leads to a system of uncoupled quantum harmonic oscillators, each described by operators  $\hat{a}_n^\dagger, \hat{a}_n$  acting on modes with frequencies  $\omega_n$ . A qubit described in its energy eigenbasis by Pauli matrices  $\hat{\sigma}_{x/z}$  placed close to the CTL will couple to mode  $n$  with strength  $g_n$

$$\hat{H}/\hbar = \frac{\Delta_0}{2} \hat{\sigma}_z + \sum_n g_n \hat{\sigma}_x (\hat{a}_n + \hat{a}_n^\dagger) + \sum_n \omega_n \hat{a}_n^\dagger \hat{a}_n. \quad (7.13)$$

If the qubit is coupled to the RHTL,  $g_n \simeq g_{n+1}$  for low frequency modes since they have similar spatial profiles in the RHTL. For a flux qubit [19, 29], the mode dependent part of the coupling strength is given by taking into account the finite size of the qubit and the spacial profile of the mode. It is given by  $\mathcal{D}(\omega_n) \langle I_n(x) \rangle / \max_n \{ \langle I_n(x) \rangle \}$ . The current  $I_n$  is averaged over the spatial extent of the qubit. Figure 7.3 shows that the qubit can be coupled to a wide range of modes. For frequencies sufficiently above  $\omega_{IR}$  the wavelength in the RHTL also starts to change away from the antinode towards a node, creating a deep minimum in coupling strength. This mode structure allows the qubit to simultaneously couple to multiple modes when  $N > 1$  modes fall within a frequency interval of  $2g_n$ . We refer to this regime as *multi-mode strong-coupling*. It can be reached with other superconducting qubits, notably transmons [33], which should be placed at a charge antinode. Flux qubits on the other hand allow us to reach *multi-mode ultrastrong coupling* [155, 156] —  $g_n/\omega_n > 0.1$ . This regime offers many new possibilities for circuit QED.

### 7.2.1 Multi-Mode Entanglement

The multi-mode Rabi Hamiltonian, Eq. (7.13), allows us to prepare multi-mode entangled states. Within the rotating wave approximation it conserves the number of excitations. Exciting the qubit and placing its  $0 \leftrightarrow 1$  resonance frequency slightly above  $\omega_{IR}$  allows the qubit excitation to distribute itself over many modes, i.e., produce arbitrary superpositions of the form  $c_0 |1; 0\rangle + \sum_n c_n |0; n\rangle$ .  $|0; n\rangle$  indicates the qubit in the ground state, a single photon in mode  $n$  and none in the other modes. For  $|1; 0\rangle$  only the qubit is excited. These states are in general entangled as seen from their Von Neumann entropy [175]. The qubit is put in the bath at a frequency  $\omega_q > \omega_{IR}$  and the system left to evolve for a dimensionless time  $tg$ . The Von Neumann entropy is computed for the system after having traced out the qubit and mode  $n$ , see Fig. 7.6. It indicates complex multi-partite entanglement.

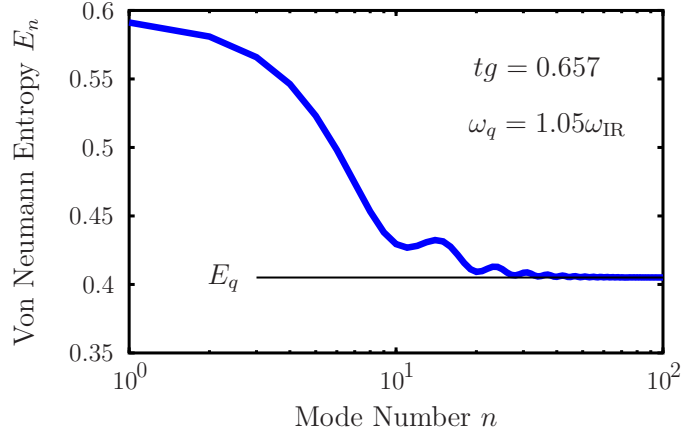


Figure 7.6: Von Neumann entropy as function of the traced out mode  $n$ . We then vary  $n$  to see how much the entropy increases from  $E_q$ , the entropy when only the qubit is traced out.  $E_q > 0$  indicates that there is at least bi-partite entanglement. When additionally tracing out mode  $n$  the entropy  $E_n$  increases above  $E_q$  and this is for all modes indicating complex multi-partite entanglement.

### 7.2.2 Spin-Boson Simulator

The Spin-Boson model [170] is a fundamental model of quantum dissipation which allows to understand the transition between coherent and incoherent behaviour as well as a quantum phase transition suppressing quantum tunnelling. It is described by the Hamiltonian in Eq. (7.13) in the limit where the modes form a continuum. The dense modes at the low-frequency end provide a generic and realisable quantum simulator for this model. Our unusual density of modes provides a novel regime of sub-subhomic models with a low-frequency cut-off, i.e., a spectral density of the form

$$J(\omega) = \sum_n g_n^2 \delta(\omega - \omega_n) \simeq \frac{N_l}{\pi \sqrt{2\omega_{\text{IR}}}} \frac{\Theta(\omega - \omega_{\text{IR}})}{\sqrt{\omega - \omega_{\text{IR}}}}.$$

The ground and lowest excited states are well approximated by a multimode Schrödinger cat state of the qubit dressed by coherent photonic states [170]

$$|\pm\rangle = \frac{1}{\sqrt{2}} \left( |L\rangle \bigotimes_n |\lambda_n\rangle \pm |R\rangle \bigotimes_n |-\lambda_n\rangle \right). \quad (7.14)$$

$|L, R\rangle$  are the eigenstates of  $\hat{\sigma}_x$ . The renormalised energy splitting is

$$\Delta_{\text{eff}} = \langle + | \hat{H} | - \rangle = \Delta_0 \exp \left( -2 \sum_n \lambda_n^2 \right). \quad (7.15)$$

The multimode cat state in Eq. (7.14) involves, according to the principle of adiabatic renormalisation, all fast modes, those with  $\omega_n > \Delta_{\text{eff}}$ , as they can adiabatically follow the qubit. Slow modes remain unaffected. Thus  $\lambda_n = \frac{g_n}{\omega_n} \Theta(\omega_n - \Delta_{\text{eff}})$  which leads to a self-consistency relation for  $\Delta_{\text{eff}}$ . The ratio  $\Delta_{\text{eff}}/\Delta_0$  measures the accumulated phase space distance of the dressing clouds, i.e. the total cat size [153], by taking the logarithm of equation (7.15). Thus, the low-energy states of the system are strongly renormalised as are their effective energies.

A true dissipative quantum phase transition [138, 170] has  $\Delta_{\text{eff}} = 0$  in the localised phase. This limit would be reached if the modes were infinitely close (hence arbitrarily close to  $\omega_{\text{IR}}$ ) as would result from an infinitely long LHTL or if  $\omega_{\text{IR}} \rightarrow 0$  as in the case of infinitely dense LHTL unit cells. Note that in the usual sub-Ohmic spin-boson model, the latter is assumed. We thus conclude that our system approaches a quantum phase transition in the infinite sample limit.

To corroborate the finite size-behaviour, we have studied the ground and first excited state of the qubit-CTL model using its actual modes in the adiabatic renormalisation approach. We identify multiple regimes: for weak coupling or large  $\Delta_0/\omega_{\text{IR}}$ , there is only weak dressing manifest by a small shift of  $\Delta_0$ . At stronger coupling, we observe the quasi-localised phase, with  $\Delta_{\text{eff}} \ll \Delta_0$ . Remarkably, even at finite length, the two regimes are separated by a discontinuous transition as indicated by Figure 7.7. Figure 7.8 shows the corresponding finite-size phase diagram highlighting the need for ultrastrong coupling. We see that by tuning the bare qubit frequency slightly above the cut-off,  $\Delta_0 > \omega_{\text{IR}}$  [176] we can tune the system through the phase transition *in situ*, or by employing a tunable coupler. The phase transition is manifest by a discontinuous drop in the energy splitting (as measured through spectroscopy) of the qubit that is inconsistent with the tuning of the circuit alone, see Fig. 7.7. Engineering the transmission line to have dense enough modes and an appropriate  $\omega_{\text{IR}}$  can be accomplished using Eq. (7.11) and  $\omega_{\text{IR}} = 1/2\sqrt{C_l L_l}$ .

### Approaching a quantum phase transition

On the level of partition functions, this model is equivalent to a one-dimensional Ising chain [138, 177]. A true quantum phase transition i.e.  $\Delta_{\text{eff}} = 0$  is reached only in an infinitely dense LHTL. Showing that the qubit-CTL system approaches a quantum phase transition up to finite size effects, is done by making use of the map between the Spin-Boson model and the 1D Ising chain [177]. This makes use of the Feynman-Vernon influence functional [178]. Following the reasoning in Weiss [138] the partition functions of these

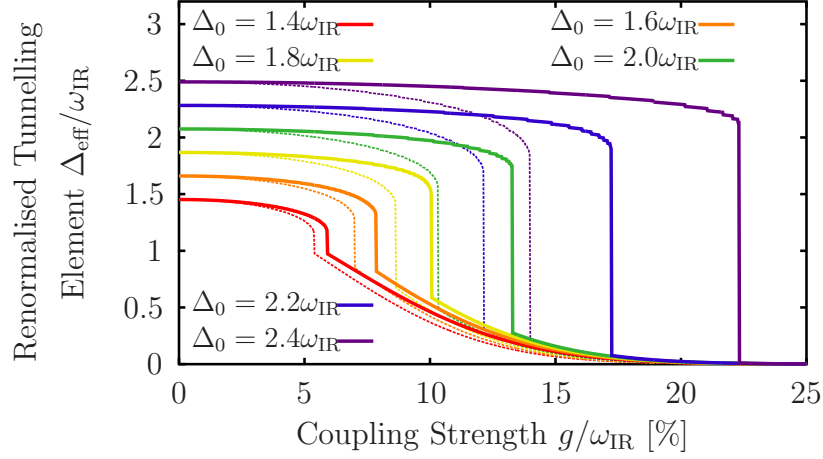


Figure 7.7: Plot of the renormalised tunnelling as function of the global coupling strength  $g$ . The individual mode coupling  $g_n$  is the product of  $g$  and the mode-dependent spatial contribution bounded by unity. The thin dashed lines correspond to the case when this effect is neglected i.e.  $\langle I_n(x) \rangle / \max_n \{ \langle I_n(x) \rangle \} = 1$ . This allows simultaneous tuning of the coupling to all modes. The discontinuous drop in  $\Delta_{\text{eff}}$  distinguishes the regions of weakly and strongly renormalised energy splitting.

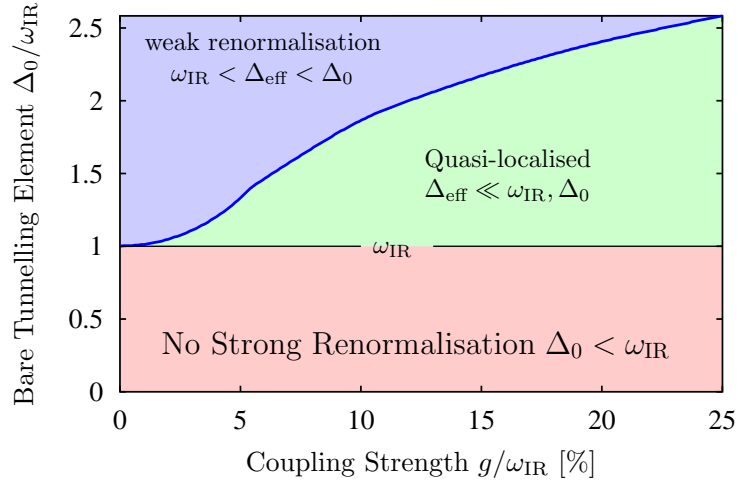


Figure 7.8: Finite-size phase diagram of the qubit-CTL system. The density of states for the case at hand is the same as in Fig. 7.3 with the dip in coupling taken into account.

models are expressed as sums over the number  $m$  of kinks

$$\begin{aligned}
Z_{\text{sb}} &= \sum_{\pm q_0} \sum_{m=0}^{\infty} \left(\frac{\Delta_0}{2}\right)^{2m} \int_0^{\infty} ds_{2m} \int_0^{s_{2m}} ds_{2m-1} \dots \int_0^{s_2} ds_1 \\
&\quad \times \exp \left\{ \sum_{j=2}^{2m} \sum_{i=1}^{j-1} (-1)^{i+j} W(s_j - s_i) \right\} \\
Z_{\text{ising}} &= \sum_{m=0}^{\infty} e^{-4m\beta U(0)} \int_0^{\hbar\beta - x_c} \frac{ds_{2m}}{x_c} \int_0^{s_{2m} - x_c} \frac{ds_{2m-1}}{x_c} \dots \int_0^{s_2 - x_c} \frac{ds_1}{x_c} \\
&\quad \times \exp \left\{ 4 \sum_{j=2}^{2m} \sum_{i=1}^{j-1} (-1)^{j+i} U[(s_j - s_i)/x_c] \right\}
\end{aligned}$$

In the flux qubit-CTL system a kink corresponds to the system tunnelling from one side of the potential well to the other. These tunnelling events take place a times  $s_j$ . In the 1D Ising chain a kink corresponds to a spin domain wall at location  $s_j$ . By comparing the two partition functions, it is seen that the second integral of the Ising interaction potential  $U$  plays that same role as the kink-kink interaction of the Spin-Boson model  $W(r)$ . Therefore the quantity  $\partial_\tau^2 W(\tau)$  is equivalent to the interaction potential of the Ising model. Using the definition of  $W$  found in Weiss [138] gives

$$\begin{aligned}
V(\tau) &= \partial_\tau^2 W(\tau) = \alpha \partial_\tau^2 \int_0^{\infty} d\omega \frac{\mathcal{D}(\omega)}{\omega^2} (1 - e^{-\omega\tau}) \\
&= \frac{\alpha N_l}{\sqrt{2\omega_{\text{IR}}\pi}} \partial_\tau^2 \int_{\omega_{\text{IR}}}^{\infty} d\omega \frac{1 - e^{-\omega\tau}}{\omega^2 \sqrt{\omega - \omega_{\text{IR}}}} = -\frac{\alpha N_l}{\sqrt{2\omega_{\text{IR}}\pi}} \sqrt{\frac{\pi}{\tau}} e^{-\omega_{\text{IR}}\tau}.
\end{aligned}$$

The constant  $\alpha$  includes all the dependencies of qubit-CTL coupling. An example of which can be found in [155]. Here the density of states was approximated by the  $\omega^{-1/2}$  law valid close to the IR cut-off. In the present case, this would be an Ising chain with an interaction that decays as  $\propto |i-j|^{-1/2}$ , where  $i$  and  $j$  are site indices, up to a range  $r \propto \omega_{\text{IR}}^{-1}$ , after which it decays exponentially. Thus, when cooled from high-temperatures the system is well described by mean-field theory, which predicts a ferromagnetic phase transition, until the correlation length reaches  $r$ . At that point, the system follows short-range physics and remains paramagnetic between magnetised blocks of size  $r$  — in analogy to the tunnel coupling in the spin-boson model falling deeply, but not to zero.

### 7.3 Conclusions

We have proposed an engineered hybrid transmission line that allows to reach a new multimode strong coupling regime of circuit QED by combining a regular line with a metamaterial. This will open the way for novel applications in microwave photonics and strongly correlated photon states, out of which we have outlined the generation of multimode entanglement, multimode Schrödinger cat states and quantum phase transitions. This system serves as an analogue quantum simulator for the Spin-Boson model up to finite size effects due to the mode discreteness.

# Conclusion

At the time of writing, coherent quantum control has been demonstrated with up to five superconducting qubits. These experiments have shown impressive single and multi-qubit control with gate fidelities reaching the threshold where surface codes become useful. However, whether a quantum computer will be built remains an open question. The scaling up towards a useful quantum computer will be an immense challenge. Many engineering issues need to be addressed. Dedicated control and readout electronics need to be further developed so as to miniaturise the classical hardware supporting the quantum chips. The gate and measurement fidelities need to increase. Indeed the higher these are the less overhead is needed to perform error correction/detection. Up to date, the control pulses for superconducting qubits are developed analytically using simple models. This makes calibrating such pulses easy. However they are not optimal; they can lose fidelity through leakage or by being too slow, thus making the effect of decoherence larger than should be. A substantial improvement in control software is to be expected by using methods from optimal control theory. This work has been carried out with the intention to make optimal control viable for superconducting qubits as well as illustrating its many benefits.

We have shown in chapter 3 how spectral crowding, a scaling issue arising when trying to pack more qubits in the same spectral range, can be mitigated through careful analytical considerations. This is done using average Hamiltonian theory, i.e. the zeroth order term of the Magnus expansion. The resulting pulses are the common DRAG solution with an extra modulation. We named these pulses Wah-Wah for weak anharmonicity with average Hamiltonian. Then in chapter 4 we show the full power of optimal control. The control pulse of the previous chapter is made faster and more accurate. Then we considered a more complex system, namely two qubits coupled through a bus resonator. The studied time evolution was the entangling controlled-Z gate. We showed that optimal control is capable of yielding a substantial improvement over analytically derived pulses. Optimal control can create pulses with perfect fidelity whilst reaching the shortest gate time allowed by

the system's quantum speed limit. This is paramount to a quantum computer since error detection/correction codes perform many entangling gates. Making these gates as fast as the quantum speed limit allows is crucial to the timely execution of a quantum algorithm. However, having perfect gates is meaningless if the state of the qubits cannot be measured with meaningful accuracy. There are many different ways to measure qubits. In chapter 5 we considered the phase qubit and the Josephson photomultiplier. The measurement contrast was optimised by shaping the bias pulse with a gradient search. This required a modification of the GRAPE algorithm since this type of measurement is a non-unitary process. We showed that a fast measurement pulse, slightly above 1 ns, can produce high contrasts. Chapter 6 on optimal control theory shows how to overcome the last obstacle in the practical implementation of numerical pulses. Despite their obvious advantages they have not been implemented in superconducting qubits. Their complex shape is the main reason. This prevents a manual tune-up of the pulses to the qubit chip. Indeed the models used to design the pulses are only an approximation of the physical system. It is thus not surprising that open-loop pulse design fails. We showed that the Ad-HOC protocol overcomes these pulse tune-up issues using open and closed-loop pulse design. This allows for a necessary automated pulse tune-up. Indeed even for few parameter pulses, where manual tune-up is still possible with a few qubits, it will no longer be the case as the number of qubits grows. Furthermore this protocol is applicable to any quantum control experiment, thus extending its usefulness far beyond the realm of superconducting qubits.

Numerical pulses will no doubt be implemented in superconducting qubit architectures. Future work should include and experimental demonstration of their feasibility. Furthermore boundary effects in arrays of coupled qubits need to be studied. For example, how does one make a quantum gate between two qubits without affecting the others in a surface code architecture? How many qubits should such a simulation include? One could also envisage making a quantum compiler based on optimal control whereby a full quantum circuit is compiled into a time and fidelity optimal numerical pulse sequence.

Lastly chapter 7 of this thesis proposes a system to bring circuit QED to the novel regime of multi-mode ultra-strong coupling. This is done by combining left- and right-handed transmission lines. This system has a mode pile-up at an infra-red cut-off creating almost identical modes in the right-handed transmission line. A superconducting qubit is then coupled to these modes. We showed how this system generates highly non-classical states. Furthermore it can be used as an analogue simulator for the Spin-Boson model in a regime where a quantum phase transition between a quasi-localised and a delocalised state occurs. This is an important effect showing how an envi-

ronment, the transmission line, causes the quantum analogue of friction on the two level system, the qubit.

Quantum technologies are still a long way from exploiting their full potential. At the time of writing, the much anticipated quantum computer is still a technology of the future. It is unclear if all the technological challenges to build such a computer will be overcome. Furthermore there is a big gap between the current proof of principle experiments involving a few qubits and the complete quantum computer involving millions of qubits. Indeed a few hundreds of qubits would not suffice for an error correction/detection code to factor a useful number. However it is in this system size gap where quantum simulations might provide an intellectually stimulating framework for research to continue in academia whilst engineering challenges are addressed by research laboratories, universities and industry.

# Publication List

## Published

- D. J. Egger and F. K. Wilhelm  
*Adaptive hybrid optimal quantum control for imprecisely characterized systems*  
Phys. Rev. Lett. **112**, 240503 (2014)
- D. J. Egger and F. K. Wilhelm  
*Optimized controlled-Z gates for two superconducting qubits coupled through a resonator*  
Supercond. Sci. Technol. **27**, 014001 (2014)
- R. Schutjens, F. Abu Dagga, D. J. Egger and F. K. Wilhelm  
*Single-qubit gates in frequency-crowded transmon systems*  
Phys. Rev. A **88**, 052330 (2013)
- D. J. Egger and F. K. Wilhelm  
*Multimode Circuit Quantum Electrodynamics with Hybrid Metamaterial Transmission Lines*  
Phys. Rev. Lett. **111**, 163601 (2013)

## Accepted in Phys. Rev. A

- D. J. Egger and F. K. Wilhelm  
*Optimal Control of Quantum Measurement*  
arXiv:1408.6086

## Previous Publications

- M. Ovegård, E. Adli, H. H. Braun, E. Bravin, N. Chritin, R. Corsini, A. E. Dabrowski, S. Dobert, C. Dutriat, D. Egger, T. Lefevre, O. Mete, P. K. Skowronski and F. Tecker  
*High intensity profile monitor for time resolved spectrometry at the CLIC Test Facility 3*  
Nucl. Instr. Meth. Phys. Res. A **683**, 29 (2012)
- O. Mete, E. Chevallay, M. Csatari, A. Dabrowski, S. Doebert, D. Egger, V. Fedosseev, M. Olvegaard and M. Petrarca  
*Production of long bunch trains with 4.5  $\mu\text{C}$  total charge using a photoinjector*  
Phys. Rev. STAB **15**, 022803 (2012)
- A. E. Dabrowski, S. Bettoni, E. Bravin, R. Corsini, S. Doebert, T. Lefevre, A. Rabiller, L. Soby, P. K. Skowronski, F. Tecker, D. Egger, A. Ferrari and C. P. Welsch  
*Measuring the bunch frequency multiplication at the 3rd CLIC Test Facility*  
JINST **7**, P01005 (2012)
- E Chevallay, M. Csatari, A. Dabrowski, S. Doebert, D. Egger, V. Fedosseev, O. Mete, M. Ovegård and M. Petrarca  
*PHIN photo-injector as the CLIC drive beam source*  
Journal of Physics: Conference Series **347**, 012036 (2012)



# Appendix A

## Phase Qubit Potential

The Hamiltonian of the flux biased phase qubit is

$$\hat{H} = E_c \hat{N}^2 + E_J \underbrace{\left( \frac{1}{2\beta} (\hat{\varphi} - \varphi_b)^2 - \cos \hat{\varphi} \right)}_{V_J \text{ qubit potential}}.$$

This Hamiltonian can be approximated by a third order potential  $\hat{V}_3$  with three parameters  $m$ ,  $\omega$  and  $\tilde{\varphi}$ . The approximate Hamiltonian is given by

$$\hat{H}' = \frac{\hbar^2}{2m} \hat{N}^2 + \frac{1}{2} m \omega^2 \Delta\varphi^2 \left( 1 - \frac{2}{3} \frac{\Delta\varphi}{\tilde{\varphi}} \right).$$

The phase variable is  $\Delta\varphi = \varphi - \varphi_{\min}$  where  $\varphi_{\min}$  is the local minimum of the shallow well. By comparing  $\hat{H}$  and  $\hat{H}'$  it is straight forward to identify the effective mass as  $m = \hbar^2/2E_c$ . Note that this parameter has units of energy instead of mass. In this approximation the constant term in the potential has been dropped so that  $V_3(\Delta\varphi = 0) = 0$ . The frequency  $\omega$  in the third order potential is chosen such that the harmonic term matches the second derivative of the actual phase qubit potential

$$\frac{1}{2} V_J''(\varphi_{\min}) = \frac{1}{2} m \omega^2 \implies \hbar\omega = \sqrt{2E_c E_J (\beta^{-1} + \cos \varphi_{\min})}. \quad (\text{A.1})$$

Lastly,  $\tilde{\varphi}$  is determined so that the potential barrier has the right height. This imposes  $V_3(\Delta\varphi = \tilde{\varphi}) = V_{\max} - V_{\min}$  where  $V_{\min/\max}$  are the local minima/maxima close to the shallow well, see Fig. 5.1. This leads to the following expression

$$m\omega^2 \tilde{\varphi} = 6(V_{\max} - V_{\min}). \quad (\text{A.2})$$

The tunnelling rates given in chapter 12 of Weiss [138] for the potential  $V_3$  involve the term  $m\omega^2\tilde{\varphi}^2/\hbar\omega$  which, for brevity, was labelled  $\alpha$  in chapter 5. Therefore, combining Eqs. (A.1) and (A.2) yields

$$\alpha = 6 \frac{V_{\max} - V_{\min}}{\sqrt{2E_J E_c}(\beta^{-1} + \cos \varphi_{\min})}.$$

# Bibliography

- [1] M. A. Nielsen and I. L. Chuang. *Quantum Computing and Quantum Information*. Cambridge University Press, 2000.
- [2] G. Vidal and C. M. Dawson. Universal quantum circuit for two-qubit transformations with three controlled-not gates. *Phys. Rev. A*, 69(1):010301, 2004.
- [3] Y. Makhlin. Nonlocal properties of two-qubit gates and mixed states, and the optimization of quantum computations. *Quantum Inf. Process.*, 1:243–252, 2002.
- [4] J. Zhang, J. Vala, S. Sastry, and K. B. Whaley. Geometric theory of nonlocal two-qubit operations. *Phys. Rev. A*, 67:042313, 2003.
- [5] S. J. Lomonaco, editor. *Quantum Information Science and Its Contributions to Mathematics*. American Mathematical Society, 2010.
- [6] S. Aaronson and D. Gottesman. Improved simulation of stabilizer circuits. *Phys. Rev. A*, 70:052328, 2004.
- [7] Y.-A. Chen, S. Chen, Z.-S. Yuan, B. Zhao, C.-S. Chuu, J. Schmiedmayer, and J.-W. Pan. Memory-built-in quantum teleportation with photonic and atomic qubits. *Nat. Phys.*, 4:103–107, 2008.
- [8] P. Kok, W. J. Munro, K. Nemoto, T. C. Ralph, J. P. Dowling, and G. J. Milburn. Linear optical quantum computing with photonic qubits. *Rev. Mod. Phys.*, 79:135–174, 2007.
- [9] J. I. Cirac and P. Zoller. A scalable quantum computer with ions in an array of microtraps. *Nature*, 404:579–581, 2000.
- [10] J. I. Cirac and P. Zoller. Quantum computations with cold trapped ions. *Phys. Rev. Lett.*, 74:4091, 1995.

- [11] T. Monz, P. Schindler, J. T. Barreiro, M. Chwalla, D. Nigg, W. A. Coish, M. Harlander, W. Hänsel, M. Hennrich, and R. Blatt. 14-qubit entanglement: Creation and coherence. *Phys. Rev. Lett.*, 106:130506, 2011.
- [12] I. Bloch. Ultracold quantum gases in optical lattices. *Nat. Phys.*, 1:23, 2005.
- [13] G. K. Brennen, C. M. Caves, P. S. Jessen, and I. H. Deutsch. Quantum logic gates in optical lattices. *Phys. Rev. Lett.*, 82:1060–1063, 1999.
- [14] D. Jaksch, H.-J. Briegel, J. I. Cirac, C. W. Gardiner, and P. Zoller. Entanglement of atoms via cold controlled collisions. *Phys. Rev. Lett.*, 82:1975, 1999.
- [15] D. Loss and D. P. DiVincenzo. Quantum computation with quantum dots. *Phys. Rev. A*, 57:120–126, 1998.
- [16] L. Robledo, L. Childress, H. Bernien, B. Hensen, P. F. A. Alkemade, and R. Hanson. High-fidelity projective read-out of a solid-state spin quantum register. *Nature*, 477:574–578, 2011.
- [17] M. Leifgen, T. Schröder, F. Gädeke, R. Riemann, V. Métilon, E. Neu, C. Hepp, C. Arend, C. Becher, K. Lauritsen, and O. Benson. Evaluation of nitrogen- and silicon-vacancy defect centres as single photon sources in quantum key distribution. *New. J. Phys.*, 16:023021, 2014.
- [18] C. Hepp, T. Müller, V. Waselowski, J. N. Becker, B. Pingault, H. Sternschulte, D. Steinmüller-Nethl, A. Gali, J. R. Maze, M. Atatüre, and C. Becher. Electronic structure of the silicon vacancy color center in diamond. *Phys. Rev. Lett.*, 112:036405, 2014.
- [19] J. Clarke and F. K. Wilhelm. Superconducting quantum bits. *Nature*, 453:1031–1042, 2008.
- [20] R. J. Schoelkopf and S. M. Girvin. Wiring up quantum systems. *Nature*, 451:664–669, 2008.
- [21] Y. Makhlin, G. Schön, and A. Shnirman. Quantum-state engineering with josephson-junction devices. *Rev. Mod. Phys.*, 73:357, 2001.
- [22] M. H. Devoret and J. M. Martinis. Implementing qubits with superconducting integrated circuits. *Quantum Information Processing*, 3:163–203, 2004.

- [23] M.H. Devoret and R.J. Schoelkopf. Superconducting circuits for quantum information: An outlook. *Science*, 339:1169, 2013.
- [24] F. Dalfovo, S. Giorgini, L. P. Pitaevskii, and S. Stringari. Theory of bose-einstein condensation in trapped gases. *Rev. Mod. Phys.*, 71:463–512, 1999.
- [25] J.M. Martinis, S. Nam, J. Aumentado, and C. Urbina. Rabi oscillations in a large josephson-junction qubit. *Phys. Rev. Lett.*, 89(11):117901, 2002.
- [26] B. Yurke and J. S. Denker. Quantum network theory. *Phys. Rev. A*, 29:1419, 1984.
- [27] J. M. Martinis, M. H. Devoret, and John Clarke. Energy-level quantization in the zero-voltage state of a current-biased josephson junction. *Phys. Rev. Lett.*, 55:1543, 1985.
- [28] J. M. Martinis, M. H. Devoret, and J. Clarke. Experimental tests for the quantum behavior of a macroscopic degree of freedom: The phase difference across a josephson junction. *Phys. Rev. B*, 35:4682–4698, 1987.
- [29] J. E. Mooij, T. P. Orlando, L. Levitov, L. Tian, C. H. van der Wal, and S. Lloyd. Josephson persistent-current qubit. *Science*, 285:1036, 1999.
- [30] V. Bouchiat, D. Vion, P. Joyez, D. Esteve, and M. H. Devoret. Quantum coherence with a single cooper pair. *Physica Scripta*, T76:165, 1998.
- [31] Y. Nakamura, Y.A. Pashkin, and J.S. Tsai. Coherent control of macroscopic quantum states in a single-Cooper-pair box. *Nature*, 398:786, 1999.
- [32] Y. Makhlin, G. Schön, and A. Shnirman. Josephson-junction qubits with controlled couplings. *Nature*, 398:305–307, 1999.
- [33] J. Koch, Terri M. Yu, J. M. Gambetta, A. A. Houck, D. I. Schuster, J. Majer, A. Blais, M. H. Devoret, S. M. Girvin, and R. J. Schoelkopf. Charge-insensitive qubit design derived from the cooper pair box. *Phys. Rev. A*, 76:042319, 2007.

- [34] J. A. Schreier, A. A. Houck, J. Koch, D. I. Schuster, B. R. Johnson, J. M. Chow, J. M. Gambetta, J. Majer, L. Frunzio, M. H. Devoret, S. M. Girvin, and R. J. Schoelkopf. Suppressing charge noise decoherence in superconducting charge qubits. *Phys. Rev. B*, 77:180502(R), 2008.
- [35] R. Barends, J. Kelly, A. Megrant, D. Sank, E. Jeffrey, Y. Chen, Y. Yin, B. Chiaro, J. Mutus, C. Neill, P. O'Malley, P. Roushan, J. Wenner, T. C. White, A. N. Cleland, and J. M. Martinis. Coherent josephson qubit suitable for scalable quantum integrated circuits. *Phys. Rev. Lett.*, 111:080502, 2013.
- [36] M. R. Geller, E. J. Pritchett, A. T. Sornborger, and F. K. Wilhelm. Quantum computing with superconductors i: Architectures. *NATO Science Series II: Mathematics, Physics and Chemistry*, 244:171–194, 2006.
- [37] Y. Nazarov and Y. Blanter. *Quantum Transport: Introduction to Nanoscience*. Cambridge University Press, 2009.
- [38] F. Motzoi, J. M. Gambetta, P. Rebentrost, and F. K. Wilhelm. Simple pulses for elimination of leakage in weakly nonlinear qubits. *Phys. Rev. Lett.*, 103:110509, 2009.
- [39] C. Kittel. *Introduction to Solid State Physics*. John Wiley & Sons Inc., 2005.
- [40] Y. Nakamura, Yu. A. Pashkin, T. Yamamoto, and J. S. Tsai. Charge echo in a cooper-pair box. *Phys. Rev. Lett.*, 88:047901, 2002.
- [41] D. Vion, A. Aassime, A. Cottet, P. Joyez, H. Pothier, C. Urbina, D. Esteve, and M.H. Devoret. Manipulating the quantum state of an electrical circuit. *Science*, 296:866, 2002.
- [42] P. Bertet, I. Chiorescu, G. Burkard, K. Semba, C.J.P.M. Harmans, D.P. DiVincenzo, and J.E. Mooij. Relaxation and dephasing in a flux-qubit. *Phys. Rev. Lett.*, 95:257002, 2005.
- [43] A.A. Houck, J. Koch, M.H. Devoret, S.M. Girvin, and R.J. Schoelkopf. Life after charge noise: recent results with transmon qubits. *Quant. Inf. Proc.*, 8:105, 2009.

- [44] J. Bylander, S. Gustavsson, F. Yan, F. Yoshihara, K. Harrabi, G. Fitch, D. G. Cory, Y. Nakamura, J.-S. Tsai, and W. D. Oliver. Noise spectroscopy through dynamical decoupling with a superconducting flux qubit. *Nature Physics*, 7:565–570, 2011.
- [45] H. Paik, D. I. Schuster, L. S. Bishop, G. Kirchmair, G. Catelani, A. P. Sears, B. R. Johnson, M. J. Reagor, L. Frunzio, L. I. Glazman, S. M. Girvin, M. H. Devoret, and R. J. Schoelkopf. Observation of high coherence in josephson junction qubits measured in a three-dimensional circuit qed architecture. *Phys. Rev. Lett.*, 107:240501, 2011.
- [46] N.A. Masluk, I.M. Pop, A. Kamal, Z.K. Mineev, and M.H. Devoret. Microwave characterization of josephson junction arrays: Implementing a low loss superinductance. *Phys. Rev. Lett.*, 109:137002, 2012.
- [47] F. Gaitan. *Quantum Error Correction and Fault Tolerant Quantum Computing*. Taylor & Francis Group, 2008.
- [48] A. M. Steane. Efficient fault-tolerant quantum computing. *Nature*, 399:124–126, 1999.
- [49] S. B. Bravyi and A. Y. Kitaev. Quantum codes on a lattice with boundary. arXiv:9811052v1.
- [50] E. Dennis, A. Kitaev, A. Landahl, and J. Preskill. Topological quantum memory. *J. Math. Phys.*, 43:4452, 2002.
- [51] A. G. Fowler, M. Mariantoni, J. M. Martinis, and A. N. Cleland. Surface codes: Towards practical large-scale quantum computation. *Phys. Rev. A*, 86:032324, 2012.
- [52] N. Khaneja, T. Reiss, C. Kehlet, T. Schulte-Herbrüggen, and S. J. Glaser. Optimal control of coupled spin dynamics: design of nmr pulse sequences by gradient ascent algorithms. *J. Magn. Reson.*, 172:296–305, 2005.
- [53] S.A. Rice and M. Zhao. *Optical Control of Molecular Dynamics*. Wiley, 2000.
- [54] P. Brumer and M. Shapiro. *Principles of the Quantum Control of Molecular Processes*. Wiley, 2003.
- [55] J. M. Chow, J. M. Gambetta, A. D. Córcoles, S. T. Merkel, J. A. Smolin, C. Rigetti, S. Poletto, G. A. Keefe, M. B. Rothwell, J. R.

- Rozen, M. B. Ketchen, and M. Steffen. Universal quantum gate set approaching fault-tolerant thresholds with superconducting qubits. *Phys. Rev. Lett.*, 109:060501, 2012.
- [56] R. P. Feynman. Simulating physics with computers. *International Journal of Theoretical Physics*, 21:467–488, 1982.
- [57] I. M. Georgescu, S. Ashhab, and F. Nori. Quantum simulation. *Rev. Mod. Phys.*, 86:153–185, 2014.
- [58] R. Fazio and H. van der Zant. Quantum phase transitions and vortex dynamics in superconducting networks. *Physics Reports*, 355:235, 2001.
- [59] S. Schmidt and J. Koch. Circuit qed lattices. *Ann. Phys.*, 6:395–412, 2013.
- [60] A. N. Boto, P. Kok, D. S. Abrams, S. L. Braunstein, C. P. Williams, and J. P. Dowling. Quantum interferometric optical lithography: Exploiting entanglement to beat the diffraction limit. *Phys. Rev. Lett.*, 85:2733–2736, 2000.
- [61] A. Spörl, T. Schulte-Herbrüggen, S. J. Glaser, V. Bergholm, M. J. Storcz, J. Ferber, and F. K. Wilhelm. Optimal control of coupled josephson qubits. *Phys. Rev. A*, 75:012302, 2007.
- [62] S.J. Glaser, T. Schulte-Herbrüggen, M. Sieveking, O. Schedletzky, N.C. Nielsen, O.W. Sorensen, and C. Griesinger. Unitary control in quantum ensembles: Maximizing signal intensity in coherent spectroscopy. *Science*, 280:421, 1998.
- [63] T.W. Boreneman, M.D. Hurliman, and D.G. Cory. Application of optimal control to cpmg refocusing pulse design. *J. Magn. Res.*, 207:220, 2010.
- [64] M. Lapert, G. Ferrini, and D. Sugny. Optimal control of quantum superpositions in a bosonic josephson junction. *Phys. Rev. A*, 85:023611, 2012.
- [65] M. Choi. Completely positive linear maps on complex matrices. *Linear Algebra and its applications*, 10:285–290, 1975.
- [66] E. Størmer. Choi matrices and dual functionals. *Springer Monographs in Mathematics*, pages 49–62, 2013.

- [67] P. Rebentrost and F. K. Wilhelm. Optimal control of a leaking qubit. *Phys. Rev. B*, 79:060507, 2009.
- [68] J. L. O'Brien, G. J. Pryde, A. Gilchrist, D. F.V. James, N. K. Langford, T. C. Ralph, and A. G. White. Quantum process tomography of a controlled-not gate. *Phys. Rev. Lett.*, 93:080502, 2004.
- [69] T. Yamamoto, M. Neeley, E. Lucero, R. C. Bialczak, J. Kelly, M. Lenander, Matteo Mariantoni, A. D. O'Connell, D. Sank, H. Wang, M. Weides, J. Wenner, Y. Yin, A. N. Cleland, , and John M. Martinis. Quantum process tomography of two-qubit controlled-z and controlled-not gates using superconducting phase qubits. *Phys. Rev. B*, 82:184515, 2010.
- [70] C. Dankert, R. Cleve, J. Emerson, and E. Livine. Exact and approximate unitary 2-designs and their application to fidelity estimation. *Phys. Rev. A*, 80:012304, 2009.
- [71] C. Jarlskog. A recursive parametrization of unitary matrices. *J. Math. Phys.*, 46:103508, 2005.
- [72] C. Jarlskog. Recursive parametrization and invariant phases of unitary matrices. *J. Math. Phys.*, 47:013507, 2006.
- [73] M. M. Müller, D. M. Reich, M. Murphy, H. Yuan, J. Vala, K. B. Whaley, T. Calarco, and C. P. Koch. Optimizing entangling quantum gates for physical systems. *Phys. Rev. A*, 84:042315, 2011.
- [74] S. G. Schirmer and P. de Fouquieres. Efficient algorithms for optimal control of quantum dynamics: the krotov method unencumbered. *New J. Phys.*, 13:073029, 2011.
- [75] R. Barends, J. Kelly, A. Megrant, A. Veitia, D. Sank, E. Jeffrey, T. C. White, J. Mutus, A. G. Fowler, B. Campbell, Y. Chen, Z. Chen, B. Chiaro, A. Dunsworth, C. Neill, P. O'Malley, P. Roushan, A. Vainsencher, J. Wenner, A. N. Korotkov, A. N. Cleland, and J. M. Martinis. Logic gates at the surface code threshold: Superconducting qubits poised for fault-tolerant quantum computing. *Nature*, 508:500–503, 2014.
- [76] J. M. Chow, J. M. Gambetta, L. Tornberg, Jens Koch, Lev S. Bishop, A. A. Houck, B. R. Johnson, L. Frunzio, S. M. Girvin, and R. J. Schoelkopf. Randomized benchmarking and process tomography for gate errors in a solid-state qubit. *Phys. Rev. Lett.*, 102:090502, 2009.

- [77] E. Magesan, J. M. Gambetta, and J. Emerson. Characterizing quantum gates via randomized benchmarking. *Phys. Rev. A*, 85:042311, 2012.
- [78] E. Magesan, J. M. Gambetta, and J. Emerson. Scalable and robust randomized benchmarking of quantum processes. *Phys. Rev. Lett.*, 106:180504, 2011.
- [79] E. Magesan, J. M. Gambetta, B. R. Johnson, C. A. Ryan, J. M. Chow, S. T. Merkel, M. P. da Silva, G. A. Keefe, M. B. Rothwell, T. A. Ohki, M. B. Ketchen, and M. Steffen. Efficient measurement of quantum gate error by interleaved randomized benchmarking. *Phys. Rev. Lett.*, 109:080505, 2012.
- [80] J. M. Epstein, A. W. Cross, E. Magesan, and J. M. Gambetta. Investigating the limits of randomized benchmarking protocols. arXiv:1308.2928.
- [81] J. Emerson, R. Alicki, and K. Zyczkowski. Scalable noise estimation with random unitary operators. *J. Opt. B: Quantum Semiclass. Opt.*, 7:S347–S352, 2005.
- [82] J. Nocedal and S. W. Stephen. *Numerical Optimization*. Springer, New York, 2006.
- [83] F. F. Floether, Pierre de Fouquieres, and Sophie G. Schirmer. Robust quantum gates for open systems via optimal control: Markovian versus non-markovian dynamics. *New Journal of Physics*, 14:073023, 2012.
- [84] P. de Fouquieres, S.G. Schirmer, S.J. Glaser, and I. Kuprov. Second order gradient ascent pulse engineering. *J. Magn. Reson.*, 212:412–417, 2011.
- [85] S. Machnes, U. Sander, S. J. Glaser, P. de Fouquière, A. Gruslys, S. Schirmer, and T. Schulte-Herbrüggen. Comparing, optimizing, and benchmarking quantum-control algorithms in a unifying programming framework. *Phys. Rev. A*, 84:022305, Aug 2011.
- [86] J. M. Gambetta, F. Motzoi, S. T. Merkel, , and F. K. Wilhelm. Analytic control methods for high-fidelity unitary operations in a weakly nonlinear oscillator. *Physical Review A*, 83:012308, 2011.
- [87] W.S. Warren. Effect of arbitrary laser or nmr pulse shapes on population inversion and coherence. *J. Chem. Phys.*, 81:5437, 1984.

- [88] J. M. Gambetta, A. A. Houck, and Alexandre Blais. Superconducting qubit with purcell protection and tunable coupling. *Phys. Rev. Lett.*, 106:030502, Jan 2011.
- [89] M. Steffen, J. M. Martinis, and I. L. Chuang. Accurate control of josephson phase qubits. *Phys. Rev. B*, 68:224518, 2003.
- [90] B. Khani, J. M. Gambetta, F. Motzoi, and F. K. Wilhelm. Optimal generation of fock states in a weakly nonlinear oscillator. *Phys. Scr.*, T137:014021, 2009.
- [91] L. DiCarlo. Private communication.
- [92] F. Motzoi and F. K. Wilhelm. Improving frequency selection of driven pulses using derivative-based transition suppression. *Phys. Rev. A*, 88:062318, 2013.
- [93] A. Gangopadhyay, M. Dzero, and V. Galitski. Exact solution for quantum dynamics of a periodically-driven two-level-system. *Phys. Rev. B*, 82:024303, 2010.
- [94] R.L. Vold, J.S. Waugh, M.P. Klein, and D.E. Phelps. Measurement of spin relaxation in complex systems. *J. Chem. Phys.*, 48:3831, 1968.
- [95] D.I. Hoult. The solution of the bloch equations in the presence of a varying b1 field — an approach to selective pulse analysis. *J. Magn. Res.*, 35:69, 1979.
- [96] R. Freeman. *Spin Choreography: Basic Steps in High Resolution NMR*. Oxford University Press, New York, 1998.
- [97] J. M. Chow, L. DiCarlo, J. M. Gambetta, F. Motzoi, L. Frunzio, S. M. Girvin, and R. J. Schoelkopf. Implementing optimal control pulse shaping for improved single-qubit gates. *Phys. Rev. A*, 82:040305(R), 2010.
- [98] E. Lucero, K. Julian, R. C. Bialczak, M. Lenander, M. Mariani, M. Neeley, A. D. O’Connell, D. Sank, H. Wang, M. Weides, J. Wenner, T. Yamamoto, A. N. Cleland, and J. M. Martinis. Reduced phase error through optimized control of a superconducting qubit. *Phys. Rev. A*, 82:042339, Oct 2010.
- [99] J. Hendrix. *Electric Ladyland*. Reprise Records, New York, 1968.

- [100] R. Stock and D.F.V. James. Scalable, high-speed measurement-based quantum computer using trapped ions. *Phys. Rev. Lett.*, 102:170501, 2009.
- [101] M.A. Sillanpää, J.I. Park, and R.W. Simmonds. Coherent quantum state storage and transfer between two phase qubits via a resonant cavity. *Nature*, 449:438, 2007.
- [102] J. Majer, J.M. Chow, J.M. Gambetta, J. Koch, B.R. Johnson, J.A. Schreier, L. Frunzio, D.I. Schuster, A.A. Houck, A. Wallraff, A. Blais, M.H. Devoret, S.M. Girvin, and R.J. Schoelkopf. Coupling superconducting qubits via a cavity bus. *Nature*, 449:443, 2007.
- [103] A. Blais, J. Gambetta, A. Wallraff, D.I. Schuster, S.M. Girvin, M.H. Devoret, and R.J. Schoelkopf. Quantum-information processing with circuit quantum electrodynamics. *Phys. Rev. A*, 75:032329, 2007.
- [104] J. H. Plantenberg, P. C. de Groot, C. J. P. M. Harmans, and J. E. Mooij. Demonstration of controlled-not quantum gates on a pair of superconducting quantum bits. *Nature*, 447(7146):836–839, 2007.
- [105] Y.-X. Liu, L.F. Wei, J.S. Tsai, and F. Nori. Controllable coupling between flux qubits. *Phys. Rev. Lett.*, 96:067003, 2006.
- [106] J. M. Chow, A. D. Corcoles, J. M. Gambetta, C. Rigetti, B. R. Johnson, J. A. Smolin, J. R. Rozen, G. A. Keefe, M. B. Rothwell, M. B. Ketchen, and M. Steffen. Simple all-microwave entangling gate for fixed-frequency superconducting qubits. *Phys. Rev. Lett.*, 107:080502, 2011.
- [107] A. Dewes, R. Lauro, F.R. Ong, V. Schmitt, P. Milman, P. Bertet, D. Vion, and D. Esteve. Quantum speeding-up of computation demonstrated in a superconducting two-qubit processor. *Phys. Rev. B*, 85:140503(R), 2012.
- [108] L. DiCarlo, J. M. Chow, J. M. Gambetta, Lev S. Bishop, B. R. Johnson, D. I. Schuster, J. Majer, A. Blais, L. Frunzio, S. M. Girvin, and R. J. Schoelkopf. Demonstration of two-qubit algorithms with a superconducting quantum processor. *Nature*, 460:240, 2009.
- [109] A. Fedorov, L. Steffen, M. Baur, M.P. da Silva, and A. Wallraff. Implementation of a toffoli gate with superconducting circuits. *Nature*, 481:170, 2012.

- [110] J. Ghosh, A. Galiutdinov, Z. Zhou, A. N. Korotkov, J. M. Martinis, and M. R. Geller. High-fidelity controlled- $\sigma$  z gate for resonator-based superconducting quantum computers. *Phys. Rev. A*, 87:022309, 2013.
- [111] J.M. Raimond, M. Brune, and S. Haroche. Manipulating quantum entanglement with atoms and photons in a cavity. *Rev. Mod. Phys.*, 73:565, 2001.
- [112] T. Frey, P.J. Leek, M. Beck, A. Blais, T. Ihn, K. Ensslin, and A. Wallraff. Dipole coupling of a double quantum dot to a microwave resonator. *Phys. Rev. Lett.*, 108:046807, 2012.
- [113] K.D. Petersson, L.W. McFaul, M.D. Schroer, M. Jung, J.M. Taylor, A.A. Houck, and J.R. Petta. Circuit quantum electrodynamics with a spin qubit. *Nature*, 490:380, 2012.
- [114] M. Mariantoni, H. Wang, T. Yamamoto, M. Neeley, R. C. Bialczak, Y. Chen, M. Lenander, E. Lucero, A. D. OConnell, D. Sank, M. Weides, J. Wenner, Y. Yin, J. Zhao, A. N. Korotkov, A. N. Cleland, and J. M. Martinis. Implementing the quantum von neumann architecture with superconducting circuits. *Science*, 334:61–65, 2011.
- [115] S. Montangero, T. Calarco, and R. Fazio. Robust optimal quantum gates for josephson charge qubits. *Phys. Rev. Lett.*, 99:170501, 2007.
- [116] A. Blais, R.-S. Huang, A. Wallraff, S. M. Girvin, and R. J. Schoelkopf. Cavity quantum electrodynamics for superconducting electrical circuits: An architecture for quantum computation. *Phys. Rev. A*, 69:062320, 2004.
- [117] F. W. Strauch. Quantum logic gates for coupled superconducting phase qubits. *Phys. Rev. Lett.*, 91:167005, 2003.
- [118] S. Gustavsson, O. Zwiernik, J. Bylander, F. Yan, F. Yoshihara, Y. Nakamura, T. P. Orlando, and W. D. Oliver. Improving quantum gate fidelities by using a qubit to measure microwave pulse distortions. *Phys. Rev. Lett.*, 110:040502, 2013.
- [119] F. Motzoi, J. M. Gambetta, S. T. Merkel, and F. K. Wilhelm. Optimal control methods for rapidly time-varying hamiltonians. *Phys. Rev. A*, 84:022307, 2011.
- [120] D. T. Colbert and W. H. Miller. A novel discrete variable representation for quantum mechanical reactive scattering via the smatrix kohn method. *Journal of Chemical Physics*, 96:1982–1991, 1991.

- [121] L. S. Schulman. Jump time and passage time: The duration of a quantum transition. *Lec. Notes Phys.*, 734:107–128, 2008.
- [122] L. Vaidman. Minimum time for the evolution to an orthogonal quantum state. *Am. J. Phys.*, 60:182, 1992.
- [123] A. Galiatdinov, A. N. Korotkov, and J. M. Martinis. Resonator zero qubit architecture for superconducting qubits. *Phys. Rev. A*, 85:042321, 2012.
- [124] B. Khani, S. T. Merkel, F. Motzoi, J. M. Gambetta, and F. K. Wilhelm. High-fidelity quantum gates in the presence of dispersion. *Phys. Rev. A*, 85:022306, 2012.
- [125] E. Jeffrey, D. Sank, J.Y. Mutus, T.C. White, J. Kelly, R. Barends, Y. Chen, Z. Chen, B. Chiaro, A. Dunsworth, A. Megrant, P.J.J. O’Malley, C. Neill, P. Roushan, A. Vainsencher, J. Wenner, A. N. Cleland, and John M. Martinis. Fast scalable state measurement with superconducting qubits. *arXiv*, 1401:0257v3, 2014.
- [126] M. Neeley, M. Ansmann, R. C. Bialczak, M. Hofheinz, N. Katz, E. Lucero, A. O’Connell, H. Wang, A. N. Cleland, and J. M. Martinis. Process tomography of quantum memory in a josephson-phase qubit coupled to a two-level state. *Nat. Phys.*, 4:523–526, 2008.
- [127] Yu Chen, D. Sank, P. OMalley, T. White, R. Barends, B. Chiaro, J. Kelly, E. Lucero, M. Mariantoni, A. Megrant, C. Neill, A. Vainsencher, J. Wenner Y. Yin, A. N. Cleland, and John M. Martinis. Multiplexed dispersive readout of superconducting phase qubits. *Appl. Phys. Lett.*, 101:182601, 2012.
- [128] Y.-F. Chen, D. Hover, S. Sendelbach, L. Maurer, S. T. Merkel, E. J. Pritchett, F. K. Wilhelm, and R. McDermott. Microwave photon counter based on josephson junctions. *Phys. Rev. Lett.*, 107:217401, 2011.
- [129] A. Castro, J. Werschnik, and E.K.U. Gross. Controlling the dynamics of many-electron systems from first principles: A combination of optimal control and time-dependent density-functional theory. *Phys. Rev. Lett.*, 109:153603, 2012.
- [130] S. E. Sklarz and D. J. Tannor. Loading a bose-einstein condensate onto an optical lattice: An application of optimal control theory to the nonlinear schrödinger equation. *Phys. Rev. A*, 66:053619, 2002.

- [131] T. Schulte-Herbrüggen, A. Spörl, N. Khaneja, and S. J. Glaser. Optimal control for generating quantum gates in open dissipative systems. *J. Phys. B: At. Mol. Opt. Phys.*, 44:154013, 2011.
- [132] M. Raginsky. A fidelity measure for quantum channels. *Physics Letters A*, 290:11–18, 2001.
- [133] R. C. Ward. Numerical computation of the matrix exponential with accuracy estimate. *J. Numer. Anal.*, 14:600–610, 1977.
- [134] C. Moler and C. Van Loan. Nineteen dubious ways to compute the exponential of a matrix, twenty-five years later. *Society for Industrial and Applied Mathematics*, 45(1):3, 2003.
- [135] L. C. G. Govia, E. J. Pritchett, S. T. Merkel, D. Pineau, and F. K. Wilhelm. Theory of josephson photomultipliers: Optimal working conditions and back action. *Phys. Rev. A*, 86:032311, 2012.
- [136] K. B. Cooper, Matthias Steffen, R. McDermott, R.W. Simmonds, Seongshik Oh, D. A. Hite, D. P. Pappas, and John M. Martinis. Observation of quantum oscillations between a josephson phase qubit and a microscopic resonator using fast readout. *Phys. Rev. Lett.*, 93:180401, 2004.
- [137] R.W. Simmonds, K.M. Lang, D. A. Hite, S. Nam, D. P. Pappas, and J. M. Martinis. Decoherence in josephson phase qubits from junction resonators. *Phys. Rev. Lett.*, 93:077003, 2004.
- [138] U. Weiss. *Quantum Dissipative Systems*. World Scientific, 1999.
- [139] R. Schmidt, A. Negretti, J. Ankerhold, T. Calarco, and J. T. Stockburger. Optimal control of open quantum systems: Cooperative effects of driving and dissipation. *Phys. Rev. Lett.*, 107:130404, 2011.
- [140] P. Doria, T. Calarco, and S. Montangero. Optimal control technique for many-body quantum dynamics. *Phys. Rev. Lett.*, 106:190501, 2011.
- [141] R. Bücker, J. Grond, S. Manz, T. Berrada, T. Betz, C. Koller, U. Hohenester, T. Schumm, A. Perrin, and J. Schmiedmayer. Twin-atom beams. *Nat. Phys.*, 7:608, 2011.
- [142] G. Jäger and U. Hohenester. Optimal quantum control of bose-einstein condensates in magnetic microtraps: Consideration of filter effects. *Phys. Rev. A*, 88:035601, 2013.

- [143] R. Nigmatullin and S. G. Schirmer. Implementation of fault-tolerant quantum logic gates via optimal control. *New Journal of Physics*, 11:105032, 2009.
- [144] D. Egger and F. K. Wilhelm. Optimized controlled-z gates for two superconducting qubits coupled through a resonator. *Superconductor Science and Technology*, 27:014001, 2014.
- [145] M. Hellgren, E. Räsänen, and E. K. U. Gross. Optimal control of strong-field ionization with time-dependent density-functional theory. *Phys. Rev. A*, 88:013414, 2013.
- [146] R. S. Judson and H. Rabitz. Teaching lasers to control molecules. *Phys. Rev. Lett.*, 68:1500, 1992.
- [147] P. Owrutsky and N. Khaneja. Control of inhomogeneous ensembles on the bloch sphere. *Phys. Rev. A*, 86:022315, 2012.
- [148] T. E. Skinner, T. O. Reiss, B. Luy, N. Khaneja, and S. J. Glaser. Application of optimal control theory to the design of broadband excitation pulses for high-resolution nmr. *J. Magn. Res.*, 163:8–15, 2003.
- [149] J. A. Nelder and R. Mead. A simplex method for function minimization. *Comput. J.*, 7:308–313, 1965.
- [150] J. Kelly, R. Barends, B. Campbell, Y. Chen, Z. Chen, B. Chiaro, A. Dunsworth, A. G. Fowler, I.-C. Hoi, E. Jeffrey, A. Megrant, J. Mutus, C. Neill, P. J. J. O’Malley, C. Quintana, P. Roushan, D. Sank, A. Vainsencher, J. Wenner, T. C. White, A. N. Cleland, and J. M. Martinis. Optimal quantum control using randomized benchmarking. arXiv:1403.0035.
- [151] E. Lucero, R. Barends, Y. Chen, J. Kelly, M. Mariantoni, A. Megrant, P. OMalley, D. Sank, A. Vainsencher, J. Wenner, Y. Yin T. White, A. N. Cleland, and J. M. Martinis. Computing prime factors with a josephson phase qubit quantum processor. *Nature Physics*, 8:719, 2012.
- [152] M. J. Biercuk, H. Uys, A. P. VanDevender, N. Shiga, W. M. Itano, and J. J. Bollinger. Optimized dynamical decoupling in a model quantum memory. *Nature*, 458:996–1000, 2009.
- [153] S. Haroche and J.-M. Raimond. *Exploring the Quantum: Atoms, Cavities, and Photons*. Oxford University Press, Oxford, 2006.

- [154] J.Q. You and F. Nori. Atomic physics and quantum optics using superconducting circuits. *Nature*, 474:589, 2011.
- [155] J. Bourassa, J. M. Gambetta, A. A. Abdumalikov Jr., O. Astafiev, Y. Nakamura, and A. Blais. Ultrastrong coupling regime of cavity qed with phase-biased flux qubits. *Phys. Rev. A*, 80:032109, 2009.
- [156] P. Forn-Diaz, J. Lisenfeld, D. Marcos, J. J. Garcia-Ripoll, E. Solano, C. J. P. M. Harmans, and J. E. Mooij. Observation of the bloch-siegert shift in a qubit-oscillator system in the ultrastrong coupling regime. *Phys. Rev. Lett.*, 105:237001, 2010.
- [157] T. Niemczyk, F. Deppe, H. Huebl, E. P. Menzel, F. Hocke, M. J. Schwarz, J. J. Garcia-Ripoll, D. Zueco, T. Hmmer, E. Solano, A. Marx, and R. Gross. Circuit quantum electrodynamics in the ultrastrong-coupling regime. *Nature Physics*, 6:772, 2010.
- [158] S. Filipp, M. Göppl, J. M. Fink, M. Baur, R. Bianchetti, L. Steffen, and A. Wallraff. Multimode mediated qubit-qubit coupling and dark-state symmetries in circuit quantum electrodynamics. *Phys. Rev. A*, 83(063827):063827, 2011.
- [159] M. Mariani, F. Deppe, A. Marx, R. Gross, F. K. Wilhelm, and E. Solano. Two-resonator circuit quantum electrodynamics: A superconducting quantum switch. *Phys. Rev. B*, 78:104508, 2008.
- [160] S. T. Merkel and F. K. Wilhelm. Generation and detection of noon states in superconducting circuits. *New J. Phys.*, 12:093036, 2010.
- [161] H. Wang, M. Mariani, R. C. Bialczak, M. Lenander, E. Lucero, M. Neeley, A. D. O’Connell, D. Sank, M. Weides, J. Wenner, T. Yamamoto, Y. Yin, J. Zhao, J. M. Martinis, and A. N. Cleland. Deterministic entanglement of photons in two superconducting microwave resonators. *Phys. Rev. Lett.*, 106:060401, 2011.
- [162] M. Mariani, H. Wang, R. C. Bialczak, M. Lenander, E. Lucero, M. Neeley, A. D. O’Connell, D. Sank, M. Weides, J. Wenner, T. Yamamoto, Y. Yin, J. Zhao, J. M. Martinis, and A. N. Cleland. Photon shell game in three-resonator circuit quantum electrodynamics. *Nature Physics*, 7:287–293, 2011.
- [163] A. Nunnenkamp, J. Koch, and S. M. Girvin. Synthetic gauge fields and homodyne transmission in jaynes-cummings lattices. *New J. Phys.*, 13:095008, 2011.

- [164] M. J. Hartmann, F. G. S. L. Brandao, and M. B. Plenio. Strongly interacting polaritons in coupled arrays of cavities. *Nat. Phys.*, 2:849–855, 2006.
- [165] D. L. Underwood, W. E. Shanks, J. Koch, and A. A. Houck. Low-disorder microwave cavity lattices for quantum simulation with photons. *Phys. Rev. A*, 86:023837, 2012.
- [166] V. Veselago. The electrodynamics with simultaneously negative values of  $\epsilon$  and  $\mu$ . *J. Sov. Phys.*, 10:509–514, 1968.
- [167] J. B. Pendry. Negative refraction makes a perfect lens. *Phys. Rev. Lett.*, 85:3966, 2000.
- [168] G.V. Eleftheriades, A.K. Izer, and P.C. Kremer. Negative refractive index media using periodically l-c loaded transmission lines. *IEEE Trans. Microwave Theory and Techniques*, 50:2702, 2002.
- [169] H. Salehi, A. H. Majedi, and R. R. Mansour. Analysis and design of superconducting left-handed transmission lines. *IEEE Transactions on applied superconductivity*, 15:996, 2005.
- [170] A. J. Leggett, S. Chakravarty, A. T. Dorsey, Matthew P. A. Fisher, A. Garg, and W. Zwerger. Dynamics of the dissipative two-state system. *Rev. Mod. Phys.*, 59:1, 1987.
- [171] P. Jung, S. Butz, S. V. Shitov, and A. V. Ustinov. Low-loss tunable metamaterials using superconducting circuits with josephson junctions. *Appl. Phys. Lett.*, 102:062601, 2013.
- [172] D. M. Pozar. *Microwave Engineering*. Wiley, 2005.
- [173] M. H. Devoret. Quantum fluctuations in electrical circuits. In *Les Houches Session LXIII, Quantum Fluctuations p. 351-386*, 1995.
- [174] N.W. Ashcroft and N.D. Mermin. *Solid state physics*. Holt-Saunders, 1976.
- [175] O. Gühne and Géza Tóth. Entanglement detection. *Physics Reports*, 474:1–75, 2009.
- [176] F. G. Paauw, A. Fedorov, C. J. P. M. Harmans, and J. E. Mooij. Tuning the gap of a superconducting flux qubit. *Phys. Rev. Lett.*, 102:090501, 2009.

- [177] J. L. Cardy. One-dimensional models with  $1/r^2$  interactions. *J. Phys. A: Math. Gen.*, 14:1407, 1981.
- [178] R. P. Feynman and F. L. Vernon. The theory of a general quantum system interacting with a linear dissipative system. *Ann. Phys.*, 24:118–173, 1963.